University of Sussex

Cosmological Dynamics and Structure Formation

Mateja Gosenca

Submitted for the degree of Doctor of Philosophy

University of Sussex

September 2017

Declaration

I hereby declare that this thesis has not been and will not be submitted in whole or in part to another University for the award of any other degree.

The work in this thesis has been completed in collaboration with Peter Coles, Christian Byrnes, Shaun Hotchkiss, Julian Adamek, and David Seery and is comprised of the following papers:

- Mateja Gosenca, Peter Coles: "Dynamical Analysis of Scalar Field Cosmologies with Spatial Curvature", published in The Open Journal of Astrophysics. DOI: 10.21105/astro.1502.04020. arXiv:1502.04020.
- Julian Adamek, Mateja Gosenca, Shaun Hotchkiss: "Spherically Symmetric N-body Simulations with General Relativistic Dynamics", published in Phys. Rev. D 93, 023526. DOI: 10.1103/PhysRevD.93.023526. arXiv:1509.01163.
- Mateja Gosenca, Christian Byrnes, Shaun Hotchkiss, Julian Adamek: "3D simulations with boosted primordial power spectra and ultracompact minihalos", published in Phys. Rev. D 96, 123519. DOI: 10.1103/PhysRevD.96.123519. arXiv:1710.02055.

I made an essential contribution to all the papers that constitute this thesis.

Signature:

Mateja Gosenca

UNIVERSITY OF SUSSEX

Mateja Gosenca, Doctor of Philosophy

Abstract

Observational surveys which probe our universe deeper and deeper into the nonlinear regime of structure formation are becoming increasing accurate. This makes numerical simulations an essential tool for theory to be able to predict phenomena at comparable scales.

In the first part of this thesis we study the behaviour of cosmological models involving a scalar field. We are particularly interested in the existence of fixed points of the dynamical system and the behaviour of the system in their vicinity. Upon addition of spatial curvature to the single-scalar field model with an exponential potential, canonical kinetic term, and a matter fluid, we demonstrate the existence of two extra fixed points that are not present in the case without curvature. We also analyse the evolution of the equation-of-state parameter.

In the second part, we numerically simulate collisionless particles in the weak field approximation to General Relativity, with large gradients of the fields and relativistic velocities allowed. To reduce the complexity of the problem and enable high resolution simulations, we consider the spherically symmetric case. Comparing numerical solutions to the exact Schwarzschild and Lemaître-Tolman-Bondi solutions, we show that the scheme we use is more accurate than a Newtonian scheme, correctly reproducing the leading-order post-Newtonian behaviour. Furthermore, by introducing angular momentum, configurations corresponding to bound objects are found.

In the final part, we simulate the conditions under which one would expect to form ultracompact minihalos, dark matter halos with a steep power-law profile. We show that an isolated object exhibits the profile predicted analytically. Embedding this halo in a perturbed environment we show that its profile becomes progressively more similar to the Navarro-Frenk-White profile with increasing amplitude of perturbations. Next, we boost the power spectrum at a very early redshift during radiation domination on a chosen scale and simulate clustering of dark matter particles at this scale until low redshift. In this scenario halos form earlier, have higher central densities, and are more compact.

Acknowledgements

First of all, I would like to thank my supervisors, Peter Coles and David Seery. Peter always amazed me with the clearness of his insight. I will for ever cherish and remember the endless conversations we had about cosmology, physics, and life in general. David was always there to answer any question, no matter how trivial, and inspire me with his impressive understanding of cosmology.

I had the privilege of having another, unofficial supervisor: Chris Byrnes. I'd like to thank him for his eternal good mood and genuine concern about mine, as well as his readiness for discussion.

Next, I am really grateful to my collaborators Shaun Hotchkiss and Julian Adamek, who played a big role in steering my research in the direction it eventually took.

Special thanks go to my masters supervisor, Donough Regan, who was always around for a coffee, chat and invaluable advice. Antony Lewis and Robert Smith contributed to my understanding of cosmology by their comments, questions and answers in seminars, journal clubs and discussions. I am delighted I was able to do my PhD in such a lively group.

In my final year, the UCMH collaboration met in Auckland, New Zealand, where Richard Easther kindly hosted us in his group. I would also like to thank Shaun's family for opening the doors of their beach house for the collaboration and guests.

I would like to thank all my fellow students and postdocs with whom we shared so many good moments, hard moments, beach barbecues, solved conundrums, and generally had a good time. Not in any particular order: Lucía, Sam, Zé, Mark, Tic, Pippa, Scott, David, Michaela, Steven, Sean, Daniel, Hannah, Azizah, Alex, Elisa, Ridwan, Sunayana, Benoît, Antonio, Carlos, Raul, Jan, Hazel, Oliver, April, Tuğba, Chris, Djuna, Heather, Chris, Joyce, Jesus, Ewan, Julian, Julian, Ruth, Gemma, Peter, Charlotte, Geraint, Joe, Phil, Barry, Ken, Edouard, Jonny, and Mafalda. A very special acknowledgement goes to Kevin for his support over the years. Extraordinary people like him are quite hard to come across and I feel honoured I had the privilege. Furthermore, my time in Brighton would not have been nearly as amazing without the Bungayans. During the last stages of writing this thesis I had the pleasure of meeting Oliver and being given some wonderful inappropriate playlists. I will always listen to them with great joy.

Finally, I wish to thank my two brothers and their families, and especially my dad.

Ati, hvala za vso skrb, ljubezen in podporo.

Contents

List of Figures

"What is now proved was once only imagined."

William Blake

Introduction

There are two main reasons why people want to study any dynamical evolving system. The first is because they want to predict its behaviour in the future. The second is the pure intellectual satisfaction one gains from understanding something beautiful. The observable universe represents the largest system that we can potentially research, probe, describe with predictable models and therefore gain insightful understanding.

Today, this understanding rests upon decades of interplay between theoretical models predicting phenomena that were confirmed by later observations, and observations discovering new physics that led to the construction of new theories.

The success of the "hot big bang" (HBB) model, which predicts that the universe started in a hot, dense state that later expanded and cooled, relies on the impressive range of observations with which it is compatible. First came the observations that the universe is expanding. As early as 1917, Slipher (Slipher, 1917) measured that most of the galaxies are redshifted and concluded that our own must be moving with respect to them. However, the discovery of the expansion of the universe is usually accredited to Hubble (Hubble, 1929), since he introduced the linear distance-redshift relation (also the Hubble law), which states that the further things are (distance d), the faster (speed v) they are moving away from us:

$$v = Hd, \tag{1.1}$$

where H is the Hubble parameter.

In 1948, Alpher, Bethe, and Gamow (Alpher et al., 1948) calculated the abundance of elements heavier than hydrogen that were synthesised in the primordial nuclear fluid. Their prediction agrees very well with the measured values and this process is today known as the big bang nucleosynthesis.

Cosmology became a precise science, and not just something particle physicists do when they feel philosophically inspired, with the discovery of the anisotropies in the cosmic microwave background (henceforth CMB) radiation. First detected in 1964 by Penzias

and Wilson (Penzias and Wilson, 1965), the CMB is light emitted from the surface of last scattering, just after the protons and neutrons combined into atoms and the photons thus became unbound and began to stream freely. It has since been probed by three major satellite telescopes: COBE (Smoot et al., 1992) confirmed its black-body nature, and discovered temperature anisotropies of the order 10^{-5}, which were carefully mapped out by WMAP (Spergel et al., 2007) and even more precisely measured by Planck (Ade et al., 2014b) which also gave strong evidence for their Gaussian nature. In addition, numerous ground-based and balloon experiments performed measurements of polarisation, lensing, and smaller angular scales from localised regions of the sky. All these probes allow us to constrain parameters of the (standard) model of cosmology with fantastic precision.

A surprising discovery came in 1998, when two independent groups measured the accelerated expansion of the universe using type Ia supernovae (Riess et al., 1998; Perlmutter et al., 1999). This type of supernova is caused by a binary system with one of the stars being a white dwarf. Gas and dust are being accreted onto the white dwarf and when the total mass exceeds the Chandrasekhar limit (1.44 solar masses), the star explodes as a supernova with a normalisable luminosity. This fact, together with the spectroscopic measurement of their recession velocity makes them an excellent probe of the expansion in the local universe.

On the other hand, many open questions in cosmology remain to be addressed. The discovery of accelerated expansion ignited the discussion about its origin which is still very much not settled, also known as the *dark energy problem*. While the cosmological constant provides the simplest solution which requires the introduction of only one new free parameter, many attempts have been made to come up with an alternative explanation. Among the most popular candidates are tensor-scalar theories and modified gravity models, most of which rely on introducing new degrees of freedom.

Only a small fraction of the energy density in the universe today is the usual matter that we deal with on the Earth. According to Planck (Ade et al., 2015), this proportion is only 4.8%. Dark energy is the dominant component of the total energy density, with 68.3%. The rest is a component which interacts with the ordinary baryonic matter gravitationally, and possibly through the weak interaction, but not electromagnetically. It has therefore been dubbed *dark matter*.

Since all the astrophysical observations[1] rely on measuring some part of the electromagnetic spectrum, all astrophysical evidence for dark matter is indirect.

[1] with the exception of the gravitational-wave experiments (Abbott, 2017b,a) and neutrino detections, e.g. (Hirata et al., 1987)

One of the first indications of dark matter came in the 1970s, when Vera Rubin measured the rotation curves of stars in the outer regions of galaxies and concluded that the mass in those galaxies had to exceed the visible part in magnitude and spatial extent (Rubin et al., 1980). Since then, many more observations confirmed the need for such a component, from the CMB, gravitational lensing, large-scale-structure dynamics, and galaxy clusters. Despite all this evidence, to this day, dark matter manages to successfully avoid detection in a controlled environment. It is therefore not yet possible to answer questions about its precise nature, such as, is it a particle or some other effect, what is the mass of the particle, does it interact with normal matter other than through gravity, etc. For the purposes of astronomical classification, there are three main broad branches of theories of dark matter: cold, warm, and hot, which refers to the speed of the particles: cold being slow compared to the speed of light, hot being relativistic, and warm being in-between.

1.1 Standard Concepts in Cosmology

Most modern cosmological models respect the Copernican principle, which states that we are statistically typical observers of the large-scale structure in the universe. On small scales, this is a very poor assumption because it is trivial to realise that it is not the case; both in our everyday lives, and on all scales up to the galactic ones, we can observe environments with very high density, such as stars and planets, and others almost entirely vacant of any matter, such as the interstellar space. However, as we examine larger and larger scales (especially $\gtrsim$ 100 Mpc), the universe seems to become more and more Copernican.

More formally, this statement is expressed through the concepts of statistical homogeneity and isotropy. The former states that the universe is the same at every point, and the latter that it is the same in all directions. These two properties are not mutually assured; one can envision manifolds that posses only one of these qualities. But if a space is isotropic in at least two points, then it is also homogeneous. And likewise, if it is isotropic around a point and also homogeneous, then it is isotropic at every point.

The isotropy is well supported by observations of the CMB, where the relative difference in the temperature in different directions[2] does not exceed 10^{-5}.

[2] once we subtract the dipole anisotropy, caused by the movement of the Earth with respect to the CMB, which is of the order of 10^{-3}.

In practice, most cosmological models treat the contents of the universe perturbatively, by separating background from perturbations. Only the background then needs to be treated as perfectly homogenous and isotropic. Recently, there has been quite some discussion whether this is the right approach – or whether by doing so one introduces spurious effects, collectively referred to as backreaction (see for example Adamek et al. (2017a) and references within).

1.1.1 Background: The Lagrangian, Einstein equations, Friedmann equations, curvature

In classical mechanics, when we want to describe the movement of a point particle, we resort to the *principle of least action*, which states that when the system evolves from one configuration to anther, it follows a "path" in configuration space for which S is an extremum (Peskin and Schroeder, 1995). For a one-dimensional particle with coordinate $q(t)$, we can define the action as:

$$S = \int dt\, L(q, \dot{q}), \tag{1.2}$$

where $L(q, \dot{q})$ is the Lagrangian, and the dot represents time derivative. When the action is minimised, $\delta S = 0$, we obtain the equations of motion which govern the movement of the particle. In classical mechanics, the Lagrangian is defined as $L = T - V$, with T and V being the kinetic and potential energy, respectively. The Euler-Lagrange equations are:

$$\frac{\partial L}{\partial q} - \frac{d}{dt}\left(\frac{\partial L}{\partial \dot{q}}\right) = 0. \tag{1.3}$$

In classical field theory on the other hand, the Lagrangian depends on one or more fields $\varphi(x)$ and their derivatives $\partial_\mu \varphi(x)$. The action is therefore:

$$S = \int dt\, L = \int d^4x\, \mathcal{L}(\varphi(x), \partial_\mu \varphi(x)), \tag{1.4}$$

where we have introduced the Lagrangian density $\mathcal{L}$. Demanding again $\delta S = 0$, the Euler-Lagrange equation now becomes:

$$\partial_\mu \left(\frac{\partial \mathcal{L}}{\partial(\partial_\mu \varphi)}\right) - \frac{\partial \mathcal{L}}{\partial \varphi} = 0. \tag{1.5}$$

1.1.2 General Relativity (GR)

Compared to the other three fundamental interactions, gravity is treated a bit exceptionally. Instead of introducing a new field which propagates through space-time, Einstein realised that gravity can be described as curvature of the space-time itself. This insight was inspired by two principles: the equivalence principle, which states that gravitational and inertial mass are equivalent, and the relativity principle, demanding that the laws of physics should not depend on the choice of the coordinate system they are written in. In this section we will review some basic concepts of general relativity. More details can be found in, for example, Carroll (2004) and Lyth and Liddle (2009).

We start with the line element, which describes the distance between two points in space-time, and can be written in the Euclidean (flat) space-time and using the Cartesian coordinates as:

$$ds^2 = -dt^2 + dx^2 + dy^2 + dz^2. \tag{1.6}$$

The overall sign of this equation is a convention; we will use $(-,+,+,+)$ throughout this thesis. More generally, we can describe the two points as vectors in four-space $x^\mu = (t, x, y, z)$ and the line element becomes:

$$ds^2 = g_{\mu\nu} dx^\mu dx^\nu. \tag{1.7}$$

Here, we have introduced the metric tensor $g_{\mu\nu}$. We also adopted Einstein summation convention, which says that every pair of repeated space-time indices is summed over. In general, $g_{\mu\nu}$ has 16 entries, but because it is symmetric, $g_{\mu\nu} = g_{\nu\mu}$, there are only 10 independent elements. We will also use the determinant of the metric, written as g.

The metric in equation (1.6) is called the Minkowski metric, characterised by there being no matter and no curvature. It is sometimes written as $\eta_{\mu\nu}$.

The action of general relativity can be written as:

$$S = \int d^4x \sqrt{-g} \left(\frac{1}{16\pi G}(R - 2\Lambda) + \mathcal{L}_{\text{matter}} \right). \tag{1.8}$$

An action containing only a term with R is usually referred to as the Einstein-Hilbert action. In the above equation, Λ is the cosmological constant and $\mathcal{L}_{\text{matter}}$ describes the matter contents of the model.

The equations of motion which can be derived by varying equation (1.8) with respect to the metric are the Einstein equations. Before we write them down, we need to introduce

some new concepts.

The metric connection is expressed by the Christoffel symbol:

$$\Gamma^{\alpha}_{\mu\nu} = \frac{1}{2} g^{\alpha\beta}(g_{\beta\nu,\mu} + g_{\mu\beta,\nu} - g_{\mu\nu,\beta}) \tag{1.9}$$

where commas symbolise partial derivatives with respect to the coordinate, for example $g_{\mu\nu,\alpha} = \partial_\alpha g_{\mu\nu} = \frac{\partial g_{\mu\nu}}{\partial x^\alpha}$. Having the metric connection we can write down the Riemann tensor:

$$R^{\rho}{}_{\sigma\mu\nu} = \partial_\mu \Gamma^{\rho}_{\nu\sigma} - \partial_\nu \Gamma^{\rho}_{\mu\sigma} + \Gamma^{\rho}_{\mu\lambda}\Gamma^{\lambda}_{\nu\sigma} - \Gamma^{\rho}_{\nu\lambda}\Gamma^{\lambda}_{\mu\sigma} \tag{1.10}$$

The Riemann tensor measures the intrinsic curvature, a property defined on a given manifold. It should be distinguished from the extrinsic curvature, which depends on how a submanifold is embedded in some higher-dimensional manifold. We can also formulate the symmetric Ricci tensor:

$$R_{\mu\nu} = R^{\lambda}{}_{\mu\lambda\nu} \tag{1.11}$$

and Ricci scalar:

$$R = R^{\mu}{}_{\mu}. \tag{1.12}$$

With these definitions in place, one can, by varying the action with respect to the metric, derive the Einstein equations:

$$R_{\mu\nu} - \frac{1}{2} g_{\mu\nu} R + \Lambda g_{\mu\nu} = (8\pi G) T_{\mu\nu}. \tag{1.13}$$

G is the Newton's gravitational constant; sometimes the reduced Planck mass $M_{Pl}^2 = 1/(8\pi G)$ and $\kappa = 8\pi G$ are also used. The first two terms on the left side of this equation come from the first term in equation (1.8) and describe the curvature of the space-time. The third term on the left contanis Λ, the cosmological constant. On the left side we introduced the stress-energy tensor, $T_{\mu\nu}$, which depends on what matter contents of the universe are described by $\mathcal{L}_{\text{matter}}$ and is derived by:

$$T^{\mu\nu} = -\frac{2}{\sqrt{-g}} \frac{\partial(\mathcal{L}_{\text{matter}}\sqrt{-g})}{\partial g_{\mu\nu}}. \tag{1.14}$$

For the perfect fluid, which can be characterised by two quantities, its density ρ and pressure p, the energy-momentum tensor is $T^{\nu}_{\mu} = \text{diag}(-\rho, p, p, p)$. More generally, pressure

p and density ρ are related through the equation of state:

$$p = w\rho, \tag{1.15}$$

where the parameter w corresponds to different types of matter. For pure pressureless matter, radiation, or the cosmological constant, w is constant and takes the value of 0, $1/3$, and -1, respectively.

1.1.3 The background dynamics

Throughout this thesis, we will use the concept of the scale factor $a(t)$ and comoving coordinates x, related as:

$$r = a(t)x, \tag{1.16}$$

where r is the proper physical coordinate. Because we assume homogeneity and isotropy, a only depends on time. Focusing only on the dynamics of the background, and using the Friedmann-Lemaître-Robertson-Walker (FLRW) metric ansatz:

$$ds^2 = -dt^2 + a(t)^2 \left(\frac{dr^2}{1 - Kr^2} + r^2 d\theta^2 + r^2 \sin\theta^2 d\phi^2 \right), \tag{1.17}$$

the Einstein equations (1.13) can be simplified into the Friedmann equations:

$$H^2 = \frac{8\pi G}{3}\rho - \frac{K}{a^2} + \frac{\Lambda}{3} \tag{1.18a}$$

$$\frac{\ddot{a}}{a} = -\frac{4\pi G}{3}(\rho + 3p) + \frac{\Lambda}{3}. \tag{1.18b}$$

We have introduced the Hubble parameter $H \equiv \dot{a}/a$ and the curvature constant K, which can be negative, zero, or positive for open, flat, or closed universe, respectively. This will be discussed in some more detail in Chapter 2. The energy-momentum conservation ($T^{\mu\nu}{}_{;\nu} = 0$) gives the continuity equation, which holds separately for each component of the universe:

$$\dot{\rho} + 3H(\rho + p) = 0. \tag{1.19}$$

Using the equation of state (1.15), the continuity equation can be rewritten as:

$$\frac{\dot{\rho}}{\rho} = -3(1 + w)\frac{\dot{a}}{a} \tag{1.20}$$

which can be integrated, assuming that w is constant, to give the dependence of the background density on the scale factor, depending on the dominant fluid of the universe:

$$\rho(t) = a(t)^{-3(1+w)}. \tag{1.21}$$

The radiation dominated phase ($w = 1/3$) therefore decays as $\rho_{\rm rad} \propto a^{-4}$. This means that for our universe at some point the energy density of matter ($w = 0$) started to dominate with $\rho_{\rm mat} \propto a^{-3}$. We refer to this event as the radiation-matter equality. At even later times matter energy density gets diluted as well and the universe effectively became dominated by the cosmological constant ($w = -1$), which has no dependence on the scale factor: $\rho_\Lambda \propto const.$ These are of course only the cases where one component dominates over the others and to account for the transitions between different stages, one has to consider a mixture of fluids.

Another useful quantity to define is the critical density:

$$\rho_{\rm crit} = \frac{3H^2}{8\pi G}. \tag{1.22}$$

This follows from the first Friedmann equation (1.18a), with the spatial curvature set to zero and the cosmological constant absorbed in $\rho_{\rm crit}$. The critical density is therefore the density of the universe if there is no background curvature. It can also be regarded as the total energy density of the universe, once all different components (apart from curvature) are summed over. With this parameter in place, one can also define the density parameter, for each component i of the universe as $\Omega_i = \rho_i/\rho_{\rm crit}$. The first Friedmann equation can then be written as

$$H(a)^2 = H_{(0)}^2 \left(\frac{\Omega_{(0)\rm r}}{a^4} + \frac{\Omega_{(0)\rm m}}{a^3} + \frac{\Omega_{(0)K}}{a^2} + \Omega_{(0)\Lambda} \right), \tag{1.23}$$

where the subscript (0) denotes the value of the quantities at present, and we have additionally defined $H_{(0)}^2 = 8\pi G \rho_{(0)\rm crit}/3$ and $\Omega_{(0)K} = -K/H_{(0)}^2$.

Equation (1.23) can be used to give the functional dependence of scale factor with time for special cases, where the background is dominated by one of the fluids. For radiation, we have $a^2\dot{a}^2 = H_{(0)}^2 \Omega_{(0)\rm r} = \text{const.}$ and therefore

$$a(t) \propto t^{1/2}. \tag{1.24}$$

Similarly, for pure matter and with negligible curvature, we have

$$a(t) \propto t^{2/3}. \tag{1.25}$$

Finally, for the case of dominant cosmological constant, one finds

$$a(t) \propto e^{t}. \tag{1.26}$$

1.1.4 The redshift

The light coming from distant galaxies, which are moving away from us with the Hubble flow[3], is redshifted:

$$z = \frac{\lambda_{\text{obs}} - \lambda_{\text{src}}}{\lambda_{\text{src}}} \tag{1.27}$$

where λ_{src} is the wavelength of light, emitted by the source, and λ_{obs} recorded by the observer. This redshift z is one of the most important tools we have in cosmology to measure the distance to an object. At the same time, since the light only travels at finite speed, z serves as a measure for cosmological time. If the light is emitted at some time t_1 when the scale factor is $a(t_1)$ and recorded at t_2, we have:

$$1 + z = \frac{\lambda_2}{\lambda_1} = \frac{a(t_2)}{a(t_1)}. \tag{1.28}$$

The scale factor is a dimensionless quantity and there is freedom in its normalisation. For simplicity, it is often defined to be unity at the present time: $a(t_0) = 1$. To give some typical redshifts: the universe transitioned from being radiation to being matter dominated at $z \sim 3200$. The redshift of the CMB is $z \sim 1100$, the most distant observed galaxy is at $z \sim 11$, the epoch of reionisation started around $z \sim 6$, the most distant observed supernova is at $z \sim 4$. The universe started being dominated by a fluid with equation of state $w = -1$ at $z \sim 0.3$.

[3]Here it should be noted that a virialised object such as our Galaxy, is actually decoupled from the Hubble flow and is not expanding in physical size. Therefore it is shrinking in the comoving-coordinate frame.

1.2 Eulerian Perturbation theory

So far we have focused on the dynamics of the homogeneous background, but the really interesting aspect of the universe are its rich structures, from the cosmic web on the largest scales, clusters, individual galaxies and their halos, to stars and planets. These structures were most likely seeded by quantum fluctuations and inflated to macroscopic scales in a process described by the theory of inflation. Once the background became matter dominated, these seeds started growing due to gravitational attraction. Because fluctuations are initially sufficiently small in amplitude, their evolution can be studied using perturbation theory, until quite late times, when they start becoming order one. For a thorough review see for example Bernardeau et al. (2002). We start with the fluid equations:

Continuity equation:
$$\frac{\partial \rho}{\partial t} + \nabla \cdot (\rho \mathbf{v}) = 0, \tag{1.29a}$$

Euler equation:
$$\frac{\partial \mathbf{v}}{\partial t} + (\mathbf{v} \cdot \nabla)\mathbf{v} + \frac{\nabla p}{\rho} + \nabla \Phi = 0, \tag{1.29b}$$

Poisson equation:
$$\Delta \Phi = 4\pi G \rho, \tag{1.29c}$$

where $\rho = \rho(\mathbf{r}, t)$ is the density field, $\mathbf{v} = \mathbf{v}(\mathbf{r}, t)$ is the velocity field, $\Phi = \Phi(\mathbf{r}, t)$ denotes the gravitational potential, and $p = p(\mathbf{r}, t)$ is the pressure, related to the density through the equation of state: $p = p(\rho)$. In the Poisson equation we used the Laplacian, defined as the divergence of the gradient: $\Delta \Phi = \nabla \cdot \nabla \Phi$. For each quantity y we introduce small first-order perturbations by $y(\mathbf{r}, t) = \bar{y}(t) + \delta y(\mathbf{r}, t)$, where barred quantities denote the background and $\delta y / \bar{y} \ll 1$. Perturbation theory assumes this kind of split is possible. It is justified as long as we consider early enough times and large enough scales. Here we also assume the Newtonian limit, meaning that the velocities are non-relativistic and there are no GR effects. These two assumptions will be relaxed in Chapter 3[4]. Inserting these perturbations into the fluid equations, keeping in mind that the background terms satisfy the equations on their own, and keeping all perturbations up the first order, the perturbed fluid equations become:

$$\frac{d \delta \rho}{dt} + \bar{\rho} \nabla \cdot \delta \mathbf{v} + 3H \delta \rho = 0 \tag{1.30a}$$

[4]Note that there Φ refers to the metric perturbation and not the full potential.

$$\frac{d\delta\mathbf{v}}{dt} + H\delta\mathbf{v} + \frac{\nabla\delta p}{\bar{\rho}} + \nabla\delta\Phi = 0 \tag{1.30b}$$

$$\Delta\delta\Phi = 4\pi G\delta\rho, \tag{1.30c}$$

where we used $\bar{\mathbf{v}} = H\mathbf{r}$, and we also introduced the total derivative as $d/dt = \partial/\partial t + (\mathbf{v}\cdot\nabla)$. Equations (1.30a)–(1.30c) apply only on subhorizon scales. For the velocity field, which is a vector field, it is enough to specify its divergence $\theta(\mathbf{r}, t) = \nabla \cdot \delta\mathbf{v}(\mathbf{r}, t)$ and vorticity $\mathbf{w}(\mathbf{r}, t) = \nabla \times \delta\mathbf{v}(\mathbf{r}, t)$. Taking the divergence of the Euler equation (1.30b), and replacing the last term from the Poisson (1.30c), we get, for the evolution of the divergence:

$$\frac{d\theta}{dt} + H\theta + \frac{\Delta\delta p}{\bar{\rho}} + 4\pi G\delta\rho = 0. \tag{1.31}$$

Similarly, by taking the curl of equation (1.30b), we get, for the evolution of vorticity:

$$\frac{d\mathbf{w}}{dt} + H\mathbf{w} = 0. \tag{1.32}$$

Integrating the above equation we get $\mathbf{w}(\mathbf{r}, t) \propto a^{-1}$. This means that in the linear regime the vorticity decays with the expansion of the universe.

We now introduce the comoving coordinates $\mathbf{x}$ as $\mathbf{r} = a\mathbf{x}$. Spatial derivatives become $\nabla_{\mathbf{r}} = (1/a)\nabla_{\mathbf{x}}$ and temporal derivatives $(\partial/\partial t)_{\mathbf{r}} = (\partial/\partial t)_{\mathbf{x}} - (\bar{\mathbf{v}} \cdot \nabla)_{\mathbf{r}}$. We can further define the density contrast as:

$$\delta(\mathbf{x}, t) = \frac{\rho(\mathbf{x}, t) - \bar{\rho}(t)}{\bar{\rho}(t)}, \tag{1.33}$$

which simplifies the form of equation (1.30a) to:

$$\frac{\partial\delta}{\partial t} + \frac{1}{a}\nabla \cdot \delta\mathbf{v} = 0. \tag{1.34}$$

Taking another temporal derivative of this equation and combining it with (1.30b), we get an expression for the evolution of the density perturbation:

$$\frac{\partial^2\delta}{\partial t^2} + 2H\frac{\partial\delta}{\partial t} - \frac{c_s^2}{a^2}\Delta\delta - 4\pi G\bar{\rho}\delta = 0. \tag{1.35}$$

Here, we used $\delta p = c_s^2\delta\rho$. We can solve this equation for a matter-dominated universe with $a \propto t^{2/3}$ (equation (1.25)), and neglecting pressure perturbations $\delta p = 0$. Using the

Friedmann equation to simplify the last term: $4\pi G\bar{\rho} = -3\ddot{a}/a$, we get:

$$\frac{\partial^2\delta}{\partial t^2} + \frac{4}{3t}\frac{\partial\delta}{\partial t} - \frac{2}{3t^2}\delta = 0. \tag{1.36}$$

This is easy to solve by introducing a power-law ansatz: $\delta \propto t^\alpha$, and there are two solutions: $\alpha = \{-1, 2/3\}$. The density perturbation can therefore be expressed as the sum of two modes:

$$\delta(\mathbf{x}, t) = D^{(+)}(t)A(\mathbf{x}, 0) + D^{(-)}(t)B(\mathbf{x}, 0). \tag{1.37}$$

Here, $A(\mathbf{x}, 0)$ and $B(\mathbf{x}, 0)$ are two functions describing the initial conditions of the density perturbation field. $D^{(+)} \propto a \propto t^{2/3}$ is the growing mode which is responsible for the fact that perturbations happily grow during matter domination. $D^{(-)} \propto a^{-3/2} \propto t^{-1}$ is the beautiful sad decaying mode that everyone always neglects.

For the case of radiation domination, it can equivalently be shown that perturbations grow only logarithmically.

1.3 Lagrangian perturbation theory

Eulerian perturbation theory deals with density and velocity as fields, which take a particular value in each point of space and time. There exists another approach, the Lagrangian perturbation theory (LPT) (e.g. Buchert, 1995), where the perturbation theory is expressed not in terms of an expansion of the density field, but in terms of an expansion of the displacements of fluid elements. In this picture, already at linear order in the displacements, the density is a non-linear field. The two lowest orders of LPT are the Zel'dovich approximation (ZA) (Zel'dovich, 1970) and its second-order upgrade, 2LPT. Both of these approximations are in practice used for generating initial conditions of N-body simulations (Scoccimarro, 1998).

1.4 N-body Methods: A Review

In cosmology, N-body simulations are used to model structures which compose the cosmic web. Since the gravitational dynamics at the scales in question in non-linear, N-body simulations present an indispensable tool for building bridges between theory and observations. One of the main challenges is to ensure high dynamical range: to resolve structures that form on small as well as large scales with a sufficient accuracy.

One of the first ever N-body simulations was performed on an analog computer (Holmberg, 1941), where they used lightbulbs, photocells, and galvanometers to model and measure gravitational force. In the 1960s, the first N-body simulations were made on digital computers, using an order of 100 particles (Aarseth, 1963). What is now considered the first *cosmological* simulation was done by Press and Schechter (1974); they investigated the mass distribution of bound objects. Similar work was done by Haggerty and Janin (1974). Through the 80s and 90s, simulations grew in the number of particles used, started including richer physics such as baryons, they used progressively more sophisticated algorithms to model particles' dynamics and to extract statistical quantities such as the two-point correlation function as the measure of clustering.

1.4.1 State of the art

The success of N-body simulations has not only been driven by the sophistication of algorithms, but also by the progress in computer technology. Today the biggest simulations require multiple millions of CPU-hours and terabytes of memory and are run on the most powerful supercomputers in the world.

On cosmological scales, a noticeable breakthrough came with the Millennium run, a cosmological simulation that used over 10 billion particles (Springel et al., 2005). There have since been an few upgrades of this project, Millennium-II (Boylan-Kolchin et al., 2009) and Millennium-XXL (Angulo et al., 2012) simulations, which both use the GADGET-3 code. In terms of the size of the volume, the biggest simulation to date is DEUS FUR (Alimi et al., 2012), with box size $21000h^{-1}$Mpc and 550 billion particles.

Other noticeable simulations include Illustris (Riess et al., 1998), Bolshoi (Klypin et al., 2011), Horizon run 3 (Kim et al., 2011), MultiDark Run (Prada et al., 2012), PKDGRAV3 (Potter et al., 2016), Dark Sky Simulations (Skillman et al., 2014), MICE (Fosalba et al., 2015), The Q Continuum Simulation (Heitmann et al., 2015), and The Caterpillar Project (Griffen et al., 2016).

1.4.2 Simulation algorithms

For dark matter simulations, there are many different numerical methods used to discretise and solve the equations of motion. Direct computation of forces between all particles

(particle-particle method, henceforth PP) would scale as $\mathcal{O}(N^2)$ with N, the number of particles used, which is not the most optimal way.

One way to achieve a better performance is the particle-mesh (PM) method, which coarse-grains the continuous space of potentials into a grid, while still sampling the dark matter phase-space with particles. There has to exist the correspondence between the two: *particle-to-mesh projections* serves to construct a density field $\rho(x, t)$ from the particle distribution. There are different recipes to perform this projection; a widely-used example is the cloud-in-cell (CIC) scheme, which uses information from the eight grid points nearest to the particle. This procedure in effect treats every particle as a cube of uniform density. In Chapter 4 we will use a bit more elaborate scheme, the "triangular-shaped particle", which distributes the mass of each particle along three grid-cells in each dimension. At each time step of the simulation, potentials are calculated solving the Poisson equation, and particles are propagated along their geodesics. For this, one needs to know what the potential is at each particle's location. Therefore the fields have to be interpolated with the same particle-to-mesh scheme to avoid the effect of self-force on each particle. PM scales as $\mathcal{O}(N \log N)$. The grid can also be refined - subdivided into smaller cubic cells, if the number of particles exceeds some threshold value in a particular cell. Two examples of codes that use refined PM are ART (Kravtsov et al., 1997) and RAMSES (Teyssier, 2002).

Another algorithm that has $\mathcal{O}(N \log N)$ scaling, is the tree code (Barnes and Hut, 1986; Bouchet and Hernquist, 1988), which organises particles in a recursive tree structure. At the smallest scales, PP method is used to calculate forces between neighbouring particles. Neighbouring particles are then grouped together and treated as a single heavier one whose behaviour is determined through multipole expansion at a lower resolution. This significantly reduces the number of interactions between two particles that needs to be computed. Perhaps the most widely used code that uses a version of the tree method is Gadget 2 (Springel, 2005).

We will now briefly describe two of the N-body codes used in this work.

1.4.3 Ramses

RAMSES (Teyssier, 2002) is a Newtonian N-body code with AMR, which recursively refines the grid on a cell-by-cell basis up to some maximum level, specified by the user. This feature is essential for the hierarchical structure formation of cosmological structures,

where high resolution is required in regions with high density and solving can be optimised by requiring lower resolution in region of low density.

1.4.4 *gevolution*

gevolution (Adamek et al., 2016b) is a new-generation gravity solver that goes beyond the simplest Newtonian approximation and instead employs General Relativity. Its name derives from the fact that it finds the time-dependent solution for the first order perturbations of the metric tensor $g_{\mu\nu}$. Instead of evolving particles according to the underlying scalar potential, *gevolution* keeps track of two scalar potentials, a vector, and a tensor potential. This makes it ideal for problems with relativistic sources, as long as the weak-field approximation is valid.

1.4.5 Halo finders: ROCKSTAR

The analysis of simulations is another interesting challenge. In Chapter 4 we used the ROCKSTAR halo finder (Behroozi et al., 2013) to find the centres of the halos. For halo identification, ROCKSTAR uses a friends-of-friends algorithm in six phase-space dimensions. This algorithm assigns two particles to the same group if they are separated by less than the linking length. The process is repeated iteratively so that subgroups within the coarse groups are identified. ROCKSTAR calculates the halo's centre based on the peak of the halo's density. This means only the innermost particles are used to determine the centre which has been shown to be more accurate than averaging locations of all particles (Knebe et al., 2011).

1.4.6 N-body challenges

To extract cosmological parameters from the upcoming large-scale galaxy surveys such as Euclid (Laureijs et al., 2011) we will need to understand the behaviour of the dark matter and dark energy at the same precision. Gravitational dynamics at the scales in question in non-linear and so structure will need to be modelled with N-body simulations. But running a new simulation for each new set of cosmological parameters is very expensive and inefficient. Instead, one should focus on carefully probing the highly-dimensional space of parameters with only a few points and interpolating between them to fit the observed

power spectrum to the simulated one. One way to achieve this is with the use of cosmic emulators (Kwan et al., 2015).

Another challenge is how to correctly include the effects of baryons (Schneider and Teyssier, 2015). What is more, relativistic species such as massive neutrinos also have an impact on structure formation. Because of their relativistic nature, they can only be properly accounted for in relativistic simulations. The most self-consistent treatment of neutrinos in an N-body simulation to date was done by Adamek et al. (2017b).

1.5 Inflation and generation of primordial perturbations

In search of a theory that would describe the earliest time we can describe with a predictive model, inflation (Guth, 1981; Starobinsky, 1980; Linde, 1982) has been established as the as the most successful theory so far, with very few competing alternatives (Khoury et al., 2001; Lyth and Wands, 2002) The main concept is a phase of exponential expansion before the start of the bot big bang, which was proposed to address some issues that the HBB model faces. Apart from solving these problems, the biggest appeal of inflation is that it provides a mechanism to generate perturbations with a nearly scale-invariant power spectrum.

1.5.1 Problems with the hot big bang

The universe is observed to be flat today up to the measurable precision ($\Omega_\mathrm{K} = 0.0003 \pm 0.0005$) (Ade et al., 2015). The comoving Hubble radius $(aH)^{-1}$ grows during the matter and radiation eras, meaning that Ω_K must have been even tinier at the start of the hot big bang. This is know as *the flatness problem*. During the exponential expansion on the other hand, the amount of curvature shrinks and so inflation provides a solution to this problem.

Another problem is associated with the fact that we observe the CMB to be nearly the same in all directions. If we assume only matter and radiation eras, then patches of the sky greater than 2° could not have been in causal contact up to the decoupling and there is therefore no reason that the temperature of the CMB should be so uniform through the sky. This is known as the *horizon problem*. Inflation solves it because exponential growth of scale factor $a \propto e^{Ht}$ means that two points initially in causal contact, grow out of it, provided that the period of inflation lasts long enough.

There is another conundrum, the absence of relic particles such as magnetic monopoles, strings, domain walls, and textures. These phenomena would form during the hot big bang because of the symmetry breaking when the temperature dropped below that of the unification of electromagnetic, weak and strong interaction. Inflation solves this problem because rapid expansion dilutes these relic particles to unobservable abundance.

All of these problems can be bypassed by simply requesting some fine-tuned initial conditions for the HBB. It is however much more satisfying to have a mechanism that solves them, as well as simultaneously expanding quantum perturbations to explain the $\mathcal{O}(10^{-5})$ fluctuations in the temperature of the CMB.

1.5.2 Scalar field inflation

The theory of inflation comes in many different flavours. More precisely, there are many different models by which inflation can ensure an equation of state with $w < -1/3$. One thing they almost all have in common is the use of one or several scalar fields, sometimes referred to as "the inflaton". The action of a single scalar field ϕ is:

$$S = \int d^4x\sqrt{-g}\left(\frac{M_{\rm Pl}^2}{2}R - \partial_\mu\phi\partial^\mu\phi - V(\phi)\right) \tag{1.38}$$

The first term is the Einstein-Hilbert term, the second term is the simplest kinetic term, usually referred to as canonical, and the last term is the potential $V(\phi)$, which can in principle be any function. The equation of motion for the homogenous scalar field comes from varying the action with respect to ϕ:

$$\ddot{\phi} + 3H\dot{\phi} + \frac{dV(\phi)}{d\phi} = 0, \tag{1.39}$$

and the corresponding Friedmann equations are:

$$H^2 = \frac{1}{3M_{\rm Pl}^2}\left(\frac{1}{2}\dot{\phi}^2 + V(\phi)\right), \tag{1.40a}$$

$$\dot{H} = -\frac{\dot{\phi}^2}{2M_{\rm Pl}^2}. \tag{1.40b}$$

The energy density and pressure of a single homogeneous scalar field are:

$$\rho_\phi = \frac{1}{2}\dot{\phi}^2 + V(\phi) \tag{1.41a}$$

$$P_\phi = \frac{1}{2}\dot{\phi}^2 - V(\phi) \tag{1.41b}$$

The *slow-roll* condition is satisfied if the kinetic energy is small compared to the potential: $\frac{1}{2}\dot{\phi}^2 \ll V(\phi)$, which is usually achieved by the potential being sufficiently flat. It is useful to introduce the slow-roll parameters (Liddle and Lyth, 1992) as:

$$\epsilon(\phi) = \frac{M_{\rm Pl}^2}{2}\left(\frac{V'}{V}\right)^2 \tag{1.42a}$$

$$\eta(\phi) = M_{\rm Pl}^2 \frac{V''}{V}. \tag{1.42b}$$

In the slow-roll approximation these two parameters are small: $\epsilon(\phi) \ll 1$, $|\eta(\phi)| \ll 1$. The amount of inflation is usually parameterised by the logarithm of the ratio of the scale factor at final and initial times:

$$N = \ln \frac{a(t_{\rm f})}{a(t_{\rm i})}, \tag{1.43}$$

also known as the number of e-foldings. To solve the flatness and horizon problems, N needs to be at least 60 or 70. This amount is sufficient to ensure that the entire observable CMB sky was once within a causally connected region, and that the spatial curvature of the universe is less than the upper bound given by observations.

During inflation, quantum fluctuations expand to super-horizon scales. There, they can be described by the comoving curvature perturbation $a^2 R^{(3)}$, which is gauge invariant. Outside the horizon, this quantity remains constant even once exponential expansion ends and the radiation-dominated phase starts, regardless of the physics of reheating. $R^{(3)} = 6K/a^2$ is the Ricci scalar of the spatial part of the FLRW metric (Eq. 1.17). The Ricci scalar contains two derivatives, so we can also define $\mathcal{R}$ as $4\Delta\mathcal{R} = -a^2 R^{(3)}$, which in Fourier space becomes $\mathcal{R} = a^2 R^{(3)}/4k^2$. We can now parameterise the spatial part of the metric as

$$ds_3^2 = a(t)^2\, e^{2\zeta(\mathbf{x},t)}\, d\mathbf{x}^2, \tag{1.44}$$

where we have introduced $\zeta(\mathbf{x}, t)$ as the primordial curvature perturbation. In a gauge with no density perturbations ($\delta\rho = 0$) on super-horizon scales ζ corresponds to $\mathcal{R}$. In other slicings of the space-time, this relation can be different, for example in the conformal Newton gauge we have:

$$\mathcal{R} = \zeta + \frac{\delta\rho}{3(p+\rho)}. \tag{1.45}$$

To relate primordial curvature perturbations to the late-time density perturbation $\delta(\mathbf{k}, t)$, in linear theory, we can define a transfer function $T_\delta(k, t)$ such that $\delta(\mathbf{k}, t) = T_\delta(k, t)\mathcal{R}(\mathbf{k}, 0)$.

The power spectrum of $\delta(\mathbf{k}, t)$ describes the average amplitude of density fluctuations at each wave number k, corresponding to a scale $\lambda = 2\pi/k$:

$$\frac{2\pi^2}{k^3}\mathcal{P}_\delta(\mathbf{k})\delta_D(\mathbf{k}' - \mathbf{k}) = \langle\delta^*(\mathbf{k}', t)\delta(\mathbf{k}, t)\rangle. \tag{1.46}$$

Here, $\delta_D(\mathbf{k}' - \mathbf{k})$ is the Dirac delta and the left-hand side is only non-zero if $\mathbf{k}' = \mathbf{k}$. For a statistically isotropic field, there is no preferred direction and therefore $\mathcal{P}_\delta(k, t) = k^3|\delta(k, t)|^2/(2\pi^2)$. The power spectrum of the density at some time t can be calculated from the transfer function[5], which encodes all information about the evolution of perturbations in the linear regime:

$$\langle\delta^*(\mathbf{k}, t)\delta(\mathbf{k}', t)\rangle = T_\delta(k, t)^2 \, \frac{2\pi^2}{k^3} \, \mathcal{P}_\mathcal{R}(k) \, \delta_D(\mathbf{k}' - \mathbf{k}) \tag{1.47}$$

and therefore $\mathcal{P}_\delta(k, t) = T_\delta(k, t)^2 \, \mathcal{P}_\mathcal{R}(k)$. The primordial power spectrum generated by inflation is nearly scale-invariant and can be parameterised by:

$$\mathcal{P}_\mathcal{R}(k) = A_\mathrm{s} \left(\frac{k}{k_*}\right)^{n_\mathrm{s}-1} \tag{1.48}$$

where n_s is the spectral tilt, measured to be $n_s = 0.968 \pm 0.006$, $A_\mathrm{s} \simeq 2 \times 10^{-9}$ is the amplitude (Ade et al., 2015), and k_* is some pivot scale.

1.5.3 The matter power spectrum

From the shape of the matter power spectrum we can learn about how different scales evolved during different cosmological epochs. It is often defined as

$$P(k) = \frac{2\pi^2}{k^3}\mathcal{P}_\delta(k). \tag{1.49}$$

For large scales that entered the horizon during matter domination $k \ll 2\pi(aH)|_\mathrm{eq}$, the Poisson equation (Eq. 1.30c) implies that $\mathcal{P}_\delta \propto k^4 \, \mathcal{P}_\mathcal{R} \propto k^{n_s+3}$ and therefore $P(k) \propto k^{n_s}$. On smaller scales $k \gg 2\pi(aH)|_\mathrm{eq}$ which enter the horizon during radiation domination, the growth of density perturbations is suppressed. Super-horizon scales grow proportionally to a^2 during radiation domination, but as a scale enters the horizon, its growth is stalled (strictly speaking it grows only logarithmically) until matter-radiation equality when it starts growing $\propto a$. Its density perturbation is therefore suppressed by roughly a factor

[5] Provided that we are in the linear regime.

of $f(k) = a^2(t_H)/a_{\rm eq}^2$ where $a(t_H)$ corresponds to the scale factor when this scale enters the horizon and $a_{\rm eq}$ is the scale factor at equality. During radiation domination $a \propto t^{-1/2}$ and the suppression factor at a scale $k = 2\pi aH$ is $f(k) \propto 1/(k^2 a_{\rm eq}^2)$. The matter power spectrum is therefore suppressed by a factor of k^4, which implies $P(k) \propto k^{n_s-4}$ for scales smaller than the horizon at matter-radiation equality.

In-between these two regimes, the functional dependence of $P(k)$ turns over at the scale given by matter-radiation equality: $k_{\rm eq} = 2\pi(aH)|_{\rm eq}$. Around that scale, there are also baryon acoustic oscillations. In contrast to the cold dark matter, both baryons and photons are pressure supported, which leads to characteristic oscillations in the tightly coupled plasma. After recombination, radiation streams freely, baryons fall into the potential wells and their oscillations get imprinted onto the dark matter power spectrum.

1.6 Ultracompact Minihalos

CMB experiments managed to measure the power spectrum over ~ 3 orders of magnitudes in scale ($10^{-3}\text{Mpc}^{-1} \lesssim k \lesssim 1\text{Mpc}^{-1}$). On larger scales we are limited by the cosmic variance: there is only one universe we can observe. On the other hand, small scales ($k \gtrsim 10\text{Mpc}^{-1}$) are still very much unexplored. For the CMB probes, these scales are unobtainable because of the Silk damping. However, there could potentially be a lot of information hidden there: inflationary models that predict more power on smaller scales are not uncommon. Constraining the power spectrum on these scales therefore presents a very promising way of ruling out inflationary models. One way to place upper bounds on $k \gtrsim 10\text{Mpc}^{-1}$ is from non-detection of primordial black holes (PBHs). PBHs are postulated to form if the the density contrast in a particular region of space exceeds $\delta \gtrsim 0.3$ at horizon crossing. More power at some scale would therefore make them more abundant in the present-day universe. Although constraints from PBHs span over ~ 20 orders of magnitude, they are not very tight: about six orders of magnitude above the value of the power spectrum extrapolated from scales measured with the CMB experiments (see figure 1.1).

Much tighter constraints come from the non-detection of ultracompact minihalos (UCMHs), but over a somewhat smaller range of scales ($10\text{Mpc}^{-1} \lesssim k \lesssim 10^7\text{Mpc}^{-1}$). In contrast with the PBHs, formation of ultracompact mini haloes requires only $\delta \sim 10^{-3}$ at horizon crossing. Such overdensities would start collapsing much sooner than the most abundant, $\delta \sim 10^{-5}$ overdensities do, forming a dark matter halo soon after matter-radiation equality

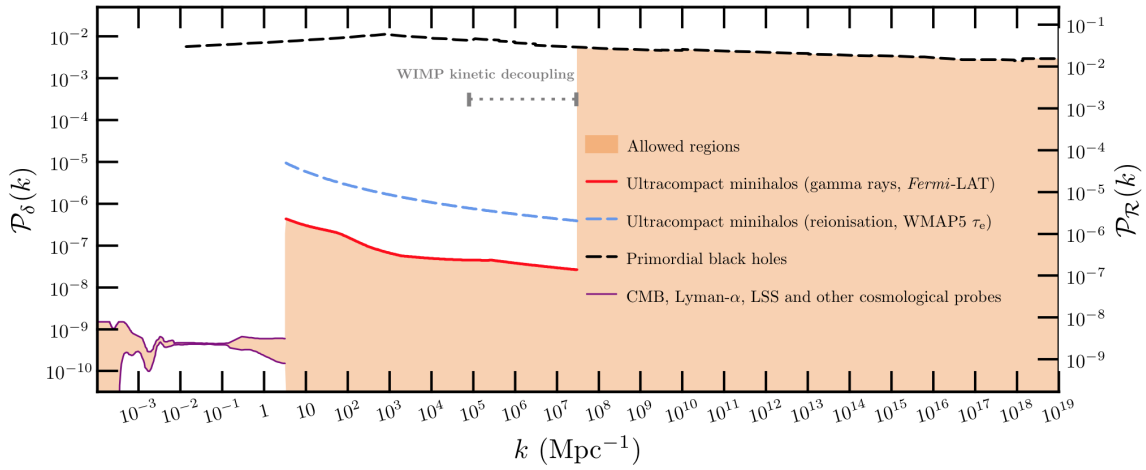

Figure 1.1: Constraints on the power spectrum from measurements of the CMB and non-detection of primordial black holes and UCMHs. The figure is taken from Bringmann et al. (2012).

when the growth of dark matter perturbations turns from logarithmic to proportional to the scale factor. Most of the literature on UCMHs assumes that they would have a very steep power-law density profile (Bertschinger, 1985):

$$\rho(r) \propto r^{-9/4} \,. \tag{1.50}$$

Their extreme compactness would allow them to retain their shape until the present time. On the other hand, the Navarro-Frenk-White (NFW) (Navarro et al., 1996, 1997) profile has been established as the best fit to the angular average of the density profile for halos found in cosmological simulations:

$$\rho_{\rm NFW}(r) = \rho_0 \frac{1}{\frac{r}{r_{\rm s}}\left(1+\frac{r}{r_{\rm s}}\right)^2}. \tag{1.51}$$

This profile is characterised by two parameters: $r_{\rm s}$, the "scale radius", and ρ_0 which serves as a normalisation parameter, and can be expressed as $\rho_0 = 4\rho(r_{\rm s})$. For radii smaller than $r_{\rm s}$ the profile has the functional dependence $\rho(r) \propto 1/r$, and for large r, it scales as $\rho(r) \propto 1/r^3$. Scale radius $r_{\rm s}$ therefore represents the scale at which the profile turns from one function to the other. The significance of this profile is in its generality; its functional dependence is the same regardless of the mass of the halo or values of cosmological parameters (Cole and Lacey, 1996; Tormen et al., 1997). It is useful to define the concentration parameter (Bullock et al., 2001) as:

$$c = \frac{r_{\rm vir}}{r_{\rm s}} \,, \tag{1.52}$$

where $r_{\rm vir}$ is the virial radius which contains the virial mass. It is often taken to be the radius within which the average density is 200 times the critical density. The value of the concentration parameter is typically between 4 and 40 for halos of different sizes and masses.

In Chapter 4 we assume that baryons and dark matter act as a single fluid. However, baryon perturbations oscillate on scales smaller than the Jeans' length, but the dark matter perturbations grow (logarithmically in radiation domination and $\propto a$ during matter domination). We therefore introduce a small error by treating all matter as collisionless and slightly overestimate the amount of perturbations. More accurate treatment of baryons would be an interesting extension of this work.

One of the main constraints on the number density of UCMHs comes from non-detection of dark matter annihilation signal (Bringmann et al., 2012). If DM is made up of weakly interacting massive particles (WMIPs) which self-annihilate and emit gamma rays, we could indirectly detect UCMHs this way. The annihilation cross-section depends on the square of the density and is therefore sensitive to the profile of the halo in its centre. Establishing what shape density profiles take in the centre of the halos is therefore crucial for understanding how to correctly translate non-detection of gamma rays to constraints on the primordial power spectrum. Since the DM dynamics is highly non-linear on these scales, this can only be explored using N-body simulations.

1.7 Open questions in cosmology

The simplest solution to the acceleration issue is to add a constant term $\Lambda g_{\mu\nu}$ in the Einstein's equation. This solution seems particularly appealing because of its simplicity. What is more, the cosmological constant gives exactly $w = -1$, but there are two concerns with this picture: fine tuning and the coincidence problem (Yoo and Watanabe, 2012a).

The former problem existed even before we knew that that the expansion is accelerated. Particle physics suggests the scale of vacuum energy Λ to be significantly bigger (Weinberg, 1989) than the dark energy today. Zero-point energy of some field with mass m, momentum k and frequency ω is given by $E = \omega/2 = \sqrt{k^2 + m^2}/2$. Integrating that over all scales up to some cut-off scale $k_{\rm max} (\gg m)$ we obtain the vacuum energy density:

$$\rho_{\rm vac} = \int_0^{k_{\rm max}} \frac{d^3k}{(2\pi)^3} \frac{\sqrt{k^2+m^2}}{2} \approx \frac{k_{\rm max}^4}{16\pi^2}. \tag{1.53}$$

If one takes the cut-off scale to be the Planck mass M_{Pl}, then the vacuum energy density

is approximately $\rho_{\text{vac}} \simeq 10^{74}\text{GeV}^4$.

On the other hand, we know that dark energy represents about 70% of the critical energy density $\rho_{\text{crit}} = 3H^2/8\pi G$ which is, for today's value of Hubble's parameter, measured to be $\rho_{\text{crit}} \simeq 10^{-47}\text{GeV}^4$ which corresponds to $\Lambda \simeq (10^{-3}eV)^4$.

Roughly speaking, there are 120 orders of magnitude between the value, predicted by quantum field theory and the one measured by cosmologists. This was dubbed "the worst theoretical prediction in history of physics". It seems very likely for the observed value to come from somewhere else rather than the vacuum energy.

The latter, perhaps less severe concern is why dark energy is of the same order of magnitude as the dark matter today. This is equivalent to asking, why do we happen to live exactly when the universe is entering the epoch of accelerated expansion. It is possible to resolve this issue with the anthropic principle.

The anthropic principle is useful to explain, for example, the distance between the Earth and the Sun. Life as we know can only exist in a certain temperature range. Hundreds of planets have been discovered around bright stars relatively close to us and we have a good reason to suspect that there are billions in our galaxy alone. Most of these planets are either too close or too far from their stars for life to develop. So the coincidence that we live on just about the right distance from Sun may actually not be a coincidence at all.

In a similar manner, we just happen to live in a moment in time that allows life forms to exist in the way we know them. Much earlier the universe was too hot and much later stars will either become black holes or disintegrate and life forms that might occur then will find that environment favourable. Although it seems, that the chance we live in such a special moment in time is vanishingly small, one must consider that life can only sprout where the conditions allow for it.

1.8 Future observational prospects

Over the next 10 to 15 years, a lot more new data will be collected and hopefully shed light on some of the conundra that we are faced with today, most importantly what drives the accelerated expansion and what the dark matter is made of.

Details of the structure formation will be probed with Euclid (Laureijs et al., 2011), a European Space Agency (ESA) mission that will take images and spectra of billions of galaxies. It is scheduled to be launched in 2020. Dark Energy Spectroscopic Instrument

(DESI) (Levi et al., 2013) will be a ground-based experiment and will measure the effect of dark energy on the expansion history of the universe. Large Synoptic Survey Telescope (LSST) (Abell et al., 2009) will survey the entire sky every few nights. Apart from detecting potentially hazardous objects in our Solar System, its significants for cosmology lies in billions of galaxies that it will record. Square Kilometre Array (SKA) (Blake et al., 2004), an array of radio telescopes, will obtain the power spectrum of dark matter by measuring the cosmic shear distortion of 10^{10} radio sources.

Dynamical Analysis of Scalar Field Cosmologies with Spatial Curvature

Mateja Gosenca and Peter Coles

2.1 Abstract

We explore the dynamical behaviour of cosmological models involving a scalar field (with an exponential potential and a canonical kinetic term) and a matter fluid with spatial curvature included in the equations of motion. Using appropriately defined parameters to describe the evolution of the scalar field energy in this situation, we elucidate the character of two fixed points that are not present in the case without curvature. We also analyse the evolution of the effective equation-of-state parameter for different initial values of the curvature.

2.2 Introduction

The discovery, based on the observed behaviour of Type Ia Supernovae (Riess et al., 1998; Perlmutter et al., 1999), that the expansion of the Universe appears to be accelerating, generated enormous theoretical interest in finding a suitable framework to account for this phenomenon. Other independent observational data such as the Cosmic Microwave Background radiation (CMB) (Hinshaw et al., 2013; Ade et al., 2014a) and Baryonic Acoustic Oscillations (BAO) (Percival et al., 2010; Abazajian et al., 2009) have subsequently confirmed that reconciling a standard Friedmann-Lemaître-Robertson-Walker model based on Einstein's General Theory of Relativity requires roughly 70% of the average energy density today to be in the form of an exotic fluid whose equation-of-state parameter $w = P/\rho$ is close to -1.

Although over fifteen years have passed since the original discovery, we still lack a compelling theoretical model to explain this so-called dark energy. The three major the-

ories that attempt to do this all rely in one way or another on modification of the Einstein Equations, which we use in the form

$$R_{\mu\nu} - Rg_{\mu\nu}/2 = 8\pi G T_{\mu\nu}, \tag{2.1}$$

in which properties of space-time appear on the left-hand side and the matter-energy contents of the Universe on the right.

The obvious phenomenological possibility is to add a constant term $\Lambda g_{\mu\nu}$ to Einstein's Equations. This seems appealing because of its simplicity and that when included in the energy-momentum tensor on the right-hand-side of the Einstein Equations, it leads to a clear prediction of the effective equation of state, namely that $w = -1$ exactly. There are, however, two major concerns with this picture. The first is that the magnitude of the vacuum energy associated with a Λ-term is out of line with the value expected from summation of zero-point energies of quantum fields up to some cut-off scale. This discrepancy is 120 orders of magnitude if one chooses a cut-off at the Planck energy, but even if some mechanism imposes a cut-off at for example a QCD energy scale, the problem is alleviated but not entirely solved (Weinberg, 1989).

The second problem is that there seems no natural explanation of why the energy density associated with the vacuum energy should be within a factor of a few of the present matter density or, in other words, why the expansion of the Universe should have began to accelerate so very recently in cosmic history. These are called the fine-tuning problem and the coincidence problem, respectively (Yoo and Watanabe, 2012b). Although such statements clearly depend on some choice of measure, related in this case to the probability distribution of the value of Λ, they must also take account of anthropic selection effects (Sivanandam, 2013).

A second class of models that might explain dark energy are those based on some form of modification of Einstein's theory of gravity. The usual approach in such models is that instead of starting from the standard Einstein-Hilbert action (which leads to the Einstein Equations), one considers additional terms in the action (Tsujikawa, 2010b). The most straightforward modification of General Relativity is to replace the Ricci scalar, R, in the Einstein-Hilbert action, by their function of this scalar, usually called $f(R)$. An example of this model is $f(R) = R + \alpha R^2$, which was in fact one of the first models of inflation, proposed by Starobinsky. The idea of using $f(R)$ for late-time acceleration was first suggested in (Capozziello, 2002) and examples of viable models of this type are proposed in (Starobinsky, 2007; Hu and Sawicki, 2007; Tsujikawa, 2008). In a more

general case, one can include an arbitrary function of R, $R_{\mu\nu}R^{\mu\nu}$ and $R_{\mu\nu\rho\sigma}R^{\mu\nu\rho\sigma}$ in the action. The Gauss-Bonnet combination $R^2-4R_{\mu\nu}R^{\mu\nu}+R_{\mu\nu\rho\sigma}R^{\mu\nu\rho\sigma}$ (Nunez and Solganik, 2005) is particularly widely explored in the literature. Another, more complicated, class of modified gravity models include scalar-tensor theories, where Ricci scalar R and a scalar field ϕ are coupled (an example of this is Brans-Dicke theory (Brans and Dicke, 1961)), and DGP (Dvali, Gabadadze and Porrati) braneworld model (Dvali et al., 2000). In the latter, particles are confined to a 3-dimensional brane, embedded in a 5(or more)-dimensional space-time with an infinite extra dimension. Standard 4D gravity is recovered at small distances, but at larger scales gravity is weakened, because its energy is essentially getting lost to the additional dimension.

A third class of possible models include modifications to the standard form of matter on the right-hand-side of the Einstein Equations, designed to generate a negative effective pressure. Among such models are quintessence, k-essence, coupled dark energy and the generalised Chaplygin gas (for reviews see Tsujikawa (2010a, 2013); Yoo and Watanabe (2012b); Copeland et al. (2006)). Quintessence, which will be studied in much greater detail in the rest of this paper, represents the idea that accelerated expansion is driven by a canonical scalar field ϕ (Wetterich, 1988; Caldwell et al., 1998; Zlatev et al., 1999). The most important consequence of this is that we now have a dynamical equation of state, rather than a constant (Copeland et al., 1998, 2006). Please note that this is also the case in some of the modified-gravity theories discussed in the paragraph above. Quintessence models are usually divided into two types on the basis of the form of potential that drives the scalar field dynamics. The first class contains models in which w gradually decreases to $w=-1$; these models are called "freezing models" (Caldwell and Linder, 2005). The forms of potential needed for this kind of behaviour were studied in (Steinhardt et al., 1999; Ratra and Peebles, 1988). In this scenario, the field energy density does not necessarily need to be negligible at the radiation epoch (this is the case with the cosmological constant). The other option is the class of "thawing models" (Caldwell and Linder, 2005) in which the field equation-of-state parameter is close to $w=-1$ initially, but at late times deviates from this value.

Theories that involve non-canonical kinetic terms in the Lagrangian are called k-essence (Chiba et al., 2000; Armendariz-Picon et al., 2001; Tamanini, 2014). The idea is that inclusion of non-canonical terms results in cosmic acceleration even without the field potential, as was shown in (Armendariz-Picon et al., 1999). A number of different scenarios were proposed, to name a few: Low energy effective string theory (Gasperini and Venezi-

ano, 1993), Ghost condensate (Arkani-Hamed et al., 2004), Tachyon field (Garousi, 2000), Dirac-Born-Infeld (DBI) theory (Silverstein and Tong, 2004; Alishahiha et al., 2004).

Furthermore, there are suggestions that dark energy and dark matter are coupled (Wetterich, 1995; Guo et al., 2007; Khoury and Weltman, 2004), that a single fluid (e.g. generalised Chaplygin gas) is responsible for dark energy and dark matter (Kamenshchik et al., 2001; Bento et al., 2003), and finally unified quintessence and inflation theories, namely quintessential inflation (Peebles and Vilenkin, 1999; Liddle and Urena-Lopez, 2006). In (Boehmer et al., 2015) the authors consider models of quintessence interacting with dark or baryonic matter.

There are also attempts to explain the apparent cosmic acceleration by means of inhomogeneities in the matter distribution in other words by breaking the assumption that cosmological space-time is described by a FLRW metric; for a review see (Buchert, 2008). One specific example is the suggestion that we live in the middle of a huge underdensity (a "void") and we interpret the expansion of its surroundings as an overall cosmic acceleration (Tomita, 2001; Alnes et al., 2006), although this seems to be in conflict with observations, see for example (Bull et al., 2012). Another approach relies upon the backreaction of cosmological perturbations (Rasanen, 2004; Kolb et al., 2005), which may be able to explain acceleration without dark energy; some work along these lines related to this paper can be found in (Buchert et al., 2006; Roy et al., 2011).

Given this plethora of possible models it is important to undertake a rigorous systematic study of their dynamical properties, in order to understand and classify the wide range of behaviours they may exhibit. In particular, focusing on the fixed points of their evolution will allow us to tackle the difficult question of what can be considered to be "natural" behaviour in a given scenario. Since the fixed points attract trajectories from a wider parameter space around them, the configuration of the system can be determined by its dynamical evolution in the fixed point rather than in the initial conditions. We concentrate on a specific class of possibilities by studying the dynamical evolution of quintessence-type models, extending previous work (described in detail below) by including spatial curvature, which is usually neglected in such analyses. Although the observational evidence at the moment points to a universe which is (nearly) spatially flat this conclusion is based on a model with restricted set of parameters. In the framework of a more general model the constraints on Ω_K can be weaker (Okouma et al., 2013). It therefore remains important to establish whether the inclusion of curvature leads to any qualitative changes in the dynamics. This issue has been addressed before (van den Hoogen et al., 1999), but

in this paper we use a different parametrisation of the equations of motion, which makes the connection between the curvature and dynamics more explicit. The aim of our analysis is to ask the question whether it is possible, via this relatively simple generalisation of the quintessence scenario, to generate an attractor solution that corresponds to a value of $w \neq -1$, which would distinguish it from many of the other models listed above.

The paper is organized as follows. In Sec. 2.3 we explore the dynamics of a single scalar field with an exponential potential and a canonical kinetic term under the flat FLRW metric. This is a well-studied system (Halliwell, 1987; Burd and Barrow, 1988) but one which repays further analysis. We find the fixed points of this system and investigate values of important dynamical parameters at these fixed points; this section follows the analysis that was done in (Copeland et al., 1998). The further details of this analysis are given in the Appendix. In Sec. 2.4.1 we generalize this approach by introducing another variable that corresponds to spatial curvature and analyze how the dynamics are affected as a consequence. We find two new fixed points and explore evolution of equation-of-state parameter for different initial values of curvature. For a parallel discussion see (Pavlov et al., 2013).

2.3 Dynamical analysis

2.3.1 Background

The action of a canonical scalar field ϕ is given by

$$S = \int d^4x\sqrt{-g}\left[\frac{1}{2}M_{\rm Pl}^2 R - \frac{1}{2}g^{\mu\nu}\partial_\mu\phi\partial_\nu\phi - V(\phi) + \mathcal{L}_{\rm M}\right], \tag{2.2}$$

where $M_{\rm Pl}$ represents the reduced Plank mass: $M_{\rm Pl} = 1/\sqrt{8\pi G} = 1/\sqrt{\kappa}$. The matter Lagrangian $\mathcal{L}_{\rm M}$ has two contributions: non-relativistic matter with equation of state $w_{\rm m} = P_m/\rho_{\rm m} = 0$ and radiation with equation of state $w_{\rm r} = 1/3$. Varying this action with respect to metric and applying the action principle gives the Einstein Equations with the energy momentum tensor:

$$T_{\mu\nu} = \partial_\mu\phi\partial_\nu\phi - g_{\mu\nu}\left(\frac{1}{2}\partial_\rho\phi\partial^\rho\phi - V(\phi)\right). \tag{2.3}$$

The assumption of spatial homogeneity and isotropy allows us to adopt the Friedmann-Lemaître-Robertson-Walker (FLRW) metric:

$$ds^2 = -dt^2 + a(t)^2 \left(\frac{dr^2}{1 - Kr^2} + r^2 d\theta^2 + r^2 \sin\theta^2 d\phi^2 \right), \tag{2.4}$$

where $a(t)$ is time-dependent scale factor and K is a constant describing the spatial curvature. The universe is open if $K < 0$, flat if $K = 0$ and closed if $K > 0$. With the use of this metric, the Einstein Equations become the modified Friedmann Equations:

$$3M_{\rm Pl}^2 H^2 = \frac{1}{2}\dot{\phi}^2 + V(\phi) + \rho_{\rm m} + \rho_{\rm r} - 3M_{\rm Pl}^2 \frac{K}{a^2} \tag{2.5a}$$

$$2M_{\rm Pl}^2 \dot{H} = -\dot{\phi}^2 - (1 + w_{\rm m})\rho_{\rm m} - (1 + w_{\rm r})\rho_{\rm r} + 2M_{\rm Pl}^2 \frac{K}{a^2} \tag{2.5b}$$

where the Hubble parameter is defined in the usual manner as $H = \dot{a}/a$. The requirement of energy-momentum conservation demands $T^{\mu\nu}{}_{;\nu} = 0$. For a homogeneous and isotropic universe the energy-momentum tensor becomes symmetric, i.e. $T_{\mu\nu} = \mathrm{diag}(-\rho, P, P, P)$ and we thus obtain the continuity equation $\dot{\rho} + 3H(\rho + P) = 0$. This equation is obeyed separately by the matter, radiation and scalar field as long as there is no coupling between these components. Applying the same condition to the energy-momentum tensor of the scalar field (2.3) we get

$$\ddot{\phi} + 3H\dot{\phi} + V_{,\phi} = 0\,, \tag{2.6}$$

where $V_{,\phi}$ is the derivative of the potential with respect to the field ϕ. Comparing this to the general continuity equation we see that the effective energy density and pressure of the scalar field are $\rho_\phi = \dot{\phi}^2/2 + V(\phi)$ and $P_\phi = \dot{\phi}^2/2 - V(\phi)$, respectively. The equation of state for the scalar field is then given by

$$w_\phi = \frac{P_\phi}{\rho_\phi} = \frac{\dot{\phi}^2/2 - V(\phi)}{\dot{\phi}^2/2 + V(\phi)}. \tag{2.7}$$

Equation (2.6) is a dynamical equation for the evolution of the scalar field; in order to solve for the dynamics of the system, one must solve this equation simultaneously with the Friedmann Equations (2.5) and the continuity equation.

2.3.2 Two dynamical variables

It is convenient to define a new set of dimensionless variables:

$$x = \frac{\dot{\phi}}{\sqrt{6}M_{\rm Pl}H}\,, \qquad\qquad y = \frac{\sqrt{V(\phi)}}{\sqrt{3}M_{\rm Pl}H}\,, \tag{2.8}$$

because the energy density of the scalar field can be expressed as:

$$\Omega_\phi = \frac{\rho_\phi}{3M_{\rm Pl}^2H^2} = x^2 + y^2 \tag{2.9}$$

and the equation of state for the scalar field reads:

$$w_\phi = \frac{x^2 - y^2}{x^2 + y^2}. \tag{2.10}$$

Additionally defining combined matter and radiation energy density parameter as:

$$\Omega_{\rm M} = \Omega_{\rm m} + \Omega_{\rm r} = \frac{\rho_{\rm m}}{3M_{\rm Pl}^2H^2} + \frac{\rho_{\rm r}}{3M_{\rm Pl}^2H^2} \tag{2.11}$$

and assuming that spatial curvature is zero, the first Friedmann Equation (2.5a) simplifies as:

$$1 = x^2 + y^2 + \Omega_{\rm M}. \tag{2.12}$$

To study the evolution of the scalar field we can take derivatives of x and y with respect to the number of e-foldings $N = \ln a$, anticipating that such a system can display accelerated exponential expansion. For an exponential potential $V = V_0 e^{-\lambda\phi/M_{\rm Pl}}$ we get:

$$\frac{dx}{dN} = \sqrt{\frac{3}{2}}\lambda y^2 - \frac{3}{2}x\left(w_{\rm M}\left(x^2 + y^2 - 1\right) - x^2 + y^2 + 1\right) \tag{2.13a}$$

$$\frac{dy}{dN} = -\sqrt{\frac{3}{2}}\lambda xy - \frac{3}{2}y\left(w_{\rm M}\left(x^2 + y^2 - 1\right) - x^2 + y^2 - 1\right). \tag{2.13b}$$

In order to analyse the dynamical system (2.13) we first look at the fixed/critical points for different values of the parameters λ (not to be confused with the cosmological constant Λ) and $w_{\rm M}$ (defined as $w_{\rm M} = (\rho_{\rm m}w_{\rm m} + \rho_{\rm r}w_{\rm r})/(\rho_{\rm m} + \rho_{\rm r})$). From the constraint (2.12), it follows that $x^2 + y^2 \leq 1$ because $\Omega_{\rm M}$ is always positive for the form of the potential we use. Every solution with non-zero y can be positive or negative in y, since $y^2 \sim V$. The part of parameter space in which y is negative corresponds to a contracting universe. Because the phase plane is symmetric with respect to the x-axis, we will only consider its upper

part. This implies that trajectories in phase plane are limited to the upper half of the unit disc. Fixed points are defined as:

$$\frac{dx}{dN} = 0 \,, \qquad \frac{dy}{dN} = 0 \,. \tag{2.14}$$

There are five such critical points; their coordinates and values of the associated physical parameters are listed in Table (2.1).

Table 2.1: Coordinates and properties of fixed points.

	x_*	y_*	w_{eff}	Ω_ϕ	Ω_{M}
A	0	0	w_{M}	0	1
B_1	1	0	1	1	0
B_2	-1	0	1	1	0
D	$\lambda/\sqrt{6}$	$\sqrt{1-\lambda^2/6}$	$\lambda^2/3-1$	1	0
E	$\sqrt{3/2}(w_{\text{M}}+1)/\lambda$	$\sqrt{3/2(1-w_{\text{M}}^2)}/\lambda$	w_{M}	$3(w_{\text{M}}+1)/\lambda^2$	$1-3(w_{\text{M}}+1)/\lambda^2$

The value of the parameter λ can consequently be divided into three qualitatively different cases:

- ($\lambda < \sqrt{3(w_{\text{M}}+1)}$) All trajectories are drawn to the point **D** which is a *stable* attractor.
- ($\sqrt{3(w_{\text{M}}+1)} < \lambda < \sqrt{6}$) Point **E** becomes a *spiral* attractor. **D** is still present.
- ($\sqrt{6} < \lambda$) **D** is no longer defined and $\mathbf{B_1}$ becomes a *saddle point*.

The solutions of Equations (2.13) for these three cases are illustrated in figure (2.1). We have defined w_{M} to be a combination of pressureless dust (with $w_{\text{M}} = 0$) and radiation ($w_{\text{M}} = 1/3$) so its values can only lie between these two values but in the most general case (including more exotic equations of state) its value could lie outside this range. The specific cases shown in the figures (2.1) all have $w_{\text{M}} = 0$. The value of this parameter only slightly affects the position of the fixed point **E** (and none others). For higher values of w_{M} points **E** and **D** merge at higher λ. For a limiting case $w_{\text{M}} = 1$ (that extends beyond our analysis) point **E** merges with **D** exactly at the point $\mathbf{B_1}$ so it is never inside the half disc.

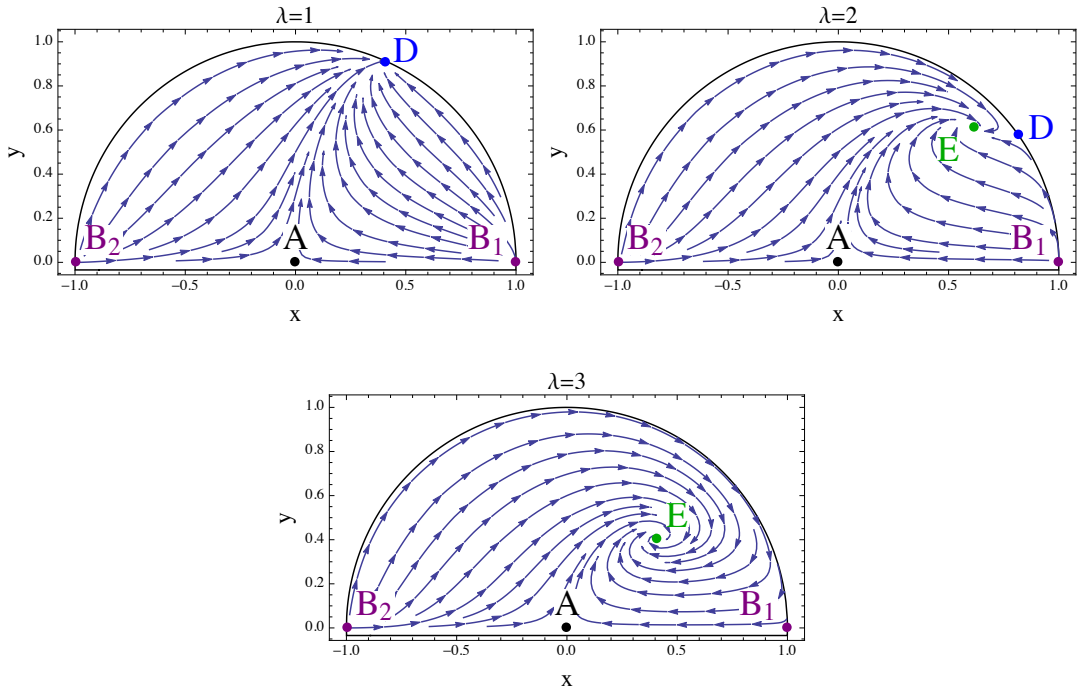

Figure 2.1: Phase planes for three qualitatively different cases of λ and $w_{\rm M} = 0$ as discussed in the text.

2.4 The Role of Curvature

2.4.1 Three dynamical variables

In this subsection we introduce spatial curvature into dynamical system, while still keeping matter and radiation as one variable and considering a scalar field described as an exponential potential. We define new variables to construct a generalization of the two-dimensional phase plane discussed in the previous subsection into a three-dimensional phase space:

$$x = \frac{\dot{\phi}}{\sqrt{6}M_{\rm Pl}H}\,, \qquad y = \frac{\sqrt{V(\phi)}}{\sqrt{3}M_{\rm Pl}H}\,, \qquad z = \frac{K}{a^2H^2}\,. \tag{2.15}$$

Definitions of Ω_ϕ, w_ϕ, $\Omega_{\rm M}$ and $w_{\rm M}$ are identical to those in the previous subsection. The first Friedmann Equation is now expressed as:

$$1 = x^2 + y^2 - z + \Omega_{\rm M}. \tag{2.16}$$

Note that z is not squared in this definition. If z were defined in such a manner that it was squared in the above equation then all solutions with negative K would correspond to solutions with imaginary z. The minus sign in front z has no physical significance; our definition corresponds to $\Omega_K = -z$. With the introduction of the curvature, ratio of the

Friedmann Equations becomes:

$$\frac{\dot{H}}{H^2} = \frac{3}{2}\left(w_{\mathrm{M}}\left(x^2+y^2-z-1\right)-x^2+y^2-1\right)-\frac{1}{2}z \tag{2.17}$$

and the effective equation-of-state parameter can be expressed as:

$$w_{\mathrm{eff}} = \frac{P_\phi + P_{\mathrm{M}}}{\rho_\phi + \rho_{\mathrm{M}}} = \frac{x^2 - y^2 + w_{\mathrm{M}}(1-x^2-y^2+z)}{1+z} \tag{2.18}$$

The evolution of the dynamical system is now described by a system of three coupled differential equations:

$$\frac{dx}{dN} = \sqrt{\frac{3}{2}}\lambda y^2 - \frac{1}{2}x\left(3w_{\mathrm{M}}\left(x^2+y^2-z-1\right)-3x^2+3y^2-z+3\right) \tag{2.19a}$$

$$\frac{dy}{dN} = \frac{1}{2}y\left(-3w_{\mathrm{M}}\left(x^2+y^2-z-1\right)+3x^2-\sqrt{6}\lambda x-3y^2+z+3\right) \tag{2.19b}$$

$$\frac{dz}{dN} = z\left(-3w_{\mathrm{M}}\left(x^2+y^2-z-1\right)+3x^2-3y^2+z+1\right). \tag{2.19c}$$

2.4.2 Phase space analysis, fixed points and their stability

In this case under consideration the constraint $x^2+y^2 \leq 1$ holds only in the plane $z=0$. The general constraint is $x^2+y^2-z \leq 1$ and it defines a parabolic surface in the space of parameters x, y, z. All trajectories must lie above this parabolic surface; they are confined either to the plane $z=0$, where the curvature is zero, or to the part of the space where $z>0$ and K has a positive sign, or to the finite part of the space between the parabolic surface and the plane $z=0$ with a negative z-component and thus a negative curvature parameter K. Because this parameter can not change sign in our model, no trajectories can cross from $z>0$ to $z<0$ or vice-versa. Figures (2.2) show solutions for four different case of parameter λ. Again, we ignore w_{M} by setting it to zero.

Inspection of the fixed points in this new system shows that all fixed points we had before are preserved, when the newly-added additional z is fixed at $z=0$. In addition, however, there are now two new fixed points: **C** and **F**. The eigenvalues corresponding to these points are obtained by extending the matrix (2.27) to describe three variables; the additional dimension of the parameter space requires that there will be an additional eigenvalue. If that eigenvalue is positive, then the fixed point is repulsive in the new direction and if it is negative, the fixed point is attractive. For a point to be an attractor, all the eigenvalues must be negative at that point. If at least one is positive, then trajectories

will be drawn away in at least one direction.

Point A is the matter dominated solution where all energy density is in $\Omega_{\rm M}$. At this point the only contribution to the effective equation of state parameter comes from the matter sector, so $w_{\rm eff} = w_{\rm M}$. The eigenvalues of this point are $[3(w_{\rm M}-1)/2, 3(w_{\rm M}+1)/2, (1+3w_{\rm M})]$ so the point is a saddle for all values of λ, as long as $w_{\rm M} < 1$. It is attractive for the trajectories along the x-axis and repulsive for others. In the limit case of initial potential being exactly 0 (the trajectories that start exactly on the x-axis) this point is an attractor.

Points $\mathbf{B_1}$ and $\mathbf{B_2}$ represent solutions in which the universe is dominated by the kinetic energy of the scalar field: $\Omega_\phi = 1$. Here the effective equation-of-state parameter is constant and the scale factor behaves as $a \propto t^{2/3}$. Eigenvalues for stability are $[3(1-w_{\rm M}), \sqrt{3/2}\lambda \mp 3, 4]$ with the minus sign for $\mathbf{B_1}$ and plus for $\mathbf{B_2}$. This means that $\mathbf{B_2}$ is always repulsive and $\mathbf{B_1}$ repulsive for $\lambda < \sqrt{6}$ and a saddle for $\lambda > \sqrt{6}$.

Point C is new compared to the two-dimensional case and corresponds to a curvature-dominated solution; all the energy density resides in Ω_K. This solution is trivial, because it does not involve any matter or the scalar field. The point is a saddle for all values of parameters; its eigenvalues are $[-2, 1, -(1+3w_{\rm M})]$.

Point D is a solution where the universe is dominated by the scalar field. All energy density is in $\Omega_\phi = x^2 + y^2 = 1$, with $\Omega_M = 0$. The effective parameter of state is $w_{\rm eff} = \lambda^2/3 - 1$, so the universe is accelerating for $\lambda < \sqrt{2}$. In the limit case $\lambda \to 0$, this solution corresponds to the de Sitter expansion dominated by the cosmological constant. This fixed point lies in the $z = 0$ plane, at the edge of the half disc and it moves from $(x = 0, y = 1)$ for $\lambda = 0$ to $(x = 1, y = 0)$ for $\lambda = \sqrt{6}$. After this value of λ it is not defined anymore. The eigenvalues are $[(\lambda^2-6)/2, \lambda^2 - 3(w_{\rm M}-1), \lambda^2 - 2]$ which means that the point is attractive for all trajectories with $z \leq 0$ and some with $z > 0$ for $\lambda < \sqrt{2}$. It is also an attractor for trajectories in the plane $z = 0$ for $\sqrt{2} < \lambda < \sqrt{3(w_{\rm M}+1)}$, and a saddle for $\sqrt{3(w_{\rm M}+1)} < \lambda < \sqrt{6}$. The case of $\lambda < \sqrt{2}$ is especially interesting because in this setup even some of the trajectories that start with a positive amount of curvature end up in the inflationary solution (most of the trajectories which start with the positive curvature evolve to a state with infinite K, i.e. the universe collapses). This demonstrates that "closed" does not imply "finite".

Point E is the so-called "tracking" solution. Both Ω_ϕ and Ω_M are between 0 and 1, and the effective equation-of-state parameter matches that of the matter: $w_\mathrm{eff} = w_\mathrm{M}$. This means that the universe expands as if it were matter dominated and there is no accelerated expansion. This point is, however, interesting because the scalar field is still present; some of the energy density in stored in Ω_ϕ. This fixed point lies in the $z = 0$ plane where both its coordinates are infinite for $\lambda = 0$. Since that is outside of the half disc, it is not relevant for this analysis. The point only becomes relevant as λ becomes larger than $\sqrt{3(w_\mathrm{M}+1)}$. At this value **E** crosses **D** and enters the half disc. Analysis of the stability shows that for $\lambda > \sqrt{3(w_\mathrm{M}+1)}$ two of the eigenvalues are complex conjugates of each other. This means that for the trajectories in the $z = 0$ plane this point is a stable spiral. The additional eigenvalue is always positive so all other trajectories are repelled.

Point F The effective equation-of-state parameter in point **F** is always $w_\mathrm{eff} = -1/3$. This corresponds to the scale factor being linearly proportional to t. The matter-energy density vanishes here so the point always lies exactly on the parabolic surface $x^2 + y^2 - z = 1$. The corresponding eigenvalues are $[-3w_\mathrm{M} - 1, -\sqrt{8\lambda^4 - 3\lambda^6}/\lambda^3 - 1, \sqrt{8\lambda^4 - 3\lambda^6}/\lambda^3 - 1]$ which results in this point being either a saddle, attractor or a stable spiral, depending on the value of λ. This is the analogue of the tracking solution (point **E**) for the case where the universe behaves as if curvature were the only component. This implies $a \propto t$.

Table 2.2: List of fixed points and theirr properties for the three dimensional case.

	x_*	y_*	z_*	w_eff	Ω_ϕ	Ω_M	Ω_K
A	0	0	0	w_M	0	1	0
B_1	1	0	0	1	1	0	0
B_2	-1	0	0	1	1	0	0
C	0	0	-1	undefined	0	0	1
D	$\lambda/\sqrt{6}$	$\sqrt{1-\lambda^2/6}$	0	$\lambda^2/3 - 1$	1	0	0
E	$\frac{\sqrt{3/2}(w_\mathrm{M}+1)}{\lambda}$	$\frac{\sqrt{3/2(1-w_\mathrm{M}^2)}}{\lambda}$	0	w_M	$\frac{3(w_\mathrm{M}+1)}{\lambda^2}$	$1 - \frac{3(w_\mathrm{M}+1)}{\lambda^2}$	0
F	$\sqrt{2/3}/\lambda$	$2/(\sqrt{3}\lambda)$	$2/\lambda^2 - 1$	$-1/3$	$2/\lambda^2$	0	$1 - 2/\lambda^2$

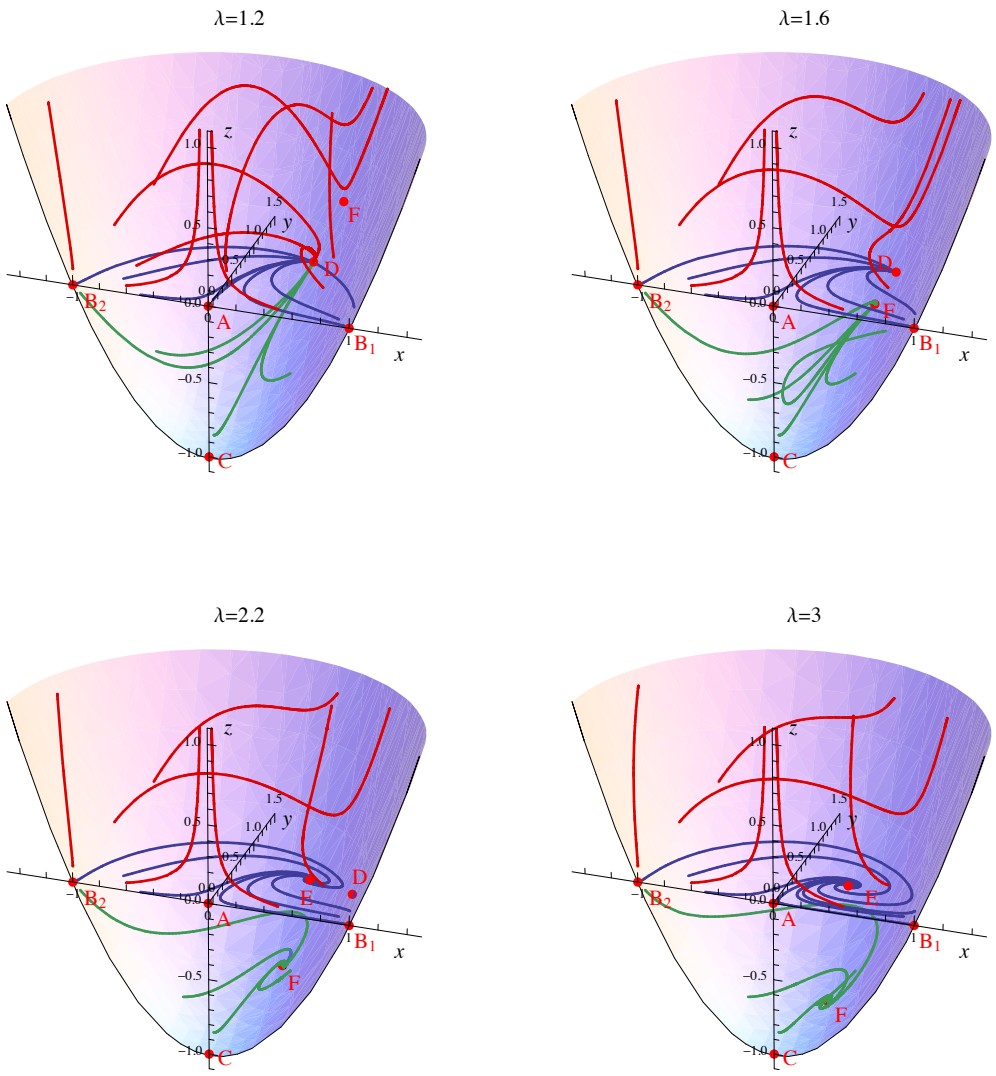

Figure 2.2: Phase spaces for four different λ and $w_{\rm M} = 0$. Valid phase space is limited by the parabolical surface: all valid trajectories lie above it. Trajectories in the $x - y$ plane (where $z = 0$) are shown in blue. Green trajectories lie between this plane and the parabolic surface. Since $z = -\Omega_K = K/(a^2H^2)$, green trajectories represent part of the phase space with negative curvature. Red trajectories are bounded to the part of the space where $z > 0$ which corresponds to $K > 0$. Point **E** lies under the parabolic surface for the first two cases, so it's not shown in the plots.

Four qualitatively different cases of λ are distinguishable:

- ($\lambda < \sqrt{2}$) There are 6 fixed points (all except **E**, which is outside of allowed region). Point **D** is the attractor for all of $z \leq 0$ part of the space and some trajectories in $z > 0$. **F** has positive z-component and is a saddle.

- ($\sqrt{2} < \lambda < \sqrt{3(w_{\mathrm{M}} + 1)}$) There are still the same 6 fixed points but the z-component of **F** is now negative. This point is a stable attractor for all trajectories with $z < 0$. For trajectories that lie in the plane $z = 0$ the attractor is point **D**, and trajectories with $z > 0$ don't converge.

- ($\sqrt{3(w_{\mathrm{M}} + 1)} < \lambda < \sqrt{6}$) Point **D** becomes a saddle, **E** enters the allowed region and becomes attractive for trajectories in the plane, while trajectories with $z > 0$ diverge. Two of the eigenvalues of point **F** are now complex conjugates of each other while the third is negative, so this point is a stable spiral in three dimensions.

- ($\sqrt{6} < \lambda$) At $\lambda = \sqrt{6}$ The significance of this last case is that point **D** merges with $\mathbf{B_1}$ and disappears. $\mathbf{B_1}$ is now a saddle point in the plane.

2.4.3 Evolution of the Equation of State

For the same cases of λ we plot trajectories that correspond to initial conditions that give flat, open and closed universe models. These are shown in figures (2.3). Note that we used the same initial conditions for all four cases. In the first case all curves converge. For all other values of λ the equation-of-state parameter diverges for $K > 0$. For $K < 0$ trajectories in phase space are drawn towards point **F**, where $w_{\mathrm{eff}} = -1/3$. For $K = 0$ they can either end up in the point **D** (first two values of λ) or **E** (third and fourth case of λ).

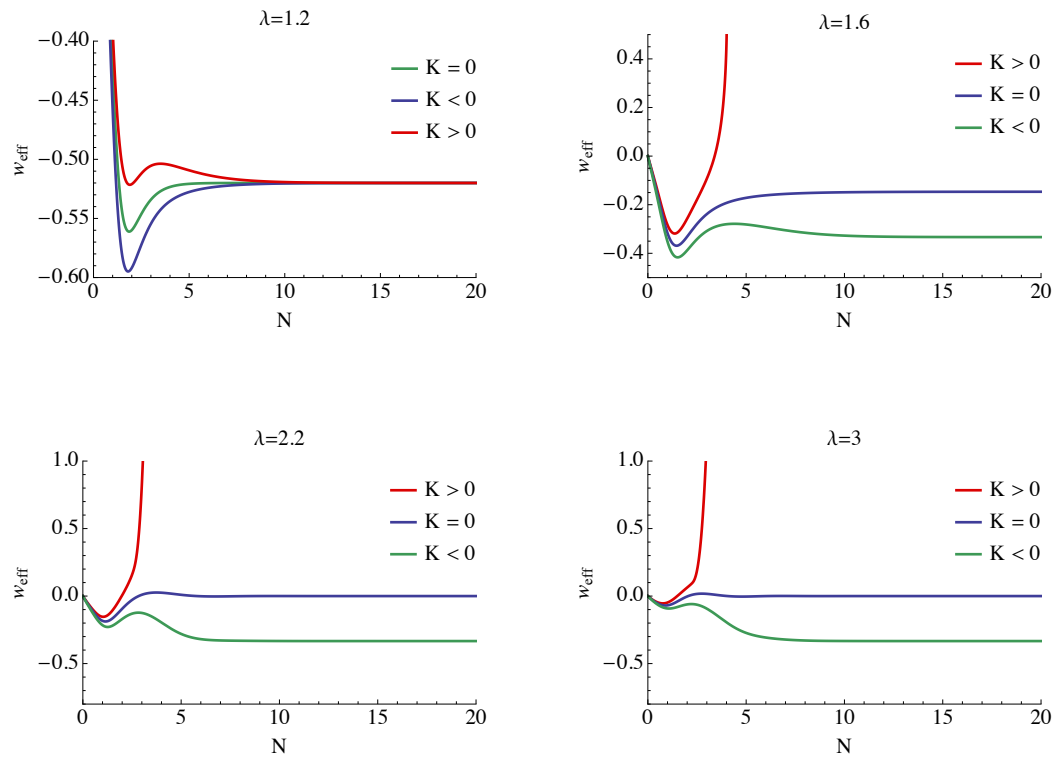

Figure 2.3: Evolution of equation-of-state parameter over 20 e-foldings (N) for four different cases of λ.

2.5 Conclusions

We explored a single-field quintessence model with exponential potential and canonical kinetic term in presence of a FLRW metric and overall (positive or negative) spatial curvature. In the Friedmann Equations, the term with spatial curvature is dynamical, so we introduced a new variable and generalized two-dimensional case that holds for a flat geometry to three dimensions.

In comparison to the model without curvature there are two new fixed points. These have been noticed before (e.g. Burd and Barrow (1988)) but their behaviour is clearer when viewed in terms of the parametrization we use. One of them is trivial, in that it corresponds to a universe where entire energy density is dominated by the curvature. This fixed point is not attractive. The other fixed point corresponds to a universe where energy density is a combination of curvature and scalar field (but no matter). The ratio between them depends on the parameter of the exponential potential. This fixed point is interesting, because it is attractive for all trajectories with negative curvature term for $\lambda > \sqrt{2}$. We have thus established that there is a natural configuration of this system that corresponds to a specific value of w. Although we know that the energy density of the Universe today is almost critical (so there is very little or no curvature), this fixed point

might still be interesting for the cases where λ is just above $\sqrt{2}$ and so energy density is dominated by the scalar field.

The only problem with relating this solution to our observed reality is that equation-of-state parameter in this point is $-1/3$, but we know that the present value is very close to -1. Nonetheless, the attractor solution **D** is an accelerating solution for flat, negatively curved and some positively curved cases. The corresponding equation-of-state parameter is close to the value $w = -1$ in the limit $\lambda \to 0$, but for any value of $\lambda < \sqrt{2}$ it corresponds to $w < -1/3$ so this is at least qualitatively applicable to dark energy.

We have only investigated one particular and rather simple model, but this sort of curvature inclusive analysis is applicable to other, potentially more complicated models that might exhibit a much richer dynamical interplay. Cases which might prove amenable to further study on these lines would be scalar fields with a more general potential (Copeland et al., 2009), non-canonical terms, with multiple scalar fields, with globally anisotropic metrics (i.e. the Bianchi models) (Fadragas et al., 2014), e.g. the Kantowski-Sachs model (Coley and Goliath, 2000), and models based on exact inhomogeneous cosmologies. Such models would of course introduce more than one extra parameter, so the resulting phase portraits would involve more than three dimensions and their analysis would entail considerably greater complexity.

Acknowledgements

PC gratefully acknowledges support from the UK Science and Technology Facilities Council (STFC) under grant reference ST/L000652/1. MG would like to thank Nicola Tamanini for useful comments.

2.A Two dynamical variables and stability of fixed points

After introducing new variables as in Equation (2.8) for a general potential $V(\phi)$ and using the Klein-Gordon Equation (2.6), the derivatives with respect to N are:

$$\frac{dx}{dN} = -\frac{\dot{\phi}}{\sqrt{6}M_{\rm Pl}H}\left(3 + \frac{\dot{H}}{H^2}\right) - \frac{V_{,\phi}}{\sqrt{6}M_{\rm Pl}H^2} \tag{2.20a}$$

$$\frac{dy}{dN} = \frac{V_{,\phi}\,\dot{\phi}}{2\sqrt{3}M_{\rm Pl}\sqrt{V}H^2} - \frac{\sqrt{V}}{\sqrt{3}M_{\rm Pl}H}\frac{\dot{H}}{H^2}. \tag{2.20b}$$

Defining parameter λ as $\lambda = -M_{\rm Pl}V_{,\phi}/V$ is especially convenient because this parameter is constant for the exponential potential. Using this potential and eliminating $\Omega_{\rm M}$ with the use of constraint (2.12), the ratio of the Friedmann Equations $\dot{H}/H^2$ can be expressed, in terms of x and y, as:

$$\frac{\dot{H}}{H^2} = \frac{3}{2}\left(w_{\rm M}\left(x^2+y^2-1\right) - x^2 + y^2 - 1\right), \tag{2.21}$$

where we define $w_{\rm M}$ to be the combined equation-of-state parameter for a fluid component taken to describe both matter and radiation:

$$w_{\rm M} = \frac{\rho_{\rm m}w_{\rm m} + \rho_{\rm r}w_{\rm r}}{\rho_{\rm m}+\rho_{\rm r}}. \tag{2.22}$$

Derivatives of x and y are hence expressed, for the exponential potential as (2.13). This provides a useful way to express the evolution of both w_ϕ and Ω_ϕ:

$$w_\phi' = (w_\phi - 1)\left(-\lambda\sqrt{3(1+w_\phi)\Omega_\phi} + 3(1+w_\phi)\right) \tag{2.23a}$$

$$\Omega_\phi' = 3(\Omega_\phi - 1)\Omega_\phi(w_\phi - w_{\rm M}), \tag{2.23b}$$

where the prime stands for differentiation with respect to N. Additionally, by defining $\Gamma = VV_{,\phi\phi}/V_{,\phi}^2$ we can obtain the derivative of λ:

$$\lambda' = -\lambda^2(\Gamma - 1)\sqrt{3(1+w_\phi)\Omega_\phi}. \tag{2.24}$$

For the exponential potential λ is constant, so λ' does not carry any additional information in this case. In the fixed points the effective equation-of-state parameter, defined as

$$w_{\rm eff} = \frac{P_\phi + P_{\rm M}}{\rho_\phi + \rho_{\rm M}} = x^2 - y^2 + w_{\rm M}(1 - x^2 - y^2) \tag{2.25}$$

is constant so we can easily integrate Equation (2.21) to see how scale factor changes with time:

$$a \propto t^{\frac{2}{3(1+w_{\rm eff})}}. \tag{2.26}$$

Note that this only holds if the system is at one of the fixed points. In other cases Equation (2.21) has to be integrated numerically because its right-hand side is not constant. However, it is still sensible to define an equation-of-state parameter $w_{\rm eff}$ even outside these points. For $w_{\rm eff} = -1/3$ the scale factor will have a linear dependance on time; values

larger or smaller than that will give decelerated and accelerated expansion, respectively.

We investigate the stability of the fixed points by finding eigenvalues of the matrix, evaluated at the fixed point (x_*, y_*):

$$M = \left[\begin{array}{cc} \frac{\partial f_x}{\partial x} & \frac{\partial f_x}{\partial y} \\ \frac{\partial f_y}{\partial x} & \frac{\partial f_y}{\partial y} \end{array} \right]_{x_*, y_*} , \tag{2.27}$$

where $f_i = di/dN$ stands for the terms on the right-hand side of Equations (2.13). A fixed point is stable (attractive) if both eigenvalues are negative, non-stable (repulsive) if they are positive and a saddle (attractive in one direction and repulsive in others) if they have the opposite sign. If the two eigenvalues are complex conjugates of each other, then the fixed point is a stable spiral.

In the case of two variables there are five such critical points; their coordinates and values of the associated physical parameters are listed in Table (2.1). Their existence and properties depend on the values of λ and w_{M}.

Spherically Symmetric N-body Simulations with General Relativistic Dynamics

Julian Adamek, Mateja Gosenca, and Shaun Hotchkiss

Abstract

Within a cosmological context, we study the behaviour of collisionless particles in the weak field approximation to General Relativity, allowing for large gradients of the fields and relativistic velocities for the particles. We consider a spherically symmetric setup such that high resolution simulations are possible with minimal computational resources. We test our formalism by comparing it to two exact solutions: the Schwarzschild solution and the Lemaître-Tolman-Bondi model. In order to make the comparison we consider redshifts and lensing angles of photons passing through the simulation. These are both observable quantities and hence are gauge independent. We demonstrate that our scheme is more accurate than a Newtonian scheme, correctly reproducing the leading-order post-Newtonian correction. In addition, our setup is able to handle shell-crossings, which is not possible within a fluid model. Furthermore, by introducing angular momentum, we find configurations corresponding to bound objects which may prove useful for numerical studies of the effects of modified gravity, dynamical dark energy models or even compact bound objects within General Relativity.

3.1 Introduction

Recent results from the Planck mission (Ade et al., 2015), BOSS (Anderson et al., 2014; Busca et al., 2013; Samushia et al., 2013), WiggleZ survey (Blake et al., 2012), CFHTlenS (Kilbinger et al., 2013) and SNLS (Betoule et al., 2014) have consolidated the ΛCDM concordance model of cosmology as providing a very good fit to observations. However, this model is characterized by two semi-phenomenological ingredients – cold dark matter (CDM) and a cosmological constant (Λ) – whose true nature still needs to be determined

at the fundamental level. With the reach of linear analysis now being nearly exhausted, phenomena at nonlinear scales can help to make progress. On the observational side, large surveys such as Euclid (Laureijs et al., 2011), DES (Abbott et al., 2005), LSST (Abell et al., 2009) and SKA (Carilli and Rawlings, 2004) will make significant progress analysing these non-linear scales. This puts the onus on the theoretical side to understand precisely what we expect these surveys to see. Due to the non-linearity, numerical simulations will be a necessary tool to probe this regime.

The N-body codes used for the study of cosmic large scale structure normally employ Newton's law of gravitation. One expects that this approximation works well as long as perturbations are generated by nonrelativistic matter only. This is true if dark energy is indeed a cosmological constant and dark matter is some heavy fundamental particle (like in the WIMP scenario). However, since these facts are not established it seems that by using the Newtonian approximation we are unable to access a viable part of model space.

In fact, even within the realm of known physics this approximation will break down due to the existence of very light, but still massive, neutrinos. In principle, the initial conditions of simulations can be set late enough that neutrinos have already become non-relativistic; however, this can be so late that the cold dark matter has already begun to cluster significantly. Therefore, relativistic effects are already important in order to rigorously model the effects of neutrino masses in cosmology.

In an effort to address these shortcomings, a relativistic framework for N-body simulations has recently been developed (Adamek et al., 2013, 2014b). This framework is based on a weak-field expansion of Einstein's equations, similar to the one proposed in (Green and Wald, 2011, 2012). It does not require a particular form of stress-energy and relies solely on the assumption that gravitational fields are weak, at least at large scales. Therefore, it is applicable[1] to a much larger set of models, including hot dark matter (Davis et al., 1992; Abazajian et al., 2001) and many types of dynamical dark energy (Copeland et al., 2006).

Before investing significant computational resources in order to do a full-scale cosmological simulation it is interesting to study the relativistic effects in a simplified setup. Here we will consider the case of a single, isolated, spherically symmetric structure which could, for instance, be a model for a cosmological void or a galaxy cluster. The idealization to exact spherical symmetry drastically reduces computational requirements, allowing high-resolution simulations to be carried out at negligible cost. Furthermore, the numerical

[1] Note however that in some models the stress energy tensor may need to be modelled by a method other than simple N-body particles.

scheme can be thoroughly verified by comparing to several known exact solutions. When comparing to exact solutions, structures can also be allowed to evolve into regimes where metric perturbations do become large and the framework breaks down, allowing us to probe the boundaries of where the framework can and cannot be trusted.

Our approach is in some sense complementary to existing methods for the numerical solution of Einstein's equations. For instance, the BSSN formalism (Shibata and Nakamura, 1995; Baumgarte and Shapiro, 1999; Rekier et al., 2015) can probe the strong field regime, but existing implementations rely on a fluid description for matter. Our N-body method, on the other hand, allows us to study matter configurations with highly nontrivial phase space distributions.

In section 3.2 we introduce the relativistic framework and study some simple spherically symmetric setups. We first consider a Schwarzschild solution to confirm that the relativistic potentials are calculated accurately in vacuum. We then add nonrelativistic matter and compare our simulations to the exact Lemaître-Tolman-Bondi models which describe spherically symmetric solutions with a dust fluid. In order to avoid gauge issues, we construct several physical observables which can be compared without ambiguity. We note that the fluid solutions break down at the formation of caustics, but our relativistic framework remains valid and can thus probe settings beyond the fluid approximation. Without support from pressure or angular motion, overdensities tend to collapse quickly and can not easily form stable bound objects. In section 3.3, we propose a way to introduce angular motion without breaking spherical symmetry. This is achieved by arranging the motion of the particles such that they all individually have angular momentum, but the total angular momentum of the system remains zero. We demonstrate that one can find configurations corresponding to bound objects. Such configurations may be useful laboratories to study the effects of modified gravity, dynamical dark energy models, or even the early stages of the formation of primordial blackholes (Hawking, 1971; Carr and Hawking, 1974), or ultra compact mini-haloes (Berezinsky et al., 2003; Bunn and White, 1997; Ricotti and Gould, 2009), within ordinary gravity.

3.2 The Model

The perturbed Friedmann-Lemaître-Robertson-Walker (FLRW) metric, in spherical coordinates and longitudinal gauge, is:

$$\mathrm{d}s^2 = -a^2(\tau)\left[1+2\Psi(\tau,r)\right]\mathrm{d}\tau^2 + a^2(\tau)\left[1-2\Phi(\tau,r)\right]\left[\mathrm{d}r^2 + r^2\mathrm{d}\Omega^2\right], \tag{3.1}$$

where τ is the conformal time, a is the scale factor and we impose spherical symmetry of the perturbations by requiring that the Bardeen potentials $\Phi(\tau, r)$ and $\Psi(\tau, r)$ depend only on the radial coordinate and time. We have also assumed a spatially flat background although it would be easy to generalize our model to allow for open or closed geometries.

We examine this metric in the regime where gravitational fields are weak. In other words, we are interested in perturbations caused by structures that remain much larger than their Schwarzschild radius. Such a weak-field setting allows for a systematic expansion of the various equations of motion (including Einstein's field equations) in terms of metric perturbation variables. We will follow an approach studied in (Adamek et al., 2013) which takes into account the most important relativistic terms.

This approach can be summarized as follows: first, all equations are expanded in terms of the metric perturbations – in our case Φ and Ψ – and all terms up to first order are kept without distinction. At higher orders, however, one only wants to keep the most relevant terms. Noting that linear perturbation theory is accurate on the largest scales (close to or beyond the horizon) the only higher order terms that we will keep are those which may become large at *small* scales. These terms will be those with two spatial derivatives,[2] since a derivative will effectively multiply a term by an inverse power of a length scale. To arrive at a tractable set of equations that still contains the most important relativistic corrections we will therefore add all second order terms with two spatial derivatives and no terms of any higher order. Although there are scenarios where terms of higher than quadratic order can dominate over the linear terms (e.g. $\Phi_{,ij}\Phi^2$ if $\Phi_{,ij} > \delta_{ij}/\Phi$) these higher order terms will always be sub-dominant to the largest *quadratic* order terms that we *do* include. Further details on this approximation scheme can be found in (Adamek et al., 2013).

It is important to emphasise that any perturbations of the stress-energy tensor, including momenta, are allowed to be arbitrarily large. The perturbative expansion is only carried out in terms of gravitational fields and we make no assumptions about other

[2] Note that Einstein's equations are second order differential equations, therefore no terms will have more than two derivatives.

perturbations. For instance, our solar system perfectly fits into this scheme since the gravitational field of the sun remains well within the weak-field regime, despite the fact that its density is some thirty orders of magnitude larger than the mean density of the Universe.

Using the "time-time" component of Einstein's equations, $G^0_0 = 8\pi G T^0_0$, we obtain an equation for the metric perturbations:

$$\Phi_{,rr} + \frac{2}{r}\Phi_{,r} - 3\mathcal{H}\Phi_{,\tau} - 3\mathcal{H}^2(\Phi - \chi) + \frac{3}{2}(\Phi_{,r})^2 = -4\pi G a^2(1 - 4\Phi)\delta T^0_0 \,, \tag{3.2}$$

where commas denote partial derivatives with respect to r or τ. Note that, in a spherical coordinate system as the one used here, second spatial derivatives can give rise to terms like $\Phi_{,r}/r$. We will treat these terms like second derivatives in our expansion scheme, i.e. a factor $1/r$ will effectively be counted like a spatial derivative. We also introduced the conformal Hubble parameter $\mathcal{H} = \mathrm{d}\ln a/\mathrm{d}\tau$ and the difference of the potentials as $\chi = \Phi - \Psi$. On the right-hand side, δT^0_0 stands for the perturbations of the stress-energy tensor, $\delta T^0_0 = T^0_0 - \bar{T}^0_0$. We will only consider contributions from massive particles (e.g. cold dark matter). The background model is governed by the Friedmann equation

$$\mathcal{H}^2 = -\frac{8\pi G}{3} a^2 \bar{T}^0_0 \,. \tag{3.3}$$

Another equation comes from the traceless part of the "space-space" components of Einstein's equations, $G^i_j - \frac{1}{3}\delta^i_j G^k_k = 8\pi G\left(T^i_j - \frac{1}{3}\delta^i_j T^k_k\right)$, and reads:

$$\chi_{,rr} - \frac{1}{r}\chi_{,r} + \chi^2_{,r} + 2\Phi^2_{,r} + 2\left(\Phi_{,rr} - \frac{1}{r}\Phi_{,r}\right)(2\Phi - \chi) = 12\pi G a^2(1 - 2\chi)\Pi_{rr} \,, \tag{3.4}$$

where Π_{rr} is the radial component of the anisotropic stress, defined for a general coordinate system as:

$$\Pi_{ij} = \delta_{ik} T^k_j - \frac{1}{3}\delta_{ij} T^k_k \,. \tag{3.5}$$

Latin indices denote spatial coordinates only. As a consequence of spherical symmetry the anisotropic stress is purely longitudinal in our setting.

The stress-energy tensor is derived by varying the action of an ensemble of massive point particles with respect to $\delta g_{\mu\nu}$ (see e.g. equation (2) of (Adamek et al., 2014b)). This gives:

$$T^{\mu\nu} = \sum_n m_{(n)} \frac{\delta^{(3)}(\mathbf{x} - \mathbf{x}_{(n)})}{\sqrt{-g}} \times \left(-g_{\alpha\beta}\frac{\mathrm{d}x^\alpha_{(n)}}{\mathrm{d}\tau}\frac{\mathrm{d}x^\beta_{(n)}}{\mathrm{d}\tau}\right)^{-1/2} \frac{\mathrm{d}x^\mu_{(n)}}{\mathrm{d}\tau}\frac{\mathrm{d}x^\nu_{(n)}}{\mathrm{d}\tau} \,, \tag{3.6}$$

where we sum the contributions of n particles with masses $m_{(n)}$ and spatial positions $\mathbf{x}_{(n)}$, and Greek indices run over all four coordinates of space-time.

For a particle moving in the radial direction we can define a momentum

$$p = \frac{m(1-\Phi)\frac{\mathrm{d}r}{\mathrm{d}\tau}}{\sqrt{1+2\Psi-(1-2\Phi)\left(\frac{\mathrm{d}r}{\mathrm{d}\tau}\right)^2}}\,, \tag{3.7}$$

which is the proper relativistic momentum as measured in a Gaussian orthonormal coordinate frame aligned with our foliation of spacetime[3]. The motivation for this is that it allows us to derive an expression for the stress-energy tensor that is valid (within the bounds of our approximation scheme) even when the particles have arbitrarily high velocities. In particular,

$$T^0_0 = -\frac{1+3\Phi}{4\pi r^2 a^3}\sum_n \delta(r-r_{(n)})\sqrt{m^2_{(n)}+p^2_{(n)}}\,, \tag{3.8}$$

and

$$\Pi_{rr} = \frac{2}{3}\frac{1+3\Phi}{4\pi r^2 a^3}\sum_n \delta(r-r_{(n)})\frac{p^2_{(n)}}{\sqrt{m^2_{(n)}+p^2_{(n)}}}\,. \tag{3.9}$$

As we restrict our solutions to spherical symmetry we can imagine collections of particles as representing spherically symmetric shells with only radial positions. This is because symmetry also requires that the particle distribution function is independent of angular position. We therefore simply dropped the angular coordinates from above expressions and defined the masses such that $m_{(n)}/(4\pi r^2_{(n)})$ is the surface mass density (in coordinate space) of the shell with label n. Thus, each shell accounts for all particles at given radius $r_{(n)}$ with given radial momentum $p_{(n)}$ and we need only sum over shells. Note that, for descriptive ease, from here onwards we will refer to the individual shells as the "particles" of our simulations.

In order to evolve the particle positions one can invert eq. (3.7),

$$\frac{\mathrm{d}r}{\mathrm{d}\tau} = \frac{p}{\sqrt{m^2+p^2}}(1+\Phi+\Psi)\,. \tag{3.10}$$

[3]Explicitly, a Gaussian orthonormal coordinate frame is given by a set of orthonormal basis vectors e^μ_0, e^μ_1, e^μ_2, e^μ_3, $g_{\mu\nu}e^\mu_0 e^\nu_0 = -1$, $g_{\mu\nu}e^\mu_0 e^\nu_i = 0$, $g_{\mu\nu}e^\mu_i e^\nu_j = \delta_{ij}$ with e^μ_0 orthogonal to the space-like hypersurface. The metric in the coordinates defined by this basis locally looks like the Minkowski metric. The momentum p defined in eq. (3.7) is simply the spatial component of the covariant 4-momentum in that coordinate system. If we align e^μ_1 with the radial direction, i.e. $e^\mu_1 \propto \delta^\mu_r$, we can write $p = mu^\mu g_{\mu\nu}e^\nu_1$, where u^μ denotes the covariant 4-velocity.

The geodesic equation for massive particles,

$$\frac{\mathrm{d}^2 x^\mu}{\mathrm{d}s^2} + \Gamma^\mu_{\nu\rho} \frac{\mathrm{d}x^\nu}{\mathrm{d}s} \frac{\mathrm{d}x^\rho}{\mathrm{d}s} = 0\,, \tag{3.11}$$

finally determines the evolution of the momenta as

$$\frac{\mathrm{d}p}{\mathrm{d}\tau} = -(\mathcal{H} - \Phi_{,\tau})p - \Psi_{,r}\sqrt{m^2 + p^2}\,. \tag{3.12}$$

Our aim is to study numerical solutions to the above system of equations. To this end, we adopt a particle-mesh (PM) scheme as used in many cosmological N-body simulations. The "mesh" part of the scheme takes care of the evolution of *fields* such as Φ or χ. All fields are represented approximately by sampling their values on a discrete set of points, hereafter referred to as the "grid". The field equations (3.2), (3.4) are solved on the grid by replacing the differential operators by finite-difference versions thereof.

The "particle" part of the PM scheme, on the other hand, takes care of the evolution of the particle ensemble. The phase-space of fundamental particles is sampled by a much smaller number of N-body particles which can be viewed as discrete elements of phase-space. Hereafter, the term "particle" usually refers to the latter notion. Positions and momenta of particles are real-valued (i.e. they can exist in arbitrary positions between grid points) and the geodesic equation is solved by interpolating field-dependent quantities such as $\Psi_{,r}$ to the particle positions.

Vice versa, a so-called particle-to-mesh projection is required to construct the stress-energy tensor (whose components are treated like a field) from the particle ensemble. This is achieved by replacing $\delta(r - r_{(n)}) \to w(r - r_{(n)})$ in eqs. (3.8), (3.9), where w is a weight function which depends on the projection method. We use the so-called "triangular-shaped particle" (TSP) method where w is constructed using a piecewise linear (triangle-shaped, hence the name) function of the separation. Some details on the projection and interpolation methods can be found in appendix 3.C.

In the following subsections, in order to validate the numerical scheme, we will compare simulations to two well-known exact solutions of Einstein's equations.

3.2.1 The Schwarzschild Solution

The Schwarzschild metric describes the spherically symmetric vacuum solution around a central mass concentration. Within the context of our simulations this metric is suitable

for regions void of particles, and can hence be used to test the implementation of the field equations independently of the particle evolution.

In order to obtain explicit expressions for the two Bardeen potentials, it is useful to write the Schwarzschild solution in so-called "isotropic coordinates" (Eddington, 1924),

$$\mathrm{d}s^2 = -\frac{\left(1-\frac{r_S}{4r}\right)^2}{\left(1+\frac{r_S}{4r}\right)^2}\mathrm{d}t^2 + \left(1+\frac{r_S}{4r}\right)^4\left[\mathrm{d}r^2 + r^2\mathrm{d}\Omega^2\right], \tag{3.13}$$

where $r_S = 2GM$ denotes the Schwarzschild radius.

As long as the mass M is distributed over a central region much larger than r_S, the exterior Schwarzschild solution can be viewed as a perturbation around Minkowski space. Within our simulations, such a background is described by $\bar{T}^0_0 = 0$ and hence $\mathcal{H} = 0$. We can therefore set $a = 1$ and $\tau = t$. In order to obtain a numerical solution we set up a homogeneous ball of particles (much larger than its Schwarzschild radius) in the center of an otherwise empty simulation volume. The Bardeen potentials Ψ and Φ outside of the ball are independent of time, as guaranteed by Birkhoff's theorem. Their behavior in the weak-field regime is given by the large-r expansion of the above exact metric. For $r \gg r_S$ we have

$$\frac{\left(1-\frac{r_S}{4r}\right)^2}{\left(1+\frac{r_S}{4r}\right)^2} = 1+2\Psi(r) = 1-\frac{r_S}{r}+\frac{r_S^2}{2r^2}+\dots, \tag{3.14a}$$

$$\left(1+\frac{r_S}{4r}\right)^4 = 1-2\Phi(r) = 1+\frac{r_S}{r}+\frac{3r_S^2}{8r^2}+\dots. \tag{3.14b}$$

In Figure 3.1 we show some results for Φ and χ obtained with our numerical scheme and compare them to the corresponding analytic results obtained from the exact solution. We only consider the vacuum region outside the central mass concentration. Evidently, our numerical scheme accurately accounts for the leading-order post-Newtonian corrections and is therefore one order (in post-Newtonian counting) better than a purely Newtonian scheme. Using the results of our simulation it would be possible, for instance, to get an accurate prediction for the advance of the perihelion of Mercury.

3.2.2 The Lemaître-Tolman-Bondi Solution

If spacetime is filled with a *dust fluid* then one can construct a spherically symmetric class of exact parametric solutions known as Lemaître-Tolman-Bondi (LTB) models. For our simulation this is equivalent to requiring that particles occupying identical space-time

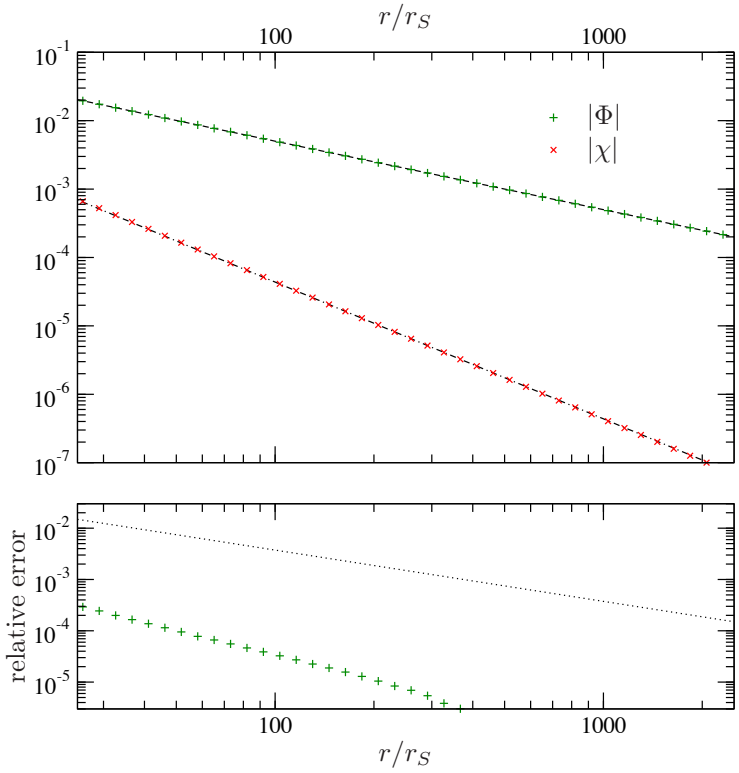

Figure 3.1: Top: numerical results for Φ (green) and $\chi = \Phi - \Psi$ (red) as a function of r/r_S. They are in excellent agreement with the exact result, shown as dashed and dot-dashed lines, respectively. Bottom: relative error of the numerical values of Φ with respect to the exact result (in green). For comparison, the relative error of the Newtonian approximation, $\Phi = -GM/r$, is shown as dotted line (in black).

points also have identical velocities, or more precisely, having a phase space distribution function which, at each spacetime point, is a single Dirac delta-distribution in velocity space. Being exact solutions, these models do not require the density to be nearly homogeneous, allowing the study of strongly non-perturbative settings. However, it is impossible to extend these solutions beyond the point where particle trajectories cross and the phase space distribution function loses its simple delta-distribution character without using a different coordinate system to the comoving-synchronous one used here.

In this coordinate system, the LTB line element reads

$$\mathrm{d}s^2 = -\mathrm{d}t^2 + \frac{[R_{,r}(t,r)]^2}{1+2E(r)}\mathrm{d}r^2 + R^2(t,r)\mathrm{d}\Omega^2\,. \tag{3.15}$$

In order to compare the LTB solutions to our numerical calculations we choose initial conditions such that the density perturbation is linear. In the perturbative regime we can easily work out the coordinate transformation between the synchronous comoving coordinates used to parameterize the LTB solution and the coordinates used in our framework, which are related to the longitudinal gauge [4]. Details can be found in appendix 3.A. A

[4]For a discussion on why this is a coordinate transformation rather than a gauge transformation see

more general treatment of this coordinate transformation has previously been considered in (Van Acoleyen, 2008). Setting initial conditions in this way we can make a comparison between the two physical situations. This procedure does not precisely match the exact LTB solution to the perturbed FLRW solution; however it is sufficient for our purposes of comparing observables in the two physical models. For a more rigorous comparison see (Sussman et al., 2015).

Figures 3.2 and 3.3 show some simulation results. We plotted the evolution of the density contrast, momentum of particles p, scalar perturbation Φ and the difference of the two potentials χ as a function of comoving radius r. The density contrast here is defined as $\rho/\bar{\rho} = T^0_0/\bar{T}^0_0$, where T^0_0 is constructed according to eq. (3.8) and $\bar{T}^0_0$ is taken from the background model. The density, Φ, and χ are quantities projected to the grid with the method described in Appendix 3.C, whereas the momentum portrait shows the momentum for each particle separately. The first set of figures portrays the collapse of a spherically symmetric overdensity and the second set shows the expansion of a spherically symmetric void. The initial densities were set as "compensated tophat profiles", where a central region of constant density contrast is surrounded by a second layer with constant density contrast of opposite sign such that the entire region can be matched onto a homogeneous FLRW exterior solution. In both cases we find χ to be proportional to $\sim \Phi^2$ and negative.

In the expansion of a void, we can also observe a "shell-crossing" which happens when a set of particles moves outwards faster than particles that were initially at a larger radius. As mentioned before, this cannot be described with the comoving synchronous coordinates – it becomes singular as soon as shell crossing occurs. Note that LTB model can also exhibit shell-crossings if constructed with non-comoving coordinates (Plebanski and Krasinski, 2006).

When following the respective solutions into the non-linear regime we face the problem that the coordinate transformation becomes highly nontrivial. This makes it difficult to compare quantities like the density or metric components directly. A good way to proceed is to compute and compare *observables*. In the following section we will discuss some examples in detail.

(Malik and Matravers, 2013).

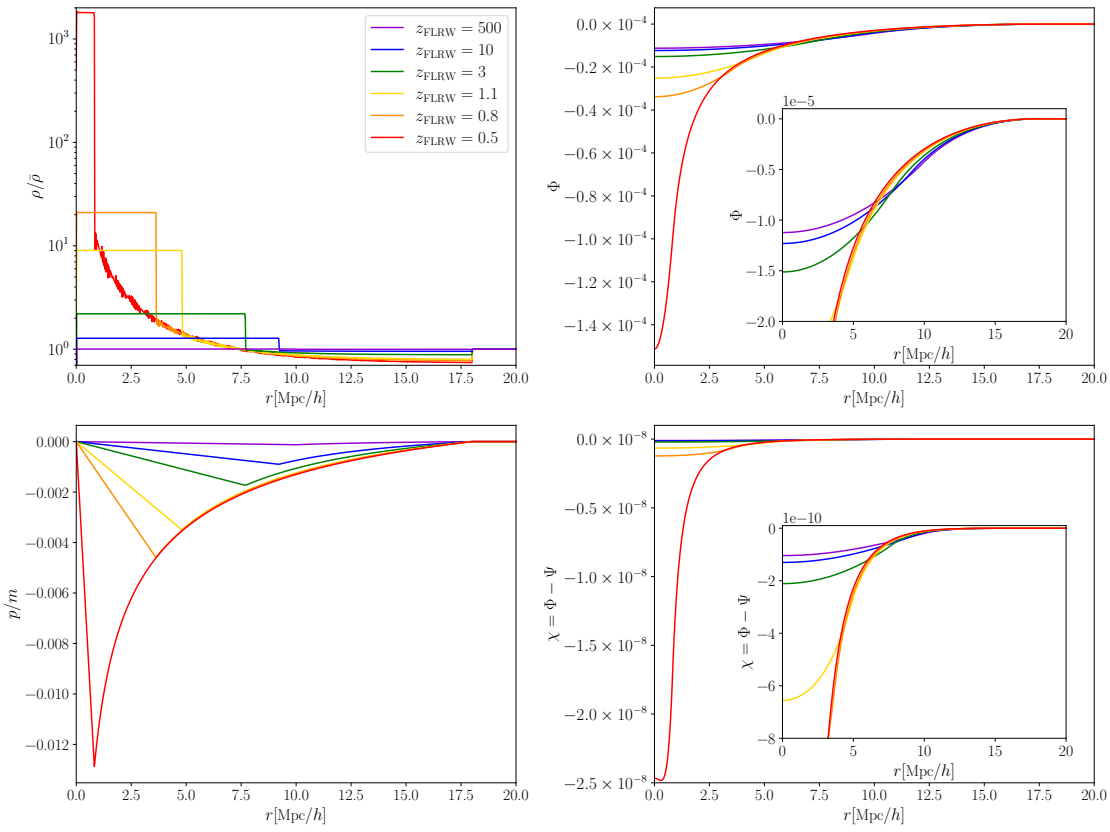

Figure 3.2: Top left: the evolution of the density profile of a spherically symmetric compensated tophat perturbation. Different-coloured lines correspond to outputs at different times in the simulation, parametrised by the background redshift z_{FLRW}. The last output at $z_{\mathrm{FLRW}} = 0.5$ happens just before the collapse occurs. Density plots exhibit some discreteness noise, which is caused by having a finite number of particles. Bottom left: the momentum of the shells moving inwards. Top right: evolution of the underlying scalar metric perturbation Φ. This profile is continuous even where the density has a step. Bottom right: Evolution of the difference of the two potentials $\chi = \Phi - \Psi$. This is a purely relativistic quantity and does not exist in a Newtonian setup. The magnitude of χ is $\sim \Phi^2$. Parameters of the simulation were: size of the box: 20 Mpc/h, initial radii of top-hat overdensity and compensated region, respectively: $r_1 = 6$ Mpc/h, $r_2 = 18$ Mpc/h, initial density contrast of the overdensity: $\delta = 1/200$, initial redshift: $z_{in} = 500$.

3.2.3 Observables

Redshift of radially in-falling source

The first observable we will study is the redshift of a source of light that is moving with the flow of particles surrounding it. We place this source of light at an initial radius r_1 from the center and an observer at r_2, the boundary where the inhomogeneous LTB patch is matched to FLRW. For this example, the source and observer are along the same radial line. The source constantly emits photons at a fixed energy given in the rest frame of the source. As the simulation progresses, we propagate these photons through the simulation volume until they reach the observer. There they are detected and we calculate their

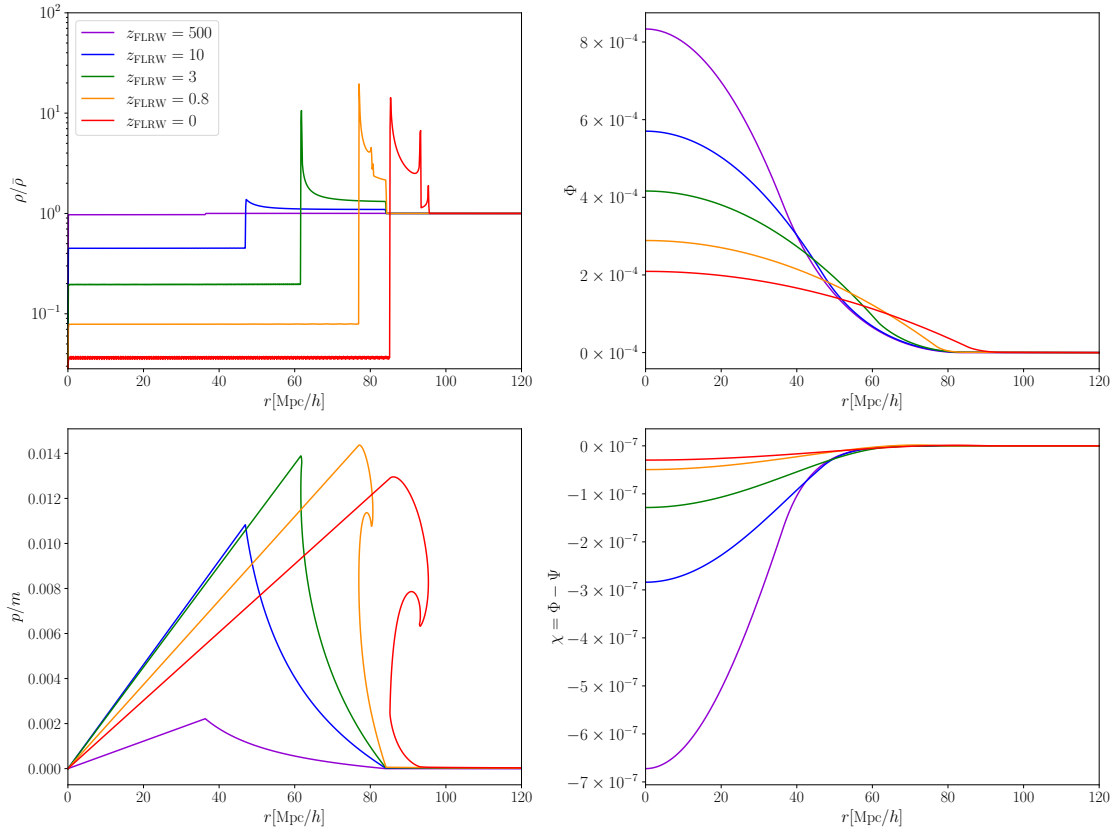

Figure 3.3: The same set of plots as for figure 3.2, this time for an evolving underdensity. The last two outputs exhibit a shell-crossing, which can be seen in the density and momentum portraits. This non-linear feature can only be modelled with an N-body simulation. The parameters used here were: size of the box: 120 Mpc/h, $r_1 = 36$ Mpc/h, $r_2 = 84$ Mpc/h, $\delta = -1/40$, $z_{in} = 500$.

observed redshift, which is defined as:

$$1 + z_{\mathrm{obs}} = \frac{(g_{\mu\nu} k^\mu u^\nu)|_{\mathrm{src}}}{(g_{\mu\nu} k^\mu u^\nu)|_{\mathrm{obs}}}\,, \tag{3.16}$$

where the product of the photon's 4-momentum k^μ and the 4-velocity of the source (observer) u^μ can be related to the momentum p of the source (observer) particle in the limit of weak fields as:

$$g_{\mu\nu} k^\mu u^\nu = -k^0 a\,(1+\Psi)\,\frac{1}{m}\left[\sqrt{m^2 + p^2} - p\right]. \tag{3.17}$$

To propagate a photon through the simulation, we use the null condition ($ds^2 = 0$). We can actually find a fixed relation between $dr/d\tau$ and $d\varphi/d\tau$, a consequence of the fact that a photon always travels at the speed of light:

$$1 + 2\Psi + 2\Phi = \left(\frac{\mathrm{d}r}{\mathrm{d}\tau}\right)^2 + \left(\frac{\mathrm{d}\varphi}{\mathrm{d}\tau}\right)^2 r^2 \tag{3.18}$$

which gives:

$$\frac{\mathrm{d}r}{\mathrm{d}\tau} = \pm\,(1 + \Psi + \Phi) \qquad \Leftrightarrow \qquad \frac{\mathrm{d}\varphi}{\mathrm{d}\tau} = 0. \tag{3.19}$$

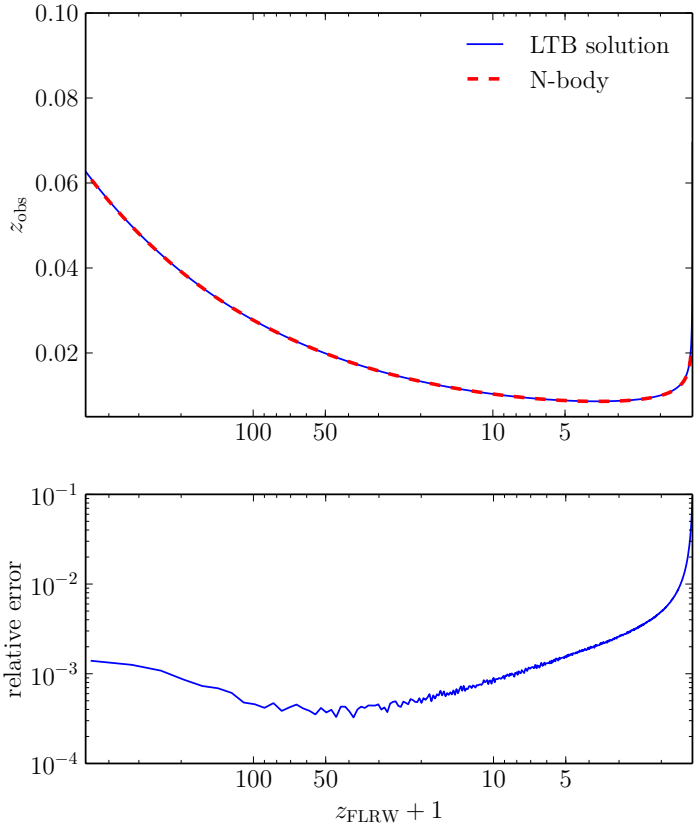

Figure 3.4: Top: the redshift of light, emitted by an in-falling source particle, as a function of the background redshift $z_{\rm FLRW}$ at the time when the light is detected by the observer. Initially, the observed redshift is decreasing, which is something we would expect for two particles comoving with the background in a matter dominated universe. Later, as the collapsing structure evolves, the velocity of the in-falling source becomes the dominant contribution and the redshift starts increasing again. Bottom: relative error between our relativistic simulation and the LTB solution. The error is mainly due to the first-order matching of the initial conditions. The error increases as the collapse evolves. This is because the collapse time itself receives a first-order correction. Therefore, the divergence in observed redshift happens at slightly offset times, resulting in the error blowing up. For this plot, the same parameters as the ones in Figure 3.2 were used.

On every step, the photon's energy can be evaluated by integrating the time component of the geodesic equation:

$$\frac{\mathrm{d}k^0}{\mathrm{d}\tau} + \left[\Psi_{,\tau} - \Phi_{,\tau} + 2\Psi_{,r}\frac{\mathrm{d}r}{\mathrm{d}\tau} + 2\mathcal{H}\right] k^0 = 0 \tag{3.20}$$

The results for this observable are shown in figure 3.4. As can be seen, the simulation agrees well with the LTB predictions. In fact, for this plot the leading source of deviation actually comes from imprecise matching of initial conditions, which could only be improved by performing that matching at a higher order of perturbation theory.

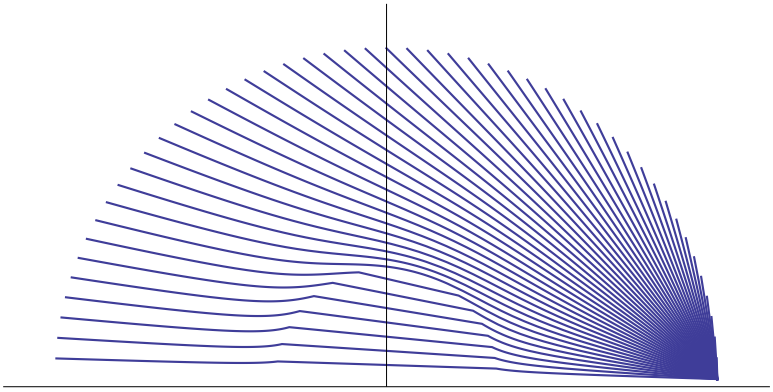

Figure 3.5: Schematic representation of the trajectories of lensed photons in an LTB geometry. The rays enter the LTB region at varying angles on the right end of the plot. Along their way through the simulation volume their trajectories are deflected due to the underlying overdensity.

Lensing of non-radial rays

Another observable we can analyse is the deflection of a ray that propagates not only in the radial, but also in an angular direction. The trajectory of such a ray is lensed by the gravitational potentials. Spherical symmetry ensures that the trajectory of a light ray will be planar, so we only have to consider the radial direction and one angular direction. By setting $\vartheta = \pi/2$ or $k^\vartheta = 0$, one can derive the two equations that determine that path of the photon from the geodesic equation:

$$\frac{\mathrm{d}^2 r}{\mathrm{d}\tau^2} - 2\left(\Psi_{,r} + \Phi_{,r}\right)\left(\frac{\mathrm{d}r}{\mathrm{d}\tau}\right)^2 - \left(\Psi_{,\tau} + \Phi_{,\tau}\right)\frac{\mathrm{d}r}{\mathrm{d}\tau} - \left(\frac{\mathrm{d}\varphi}{\mathrm{d}\tau}\right)^2 r + \left(\Phi_{,r} + \Psi_{,r}\right) = 0 \tag{3.21a}$$

$$\frac{\mathrm{d}^2 \varphi}{\mathrm{d}\tau^2} + \left(\Phi_{,\tau} - \Psi_{,\tau} - 2\Phi_{,\tau}\right)\frac{\mathrm{d}\varphi}{\mathrm{d}\tau} + \left(\frac{2}{r} - 2\Psi_{,r} - 2\Phi_{,r}\right)\frac{\mathrm{d}r}{\mathrm{d}\tau}\frac{\mathrm{d}\varphi}{\mathrm{d}\tau} = 0 \tag{3.21b}$$

Varying the initial angle at which photons enter the perturbed region and observing the deflection angle (the angle by which its outgoing trajectory differs from the incoming one), we get a gauge independent probe of the underlying potentials.

In Figure 3.5 we show the trajectories of photons that propagate through the simulation volume. We tracked 200 photons, entering at different angles α. The photons that experience the most lensing are those that pass near the edge of the overdensity. A photon that enters at $\alpha = 0$ and passes through the centre of the overdensity is not lensed, since its path is radial. Likewise, a photon that enters at $\alpha = \pi/2$ spends too little time inside the non homogeneous region to change its path substantially. In Figure 3.6 we show the deflection angle as a function of α.

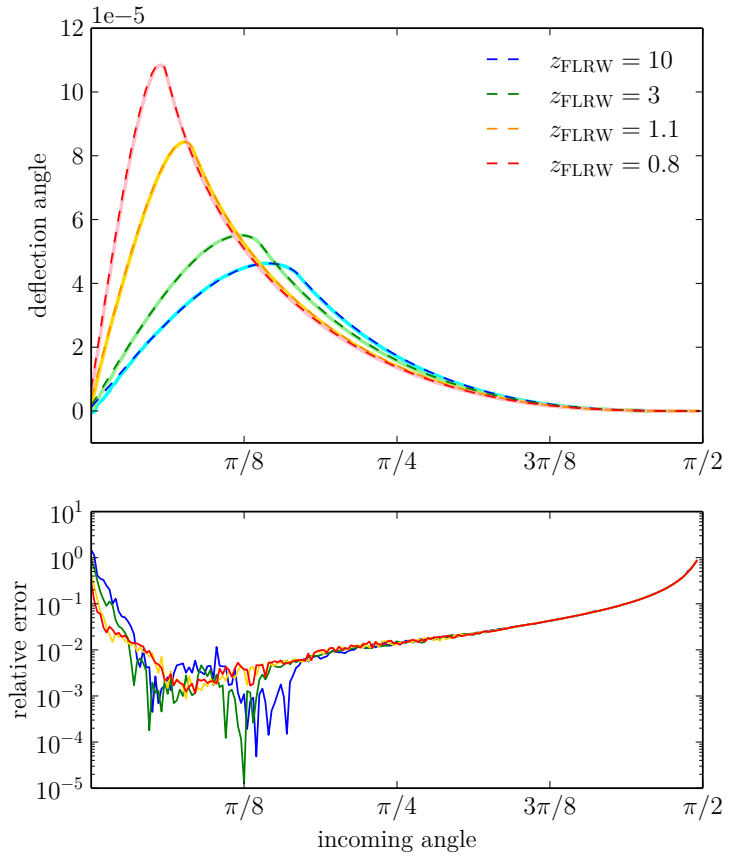

Figure 3.6: Lensing of photons by an underlying overdensity. We plot the LTB predictions (solid lines) and the results from our simulation (dashed lines on top of them) at four selected redshifts. The parameters used here are the same as the ones in Figure 3.2.

3.3 Angular Momentum

Using the formalism presented so far, any initial over-density would collapse to a singularity within a finite amount of time. For realistic cosmological structures this does not happen due to the process of virialisation during which the initial potential energy of a large scale density fluctuation is partially converted into radial and angular kinetic energies of individual particles. Most importantly, the angular momentum thus generated in individual particles causes these particles to miss the centre of a collapsing structure. This then avoids the production of densities large enough to cause singularities to arise. Essentially, the produced angular momentum provides an effective pressure term that resists the collapse.

We show in this section how we can model this pressure by adding angular momentum to the particles in our simulation box, without losing spherical symmetry as conceived in (Einstein, 1939). The downside to the method we present is that there can be no exchange of angular momentum between particles. This is because adding such an effect would

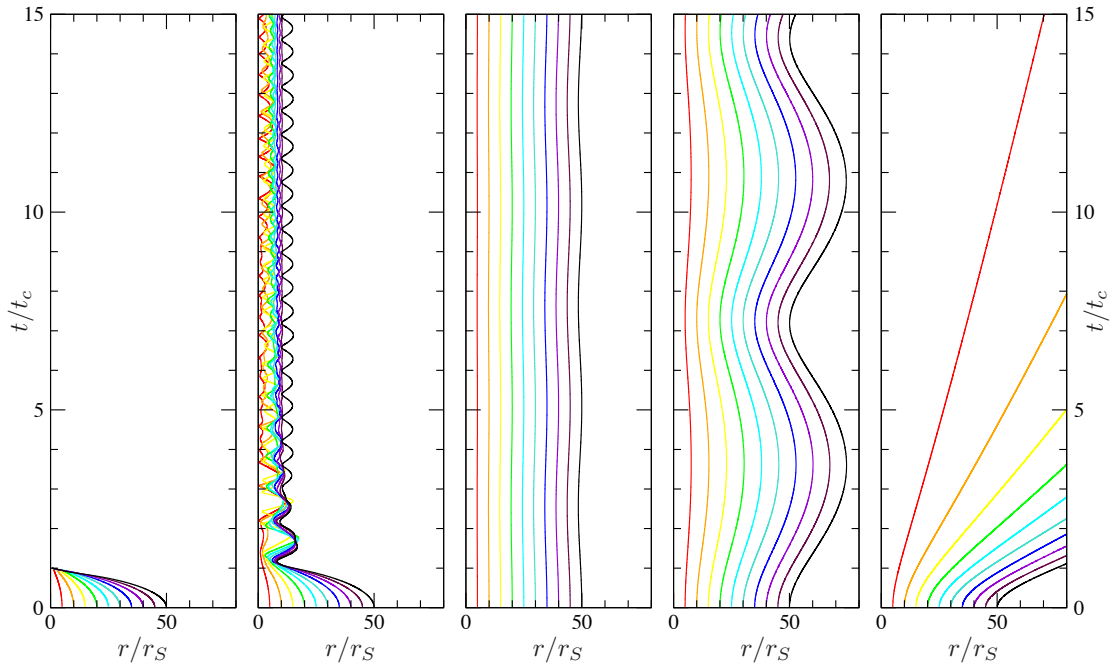

Figure 3.7: Space-time diagrams showing the radial trajectories of shells initially arranged as a uniform ball with zero radial motion. Different colors label different shells, black labelling the outermost one. From left to right, the angular momentum of the shell particles was set to $L = 0$ where we get collapse; $L = 0.5L_{\rm K}$ where a violent re-configuration to a new, much more compact state happens; $L = L_{\rm K}$ at which point the behaviour is almost Keplerian, with tiny perturbations caused by relativistic corrections - stability is guaranteed for a very long time scale; $L = 1.1L_{\rm K}$ with quasi-stable oscillations with relatively long timescale for chaotic behavior; and $L = 1.4L_{\rm K}$ which corresponds to an unbound state. Here, $L_{\rm K}$ is the (r-dependent) value of L which corresponds to a circular Keplerian orbit in Newtonian theory. The radius is plotted in units of r_S, the Schwarzschild radius of the ball; initially the ball has a radius of $50r_S$. The time coordinate is plotted in units of t_c, the collapse time of the irrotational ball.

necessarily require some degree of deviation from spherical symmetry. Unfortunately, this limits how far we can model the true virialisation process; nevertheless, as we show, we can still set initial conditions that produce stable, bound, spherical structures.

We can now imagine the shells to be made up of infinitesimal point-like particles, evenly distributed over the sphere. Apart from the radial momentum, which is the same for all infinitesimal point-like particles on a given sphere, we can assign each of those particles an angular momentum in a particular direction, in such a manner that once we perform the average over the momenta of all infinitesimal particles on a given sphere, there is no preferred direction of angular momentum. One can imagine that for every infinitesimal particle with some angular momentum, there is another particle on a trajectory in the same plane, but traveling in the opposite direction. Although we can not observe any non-radial motion of spherical shells, their radial motion is nevertheless affected. This is because the equation that governs the propagation of particles in the radial direction involves a pressure-like term that depends on the angular momentum of the particle.

We start again with the geodesic equation

$$\frac{\mathrm{d}^2 x^\mu_{(n)}}{\mathrm{d}s^2} + \Gamma^\mu_{\nu\rho} \frac{\mathrm{d}x^\nu_{(n)}}{\mathrm{d}s} \frac{\mathrm{d}x^\rho_{(n)}}{\mathrm{d}s} = 0 \tag{3.22}$$

Calculating all the Christoffel symbols $\Gamma^\mu_{\rho\sigma}$ we have three equations for evolution of coordinates:

$$\frac{\mathrm{d}^2\tau}{\mathrm{d}s^2} = -\left(\mathcal{H} + \Psi_{,\tau}\right)\left(\frac{\mathrm{d}\tau}{\mathrm{d}s}\right)^2 - 2\Psi_{,r}\frac{\mathrm{d}\tau}{\mathrm{d}s}\frac{\mathrm{d}r}{\mathrm{d}s} - \left(\mathcal{H}(1-2\Phi-2\Psi) - \Phi_{,\tau}\right)\left(\left(\frac{\mathrm{d}r}{\mathrm{d}s}\right)^2 + r^2\left(\frac{\mathrm{d}\varphi}{\mathrm{d}s}\right)^2\right) \tag{3.23a}$$

$$\begin{aligned}\frac{\mathrm{d}^2 r}{\mathrm{d}s^2} = &-\Psi_{,r}\left(\frac{\mathrm{d}\tau}{\mathrm{d}s}\right)^2 - 2\left(\mathcal{H} - \Phi_{,\tau}\right)\frac{\mathrm{d}\tau}{\mathrm{d}s}\frac{\mathrm{d}r}{\mathrm{d}s} \\ &+ \Phi_{,r}\left(\frac{\mathrm{d}r}{\mathrm{d}s}\right)^2 + r\left(1 - r\Phi_{,r}\right)\left(\frac{\mathrm{d}\varphi}{\mathrm{d}s}\right)^2\end{aligned} \tag{3.23b}$$

$$\frac{\mathrm{d}^2\varphi}{\mathrm{d}s^2} = -2\left(\mathcal{H} - \Phi_{,\tau}\right)\frac{\mathrm{d}\tau}{\mathrm{d}s}\frac{\mathrm{d}\varphi}{\mathrm{d}s} - 2\left(\frac{1}{r} - \Phi_{,r}\right)\frac{\mathrm{d}r}{\mathrm{d}s}\frac{\mathrm{d}\varphi}{\mathrm{d}s} \tag{3.23c}$$

Here we only kept one angular coordinate. Since the potentials are spherically symmetric, each infinitesimal point-like particle will move in a two-dimensional plane and so the reference frame can always be rotated so that the direction of the angular momentum is perpendicular to this plane. We see that the last equation (3.23c) can be integrated analytically with respect to $\mathrm{d}s$ once, to give

$$\frac{\mathrm{d}\varphi}{\mathrm{d}s} = \frac{L}{(ar)^2}(1 + 2\Phi) \tag{3.24}$$

where L is the constant of integration. We can express the evolution of coordinates r and φ with respect to coordinate time $\mathrm{d}\tau$ instead of eigentime $\mathrm{d}s$ using a simple trick:

$$\frac{\mathrm{d}^2 r}{\mathrm{d}\tau^2} = \left(\frac{\mathrm{d}^2 r}{\mathrm{d}s^2} - \frac{\mathrm{d}^2\tau}{\mathrm{d}s^2}\frac{\mathrm{d}r}{\mathrm{d}\tau}\right)\left(\frac{\mathrm{d}\tau}{\mathrm{d}s}\right)^{-2} \tag{3.25}$$

And equivalently for φ. With this we can combine equations (3.23b) and (3.23c) with (3.23a) to express:

$$\begin{aligned}\frac{\mathrm{d}^2 r}{\mathrm{d}\tau^2} = &\left(-\mathcal{H} + 2\Phi_{,\tau} + \Psi_{,\tau}\right)\frac{\mathrm{d}r}{\mathrm{d}\tau} - \Psi_{,r} + \left(\Phi_{,r} + 2\Psi_{,r}\right)\left(\frac{\mathrm{d}r}{\mathrm{d}\tau}\right)^2 + \left(r - r^2\Phi_{,r}\right)\left(\frac{\mathrm{d}\varphi}{\mathrm{d}\tau}\right)^2 \\ &+ \left(\mathcal{H}(1-2\Phi-2\Psi) - \Phi_{,\tau}\right)\left(\left(\frac{\mathrm{d}r}{\mathrm{d}\tau}\right)^2 + r^2\left(\frac{\mathrm{d}\varphi}{\mathrm{d}\tau}\right)^2\right)\frac{\mathrm{d}r}{\mathrm{d}\tau}\end{aligned} \tag{3.26a}$$

$$\begin{aligned}\frac{\mathrm{d}^2\varphi}{\mathrm{d}\tau^2} =& (-\mathcal{H} + 2\Phi_{,\tau} + \Psi_{,\tau})\frac{\mathrm{d}\varphi}{\mathrm{d}\tau} + \left(-\frac{2}{r} + 2\Phi_{,r} + 2\Psi_{,r}\right)\frac{\mathrm{d}r}{\mathrm{d}\tau}\frac{\mathrm{d}\varphi}{\mathrm{d}\tau} \\ &+ (\mathcal{H}(1 - 2\Phi - 2\Psi) - \Phi_{,\tau})\left(\left(\frac{\mathrm{d}r}{\mathrm{d}\tau}\right)^2 + r^2\left(\frac{\mathrm{d}\varphi}{\mathrm{d}\tau}\right)^2\right)\frac{\mathrm{d}\varphi}{\mathrm{d}\tau}\end{aligned} \tag{3.26b}$$

In addition we have the "mass-shell condition" for particles with mass:

$$g_{\mu\nu}\frac{\mathrm{d}x^\mu}{\mathrm{d}s}\frac{\mathrm{d}x^\nu}{\mathrm{d}s} = -1 \tag{3.27}$$

which is expressed, using our metric, as:[5]

$$-a^2\left(\frac{\mathrm{d}\tau}{\mathrm{d}s}\right)^2(1 + 2\Psi) + a^2\left(\frac{\mathrm{d}r}{\mathrm{d}s}\right)^2(1 - 2\Phi) + a^2r^2\left(\frac{\mathrm{d}\varphi}{\mathrm{d}s}\right)^2(1 - 2\Phi) = -1 \tag{3.28}$$

The momentum of the particles now has a radial component,

$$p_r = \frac{m(1 - \Phi)\frac{\mathrm{d}r}{\mathrm{d}\tau}}{\sqrt{1 + 2\Psi - (1 - 2\Phi)\left(\frac{\mathrm{d}r}{\mathrm{d}\tau}\right)^2 - (1 - 2\Phi)r^2\left(\frac{\mathrm{d}\varphi}{\mathrm{d}\tau}\right)^2}} \tag{3.29}$$

and an angular one,

$$p_\varphi = \frac{m(1 - \Phi)r\frac{\mathrm{d}\varphi}{\mathrm{d}\tau}}{\sqrt{1 + 2\Psi - (1 - 2\Phi)\left(\frac{\mathrm{d}r}{\mathrm{d}\tau}\right)^2 - (1 - 2\Phi)r^2\left(\frac{\mathrm{d}\varphi}{\mathrm{d}\tau}\right)^2}} \tag{3.30}$$

Using the mass-shell condition (3.28), the definition of the conserved quantity L (3.24), and (3.23a), we can extract the angular velocity of infinitesimal particles,

$$\frac{\mathrm{d}\varphi}{\mathrm{d}\tau} = \frac{L}{ar^2}\sqrt{\frac{1 + 4\Phi + 2\Psi - (1 + 2\Phi)\left(\frac{\mathrm{d}r}{\mathrm{d}\tau}\right)^2}{1 + \frac{L^2(1+2\Phi)}{a^2r^2}}}, \tag{3.31}$$

and eliminate it from the momenta equations:

$$p_r = m\frac{\mathrm{d}r}{\mathrm{d}\tau}\frac{(1 - \Phi)}{ar}\sqrt{\frac{a^2r^2 + L^2(1 + 2\Phi)}{1 + 2\Psi - (1 - 2\Phi)\left(\frac{\mathrm{d}r}{\mathrm{d}\tau}\right)^2}} \tag{3.32}$$

and

$$p_\varphi = \frac{mL(1 + \Phi)}{ar}. \tag{3.33}$$

Note that it is L which is the conserved quantity, not p_φ, within our framework. With this setup, we can finally express the equation for evolution of shell particles (3.23b) as a

[5] Again, we have set $\vartheta = \pi/2$, so $\mathrm{d}\vartheta/\mathrm{d}s = 0$.

system of two first-order equations:

$$\frac{\mathrm{d}p_r}{\mathrm{d}\tau} = (\Phi_{,\tau} - \mathcal{H})p_r - \sqrt{m^2 + p_r^2 + p_\varphi^2}\Psi_{,r} + \left(\frac{1}{r} - \Phi_{,r}\right)\frac{p_\varphi^2(1+\Phi+\Psi)}{\sqrt{m^2 + p_r^2 + p_\varphi^2}} \tag{3.34}$$

and

$$\frac{\mathrm{d}r}{\mathrm{d}\tau} = \frac{p_r}{\sqrt{m^2 + p_r^2 + p_\varphi^2}}(1+\Phi+\Psi). \tag{3.35}$$

These two equations describe the movement of shell particles and need to be solved numerically. A sanity check verifies that if we set p_φ to zero, we recover the momentum evolution equation in the case without angular momentum, (3.12).

With our new definitions of p_r and p_φ, the energy-momentum tensor expresses as:

$$T_0^0 = -\frac{1+3\Phi}{4\pi r^2 a^3}\sum_n \delta(r - r_{(n)})\left(\sqrt{m^2 + p_r^2 + p_\varphi^2}\right)_{(n)} \tag{3.36}$$

and

$$\Pi_{rr} = \frac{1+3\Phi}{4\pi r^2 a^3}\sum_n \delta(r - r_{(n)})\left(\frac{\frac{2}{3}p_r^2 - \frac{1}{3}p_\varphi^2}{\sqrt{m^2 + p_r^2 + p_\varphi^2}}\right)_{(n)} \tag{3.37}$$

The angular motion also gives rise to a transverse Doppler effect. This can be seen, e.g., from eq. (3.17) being modified as

$$g_{\mu\nu}k^\mu u^\nu = -k^0 a\,(1+\Psi)\,\frac{1}{m}\left[\sqrt{m^2 + p_r^2 + p_\varphi^2} - p_r\right]. \tag{3.38}$$

In figure 3.7 we have plotted the radial trajectories of shells within balls that have uniform density, but non-zero and non-uniform angular momentum. Each panel corresponds to the same initial density state, but different initial states of angular momentum. As can be seen, our code is able to describe balls that collapse to a point; balls that first begin to collapse under gravity but then stabilise; balls where the effective pressure due to angular momentum perfectly balances gravitational attraction; balls that first expand due to effective pressure, but then stabilise; and finally, balls which are blown apart by pressure. Only in the first and last situations respectively will our code certainly break down, and even then it will survive until the weak field limit breaks down, or a particle leaves the box. In these plots, the balls begin only 50 times larger than their Schwarzschild radii, therefore relativistic effects will not be negligible.

We have not considered the stability of the shells in our simulation. This is a non-trivial issue (Gleiser, Reinaldo J. and Ramirez, Marcos A., 2009, 2010). From the results in (Gleiser, Reinaldo J. and Ramirez, Marcos A., 2009, 2010) it is clear that the assumption

of stable, fixed mass shells is not always physically valid and that the shells would in fact disperse if examined in finer resolution. In fact, in the second panel of figure 3.7 we can see this effect occurring in our own analysis. For example, the red and orange lines begin close to each other in phase space and could even be considered as parts of the same shell in a lower resolution simulation of the same initial conditions. However at later times (e.g. at $t = 5t_c$) the two shells are moving in opposite directions. An interesting analysis that could be done within our framework is to analyse two simulations with different resolutions, but the same initial conditions. It would then be possible to follow the evolution of the sub-shells of one large shell to quantitatively determine the stability of the larger shell. Such an analysis, which is beyond the scope of our present work, would hopefully reproduce, in the simulation, the results of (Gleiser, Reinaldo J. and Ramirez, Marcos A., 2009, 2010). If our method were to be applied to real physical structures, such an issue would need to be examined and quantified.

3.4 Conclusion

We have presented an N-body framework for spherically symmetric solutions valid in the weak-field regime of general relativity. We have primarily applied this framework in a cosmological context, expanding around an FLRW metric; however nothing forbids the application of the framework to other contexts. Spherical symmetry was imposed in order to obtain an economic setup for numerical studies. We compared our code against two types of known exact solutions, Schwarzschild and Lemaître-Tolman-Bondi, and found good agreement. However, our scheme is suitable also for setups where no exact solution is known, for instance when the fluid description of matter is not valid.

Furthermore, we demonstrated that the relativistic potentials are computed more accurately than in a Newtonian scheme. This feature will be useful for the study of models which have exotic sources of stress-energy perturbations, such as dynamical dark energy or modified gravity. On a related note, we stress that our scheme does not make any assumptions about the nature of perturbations apart from the requirement that they give rise to weak gravitational fields only. This assumption breaks down, e.g., if a black hole is formed.

In order to avoid the collapse of an overdensity into a black hole, we have introduced a method to create a stable bound structure supported by angular momentum. Such configurations may, in some sense, be more realistic proxies for cosmic structures such

as galaxy clusters, and can therefore be useful laboratories for studying gravity at these scales. They may also be useful for the study of weakly relativistic, compact bound objects that can form in the early universe, such as ultra compact mini-haloes, or for the early stages of the formation of primordial black holes.

3.5 Acknowledgments

We thank Peter Coles, Ruth Durrer, and Martin Kunz for useful suggestions, insights and comments. This work was supported by the Swiss Society for Astrophysics and Astronomy through a Funding and Travel Award, sponsored by the Foundation MERAC (Mobilising European Research in Astrophysics and Cosmology). SH acknowledges support from the Science and Technology Facilities Council [grant number ST/L000652/1]. JA acknowledges support from the Swiss National Science Foundation.

3.A Appendix1: Linear Relation between LTB Solution and Longitudinal Gauge

In this appendix we give the linear coordinate transformations which we use to set up initial conditions corresponding to a given LTB solution. These relations are valid to the extent that the matching is done at a time when linear perturbation theory can be applied. LTB solutions which do not allow a perturbative description at any time are more difficult to translate into our gauge, and there may be cases where it is impossible. We will not consider solutions of this type in this paper.

Our starting point is the LTB line element given in eq. (3.15). At the initial time $t_{\rm in}$ where we will do the matching, we will rescale the coordinate r such that, at that time, $R(t_{\rm in}, r) = a(t_{\rm in})r$. The (time independent) gravitational mass function can then simply be obtained as

$$\begin{aligned} 2M(r) &= 8\pi G a^3(t_{\rm in}) \int_0^r \tilde{r}^2 \rho(t_{\rm in}, \tilde{r}) \mathrm{d}\tilde{r} \\ &= 3H^2 a^3 \int_0^r \tilde{r}^2 \left(1 + \delta(t_{\rm in}, \tilde{r})\right) \mathrm{d}\tilde{r} \,. \end{aligned} \tag{3.39}$$

In this work we are interested in setups where the metric is FLRW everywhere except for a finite spherical region. This can be achieved by choosing a "compensated" density

profile such that the mass function becomes the one of FLRW, $M(r) = H^2 a^3 r^3/2$, at the boundary of the region[6]. We will choose a particularly simple profile, given by

$$\delta(t_{\rm in}, r) = \begin{cases} \delta_1 & r < r_1 \\ \delta_2 & r_1 < r < r_2 \\ 0 & r > r_2 \end{cases} , \tag{3.40}$$

where $\delta_2 = -\delta_1 r_1^3 / \left(r_2^3 - r_1^3\right)$ gives the correct matching to FLRW as can be seen by inspecting the resulting mass function.

Next we will use the parametric expression for the exact LTB solution in order to determine the metric function $E(r)$. Let us consider $E(r) < 0$, the opposite case is analogous. The parametric expressions are

$$R(t,r) = -\frac{M(r)}{2E(r)} \left(1 - \cos\eta\right) , \tag{3.41a}$$

$$\left(\eta - \sin\eta\right)^{2/3} = -\frac{2E(r)}{M^{2/3}(r)} t^{2/3} . \tag{3.41b}$$

While the parameter η cannot be eliminated in closed form, it is possible to do so perturbatively for small η, i.e. at early time. We find that

$$E(r) = -\frac{5}{6} r^2 H^2(t_{\rm in}) a^2(t_{\rm in}) f(r) , \tag{3.42}$$

where

$$f(r) = \begin{cases} \delta_1 & \text{if } r < r_1 \\ \delta_2 + \frac{r_1^3}{r^3} \left(\delta_1 - \delta_2\right) & \text{if } r_1 < r < r_2 \\ 0 & \text{if } r > r_2 \end{cases} . \tag{3.43}$$

In the linear regime we also have

$$R(t,r) = a(t) r \left[1 + \frac{1}{3} f(r) \left(1 - \frac{a(t)}{a(t_{\rm in})}\right)\right] . \tag{3.44}$$

Let us now write the line element in a convenient perturbative notation,

$$R^2(t,r) = a^2(t) r^2 \left[1 + 2b(t,r)\right] , \tag{3.45a}$$

$$\frac{\left[R_{,r}(t,r)\right]^2}{1 + 2E(r)} = a^2(t) \left[1 + 2y(t,r)\right] , \tag{3.45b}$$

[6] Note that $H^2 a^3$ is independent of time in a matter dominated universe.

which implies

$$b(t,r) = \frac{1}{3}f(r)\left(1-\frac{a(t)}{a(t_{\rm in})}\right), \tag{3.46a}$$
$$y(t,r) = b(t,r)+rb_{,r}(t,r)-E(r). \tag{3.46b}$$

We can now work out the linear coordinate transformation from synchronous to longitudinal gauge (see also (Adamek et al., 2014a)). A straightforward calculation shows

$$r\frac{\partial}{\partial r}\left[\frac{1}{r}\Phi_{,r}(t,r)\right] = -b_{,rr}(t,r)+H(t)a^2(t)\left[y_{,t}(t,r)-b_{,t}(t,r)\right] - \frac{2}{r^2}\left[y(t,r)-b(t,r)\right]+\frac{1}{r}y_{,r}(t,r), \tag{3.47a}$$
$$r\frac{\partial}{\partial r}\left[\frac{1}{r}\Psi_{,r}(t,r)\right] = 2H(t)a^2(t)\left[b_{,t}(t,r)-y_{,t}(t,r)\right]+a^2(t)\left[b_{,tt}(t,r)-y_{,tt}(t,r)\right] \tag{3.47b}$$

Since the combination H^2a^3 is independent of time in a matter dominated universe we can evaluate it at $t=t_{\rm in}$ and find

$$r\frac{\partial}{\partial r}\left[\frac{1}{r}\Phi_{,r}(t,r)\right] = r\frac{\partial}{\partial r}\left[\frac{1}{r}\Psi_{,r}(t,r)\right] = \frac{1}{2}H^2(t_{\rm in})a^2(t_{\rm in})rf'(r), \tag{3.48}$$

which can be integrated twice to obtain Φ and Ψ. The constants of integration should be chosen such that we can match smoothly to FLRW at $r=r_2$. In other words, we require $\Phi|_{r=r_2}=\Psi|_{r=r_2}=\Phi_{,r}|_{r=r_2}=\Psi_{,r}|_{r=r_2}=0$. The corresponding solutions are

$$\Phi(t,r)=\Psi(t,r)=\frac{1}{2}H^2(t_{\rm in})a^2(t_{\rm in})\int_{r_2}^{r}\tilde{r}f(\tilde{r})\mathrm{d}\tilde{r}. \tag{3.49}$$

3.B Appendix2: Initial Particle Data

Given a linear solution for Φ, Ψ which specifies the initial conditions, we can work out the initial particle configuration. To this end, we linearize eq. (3.2),

$$\Phi_{,rr}+\frac{2}{r}\Phi_{,r}-3\mathcal{H}^2\Phi=-4\pi Ga^2\delta T^0_0, \tag{3.50}$$

where we have used that $\Phi_{,t}=\chi=0$ at linear order.

The aim of this section is to construct a linear displacement field $\delta r(r)$ which specifies the initial particle positions $r_{(n)}(t_{\rm in})=r^0_{(n)}+\delta r(r^0_{(n)})$ as infinitesimal displacements from

a homogeneous distribution $r^0_{(n)}$. Expanding eq. (3.8) to linear order we find

$$\delta T^0_0 = \bar{T}^0_0 \left(3\Phi - \delta r_{,r} - \frac{2}{r}\delta r\right) . \tag{3.51}$$

To see this, take the continuum limit of the particle sum,

$$T^0_0 = -\frac{1+3\Phi}{4\pi r^2 a^3}\sum_n m_{(n)}\delta(r - r_{(n)}) \to -\frac{1+3\Phi}{4\pi r^2 a^3}\int \bar{f}(r^0_{(n)})\delta(r - r_{(n)})\mathrm{d}r^0_{(n)} , \tag{3.52}$$

with a distribution function $\bar{f}(r^0_{(n)}) \propto (r^0_{(n)})^2$ corresponding to the homogeneous distribution. Next, change the integration variable to $r_{(n)}$ to obtain eq. (3.51). Inserting into eq. (3.50) and using eq. (3.3), the solution for the displacement is found to be

$$\delta r = \frac{5}{r^2}\int_0^r \tilde{r}^2\Phi(t_{\rm in}, \tilde{r})\mathrm{d}\tilde{r} - \frac{2}{3\mathcal{H}^2}\Phi_{,r} . \tag{3.53}$$

Here the constant of integration is fixed by requiring regularity at the origin, which implies $\delta r|_{r=0} = 0$.

The initial particle velocities can be obtained simply by taking the time derivative of above equation,

$$\left.\frac{\mathrm{d}r}{\mathrm{d}\tau}\right|_{t_{\rm in}} = \delta r_{,\tau} = -\frac{2}{3\mathcal{H}}\Phi_{,r} , \tag{3.54}$$

where we used $\mathcal{H}' = -\mathcal{H}^2/2$ in a matter dominated universe.

3.C Appendix3: Particle-Mesh Scheme for Spherical Coordinates

Standard particle-mesh schemes (Hockney and Eastwood, 1999) usually employ a Cartesian mesh which means that a few modifications are required in order to make them fit for our purpose. Our mesh will have a uniform resolution in r, the radial coordinate, meaning that the volume of the cells increases as one moves outwards from the center. The mass resolution can be set independently by changing the number of particles per cell – a number which can also depend on radius and should be chosen according to the problem at hand.

The stress-energy tensor on the grid is computed by means of a particle-to-mesh projection. It is constructed by smearing out each particle over a finite radial interval and then determining the fraction of its mass within each cell. Explicitly, we replace

$$\frac{\delta(r - r_{(n)})}{4\pi r^2} \underset{r=r_i}{\to} \frac{w(r_i - r_{(n)})}{V_i} , \tag{3.55}$$

where r_i denotes the center of the ith cell, V_i is the cell's volume, $r_{(n)}$ is the position of the nth particle, and w is a weight function which depends on the smearing. We use triangular-shaped particles where

$$w(r_i - r_{(n)}) = \int \sqcap(r - r_i) \wedge (r - r_{(n)}) \mathrm{d}r \,, \tag{3.56}$$

with

$$\sqcap(\Delta r) = \begin{cases} 1 & \text{if } -\frac{\mathrm{d}r}{2} < \Delta r < \frac{\mathrm{d}r}{2} \\ 0 & \text{otherwise} \end{cases} , \tag{3.57}$$

and

$$\wedge(\Delta r) = \begin{cases} 1 + \frac{\Delta r}{\mathrm{d}r} & \text{if } -\mathrm{d}r < \Delta r < 0 \\ 1 - \frac{\Delta r}{\mathrm{d}r} & \text{if } 0 < \Delta r < \mathrm{d}r \\ 0 & \text{otherwise} \end{cases} . \tag{3.58}$$

Here and in the following, $\mathrm{d}r$ denotes the grid unit. Pictorially, $\sqcap$ characterizes the footprint of the cell (an interval of width $\mathrm{d}r$ centered at $r = r_i$), whereas $\wedge$ characterizes the shape of the particles (its mass distribution along the radial coordinate).

Our grid cells are centered at $r_i = i\mathrm{d}r$, with $i = 0, 1, \ldots$. The volume of the ith cell is computed as

$$V_i = \frac{4\pi}{3}\left(r_i + \frac{\mathrm{d}r}{2}\right)^3 - \frac{4\pi}{3}\left(r_i - \frac{\mathrm{d}r}{2}\right)^3 = 4\pi\left(i^2 + \frac{1}{12}\right)\mathrm{d}r^3 \tag{3.59}$$

for $i > 0$, and

$$V_0 = \frac{4\pi}{3}\left(\frac{\mathrm{d}r}{2}\right)^3 = \frac{4\pi}{24}\mathrm{d}r^3 \tag{3.60}$$

for the cell at the origin. Contributions which would be projected at negative radius are simply folded back onto the positive axis.

Next, we want to construct a particle distribution which would correspond to a homogeneous universe. A perturbed distribution can then be obtained by acting with an infinitesimal displacement as explained in appendix 3.B. Our homogeneous distribution will be constructed in a way as to minimize discretization issues. For simplicity, let us discuss a setup where we have one particle per grid cell (mass resolution can be increased by subdividing particles). If we choose initial particle positions as $r_{(n)} = (n + \frac{1}{2})\mathrm{d}r$, with $n = 0, 1, \ldots$, one can recursively construct the mass assignment for each particle which

would lead to an exactly uniform projected density under the above projection method:

$$m_{(n)} = 4\pi \left(\frac{1}{12} + n + n^2\right) \mathrm{d}r^3 a^3 \bar{\rho} \tag{3.61}$$

Here, $\bar{\rho} = -\bar{T}^0_0$ is the homogeneous density of the background FLRW model. Evidently, at very large radius $r_{(n)} \gg \mathrm{d}r$ this expression asymptotes to the correct continuum limit $m_{(n)} = 4\pi r^2_{(n)} \mathrm{d}r a^3 \bar{\rho}$. The corrections which come in at small radii are chosen to compensate for discretization effects, such that the projected density remains exactly homogeneous,

$$\frac{1}{a^3} \sum_n \frac{w(r_i - r_{(n)})}{V_i} m_{(n)} = \bar{\rho} \qquad \forall i \,. \tag{3.62}$$

The weight function w can also be used in order to interpolate grid-based quantities (fields, gradients of fields etc.) to the positions of the particles. This is necessary for the integration of the geodesic equations. For instance, in order to interpolate Φ, we would define

$$\Phi(r_{(n)}) = \sum_i \Phi(r_i) w(r_i - r_{(n)}) \,. \tag{3.63}$$

Note that the sum is now taken over the grid points. Similarly, we can interpolate a gradient as

$$\Psi_{,r}(r_{(n)}) = \sum_i \frac{\Psi(r_{i+1}) - \Psi(r_i)}{\mathrm{d}r} w(r_i + \frac{1}{2}\mathrm{d}r - r_{(n)}) \,, \tag{3.64}$$

based on a standard one-sided two-point gradient which naturally sits at half-integer grid units.

3D simulations with boosted primordial power spectra and ultracompact minihalos

Mateja Gosenca, Christian Byrnes, Shaun Hotchkiss, Julian Adamek

Abstract

We perform three-dimensional simulations of structure formation in the early Universe, when boosting the primordial power spectrum on $\sim$ kpc scales. We demonstrate that our simulations are capable of producing power-law profiles close to the steep $\rho \propto r^{-9/4}$ halo profiles that are commonly assumed to be a good approximation to ultracompact minihalos (UCMHs). However, we show that for more realistic initial conditions in which halos are neither perfectly symmetric nor isolated, the steep power-law profile is disrupted and we find that the Navarro-Frenk-White profile is a better fit to most halos. In the presence of background fluctuations even extreme, nearly spherical initial conditions do not remain exceptional. Nonetheless, boosting the amplitude of initial fluctuations causes all structures to form earlier and thus at larger densities. With sufficiently large amplitude of fluctuations we find that values for the concentration of typical halos in our simulations can become very large. However, despite the signal coming from dark matter annihilation inside the cores of these halos being enhanced, it is still orders-of-magnitude smaller compared to the usually assumed UCMH profile. The upper bound on the primordial power spectrum from the non-observation of UCMHs should therefore be re-evaluated.

4.1 Introduction

The cosmic microwave background (CMB) has yielded precise constraints on the primordial power spectrum of density perturbations that gave rise to all of the gravitationally bound structures observed in the Universe today (Ade et al., 2015). These constraints are especially tight over about two orders of magnitude in scales, with the constraints on the largest scales being weakened by cosmic variance limits, which cannot be overcome.

Hence the search for new information about the primordial power spectrum must focus on the smaller scale perturbations where there is potentially enormously more information to gain. There are numerous challenges to measuring the power spectrum on scales $k \gtrsim 0.3\ h\mathrm{Mpc}^{-1}$, e.g. Silk damping of the CMB, radiation pressure during structure formation, and the nonlinear dynamics of matter in the late Universe.

A promising constraint comes from the non-detection of primordial black holes (PBHs), which puts upper limits on the primordial power spectrum over a vast range of scales spanning 20 orders of magnitude (Carr et al., 2010; Josan and Green, 2010a). However, the constraints are weak, around $\mathcal{P}^\zeta \lesssim 10^{-3} - 10^{-2}$, six orders of magnitude above the amplitude observed on CMB scales. While these upper limits do provide useful constraints on certain models of inflation (Kawasaki et al., 2016; Pattison et al., 2017), they are very weak because the critical threshold to collapse to a PBH is extremely large and only a curvature perturbation of order unity will do so (with an exception if there was an early matter-dominated era, during which time the critical collapse threshold is greatly reduced by the absence of pressure (Carr et al., 2017; Cole and Byrnes, 2017)).

If the initial perturbations had a higher amplitude than expected from extrapolating the CMB measurement then another possible signature would be ultracompact minihalos (UCMHs), which are dense dark matter halos with a very steep density profile and large central density. It has been claimed that the non-detection of annihilating dark matter signatures from such compact objects provides relatively stringent upper limits on the primordial power spectrum, around $\mathcal{P}^\zeta \lesssim 10^{-7} - 10^{-6}$ over the scales corresponding to k from $10\,\mathrm{Mpc}^{-1}$ to $10^7\,\mathrm{Mpc}^{-1}$ (Bringmann et al., 2012). Due to the exponential dependence of the number density of UCMHs and PBHs on the amplitude of the power spectrum, confirmation of the UCMH constraints would also completely rule out the existence of any PBHs forming on these scales (corresponding to a PBH mass greater than about a solar mass). This would rule out the observed supermassive black holes having a primordial origin (Kohri et al., 2014). The relation between PBH and UCMH formation has also been studied in Mack et al. (2007), Lacki and Beacom (2010), and Saito and Shirai (2011).

Assuming that weakly interacting massive particles (WIMPs) make up the majority of dark matter, the most stringent observational constraint on the existence of UCMHs comes from the expected annihilation signal from the cores of UCMHs, where the density is extremely large and hence the probability of WIMPs annihilating is massively boosted by their large number density. The constraints only weakly depend on the assumed cross section and mass of the WIMPs, but can be totally evaded if dark matter does not

annihilate. There are nonetheless other possible signatures of UCMHs, such as from the Shapiro time-delay of millisecond pulsars (although note that no actual constraints exist yet, but there are forecasts (Clark et al., 2016a,b)) or microlensing (Ricotti and Gould, 2009; Zackrisson et al., 2013; Li et al., 2012).

It is in any case interesting to ask how the dark matter substructure would change if the initial small scale perturbations were larger than expected. Other papers which constrain the power spectrum on small scales include: Zhang (2011); van den Aarssen et al. (2012); Chluba et al. (2012); Yang et al. (2013a,b); Shandera et al. (2013); Yang et al. (2013c); Berezinsky et al. (2013); Ben-Dayan and Kalaydzhyan (2014); Berezinsky et al. (2014); Yang (2014); Natarajan et al. (2015); Anthonisen et al. (2015); Aslanyan et al. (2016); Clark et al. (2017); Beck and Colafrancesco (2016); Emami and Smoot (2017); Choi and Takahashi (2017). In particular, we note that CMB spectral distortion constraints provide an upper bound on the primordial power spectrum on about the same scales as UCMHs, which are about an order of magnitude weaker than the currently claimed constraints but independent of the DM model (Chluba et al., 2012).

To date, the theoretical forecasts on UCMH formation have been made using an idealised analytical model of their formation. Josan and Green (Josan and Green, 2010b) assumed that any density contrast $\delta = \delta\rho/\bar{\rho}$ satisfying $\delta_c > 10^{-3}$ at horizon entry would form an UCMH (following Ricotti and Gould (2009)) with a steep power law profile $\rho \propto r^{-9/4}$. This is motivated by the analytical calculation of Bertschinger 1985 (Bertschinger, 1985), who calculated the profile of a spherically symmetric perturbation accreting from a homogeneous background. The analytical calculation of the requisite density threshold was refined by Bringmann et al. (Bringmann et al., 2012) who included the effects of radiation in their calculation, which is relevant because UCMHs are assumed to form shortly after matter-radiation equality. They found comparably tight constraints. We show that in practice no δ_c actually exists, because the formation and final profile of a small halo strongly depends on its environment in a way which cannot be captured even approximately by a single number, unlike the case for PBHs.

In this paper we revisit and dramatically revise the calculation of UCMH formation, and for the first time perform realistic 3D simulations of this complex process. The analytical calculations assumed that UCMHs are sufficiently rare high-density peaks that form in isolation, surrounded by an unperturbed background until redshift ~ 10. They also neglected the effects of angular momentum, thereby using spherical symmetry to reduce the problem to a 1D one. This gives rise to the steep $\rho \propto r^{-9/4}$ density profile,

with a correspondingly boosted dark matter annihilation signal. We verify these results with an N-body simulation of an isolated spherical overdensity, obtaining a UCMH-like density profile.

In practice however, all UCMHs will be formed with particles with non-zero initial peculiar velocities and they are not really isolated from nearby perturbations, even if the nearest perturbations have a smaller amplitude. We analytically estimate that even an exceptionally large amplitude perturbation will be relatively close (in comparison to the size of the object) to another perturbation with the same scale and at least half its amplitude, even in the case of non-Gaussian initial perturbations. Moreover, even if an overdense region appears spherical when smoothed on a particular scale, it will still have fluctuations on smaller scales. These fluctuations will themselves grow, making the initial sphericity unstable (Lithwick and Dalal, 2011).

We then perform N-body simulations using two classes of initial conditions: the first with a $1\,\mathrm{kpc}/h$ sized protohalo of large initial density surrounded by successively larger surrounding fluctuations, and the second starting with the standard featureless power law spectrum of the curvature perturbation but boosted around the kpc scale, with boost factors of 10, 100, 1000, and without the boost (corresponding to the standard ΛCDM cosmology).

We find no clear evidence that UCMHs are formed even in the case when we boost the initial power spectrum by a factor of 1000. Furthermore, a UCMH which formed when simulated in isolation becomes unexceptional compared to other halos in the simulation box when we add background perturbations with a typical amplitude 1/5 of that of the protohalo. This means that the analytical estimates of UCMH formation are a poor match to realistic initial conditions. Instead we find that the emergence of NFW profiles is more generic (Angulo et al., 2016; Ogiya and Hahn, 2017; Dalal et al., 2010). NFW profiles have a central core with a much gentler $\rho \propto 1/r$ slope, and a correspondingly much weaker WIMP-annihilation signal.

The NFW minihalos formed when the initial power spectrum is boosted are nonetheless of much greater density than would exist in the standard ΛCDM Universe. Because *every* structure that forms earlier forms at a greater density, these NFW minihalos are also much more abundant than proposed UCMHs, which would only have formed at the most extreme locations of the primordial density field. Therefore it remains interesting to study which observational signatures they may give rise to. We provide estimates of how sharply the existing constraints have to be weakened when taking our results into account

by calculating the WIMP annihilation signal from an NFW rather than the $r^{-9/4}$ profile.

This paper is structured as follows: In the next section we introduce the power-law density profile usually assumed for the UCMHs and the universal NFW profile, and explain the fitting procedure we used to find the parameters of these models. We also describe the initial conditions of large-amplitude fluctuations. In section 4.3 we discuss the simulation results from an initial spherical overdensity, whose evolution into an UCMH in a homogeneous background we disrupt by adding random perturbations around it, with successively larger amplitude. We then boost the power spectrum on the kpc scale in section 4.4 by up to a factor of one thousand, and we describe how this gives rise to many NFW-like halos with very large concentration parameters. In section 4.5 we briefly review the theory of WIMP annihilation in the dense center of halos and calculate the signal from the halos we simulated, before concluding in section 4.6. Technical details of how we performed the simulations and convergence testing are left to the appendices.

4.2 Halo profiles and properties

4.2.1 UCMH profiles

Ultracompact minihalos are dark matter halos, expected to form around matter-radiation equality, featuring a very steep power-law density profile (Ricotti and Gould, 2009)

$$\rho(r) \propto r^{-9/4} \,. \tag{4.1}$$

If a UCMH forms, its extreme compactness might allow it to retain its shape until the present time making it and the extreme density at its center potentially observable.

This $r^{-9/4}$ power-law profile is the late-time form for the density of an initial spherical overdensity accreting from a homogenous background (Bertschinger, 1985).[1] This is true irrespective of the density profile of the initial seed overdensity, so long as its size is finite, it is spherical, and it eventually starts accreting from a homogeneous background. Though note that even the smallest amount of asphericity in initial conditions is unstable and will result in a triaxial profile (Lithwick and Dalal, 2011). For fitting to the power-law profiles

[1] Note that this is only strictly true when the profile is sufficiently coarse-grained. The true profile will be made up of a series of separate caustics arising from shells that have passed through the center of the overdensity a different number of times. See Fig. 8 of Bertschinger (1985) for the shape of the full non-coarse-grained profile.

we use the ansatz:

$$\rho(r) = Cr^{-\alpha}. \tag{4.2}$$

If we know the mass within a certain radius then C can be calculated via:

$$M(r_{\rm max}) = \int_0^{r_{\rm max}} 4\pi r^2 dr \rho(r). \tag{4.3}$$

The choice of $r_{\rm max}$ is somewhat ambiguous, because halos do not have a clear "edge"; their density instead asymptotes to the average density of the Universe and, for $\alpha \leq 3$, the above integral diverges with $r_{\rm max}$. There are several possible choices for $r_{\rm max}$ in the literature, we use the virial radius $r_{\rm vir}$ as determined by the *ROCKSTAR* halo finder (Behroozi et al., 2013). It is defined as the radius of a sphere inside which the average density contrast is $18\pi^2 \simeq 178$ (Bryan and Norman, 1998). Correspondingly, the mass of a halo up to the virial radius $M_{\rm vir} = M(r_{\rm vir})$ is the virial mass.

For the above power-law profile, C can therefore be expressed in terms of the virial mass and virial radius as:

$$C = \frac{M_{\rm vir}}{4\pi}(3-\alpha) r_{\rm vir}^{(\alpha-3)}. \tag{4.4}$$

4.2.2 The Navarro-Frenk-White profile

Most of the halos in the Universe appear to exhibit a density profile close to the Navarro-Frenk-White (NFW) (Navarro et al., 1996, 1997) profile:

$$\rho(r) = \frac{\rho_0}{\frac{r}{r_s}\left(1+\frac{r}{r_s}\right)^2}, \tag{4.5}$$

characterised by two parameters: r_s, the "scale radius", and ρ_0. For small radii, $r \ll r_s$, the profile's radial dependence is $\rho(r) \propto 1/r$, and for large r, it is $\rho(r) \propto 1/r^3$. The scale radius r_s therefore determines the radius at which the profile changes from one power law to the other. The characteristic density ρ_0 corresponds to $\rho_0 = 4\rho(r_s)$. Integrating Eq. (4.3) for $\rho(r)$, we obtain the mass within radius $r_{\rm max}$:

$$M(r_{\rm max}) = 4\pi\rho_0 r_s^3 \left(\ln\left(\frac{r_s + r_{\rm max}}{r_s}\right) - \frac{r_{\rm max}}{r_s + r_{\rm max}}\right). \tag{4.6}$$

Defining the concentration parameter (Bullock et al., 2001) as:

$$c = \frac{r_{\rm vir}}{r_s} \,, \tag{4.7}$$

ρ_0 can be expressed as:

$$\rho_0 = \frac{M_{\rm vir}}{4\pi r_s^3 \left(\ln(1+c) - c/(1+c)\right)} \,. \tag{4.8}$$

4.2.3 Fitting the profiles

We can use the relation between $M_{\rm vir}$, $r_{\rm vir}$ and the two profiles' parameters (i.e. equations (4.4) and (4.8)) to eliminate one free parameter from each profile. In logarithmic space the NFW profile can be expressed as:

$$\begin{aligned} \log\left(\rho(r)\right) = &\log\left(\frac{M_{\rm vir}}{4\pi r_{\rm vir}^3}\right) + \log\left(\frac{c^2}{\ln(1+c) - c/(1+c)}\right) \\ &- \log\left(r/r_{\rm vir}\right) - 2\log\left(1 + cr/r_{\rm vir}\right) \end{aligned} \tag{4.9}$$

and the power-law as

$$\begin{aligned} \log\left(\rho(r)\right) = &\log\left(\frac{M_{\rm vir}}{4\pi r_{\rm vir}^3}\right) \\ &+ \log(3-\alpha) - \alpha \log\left(r/r_{\rm vir}\right) . \end{aligned} \tag{4.10}$$

For $M_{\rm vir}$ and $r_{\rm vir}$ we use the values calculated with *ROCKSTAR*.

To perform the fit we then logarithmically weight every point in the profile. Specifically, the function we minimise when fitting to a profile is:

$$S = \sum_i w_i \Big(\log(\rho_{\rm model}(r_i)) - \log(\rho_{\rm data}(r_i)) \Big)^2 \,, \tag{4.11}$$

with the weights: $w_i = \log(r_i/r_{i-1})$ chosen so that each point is weighted according to the logarithm of the size of the bin it represents. This would be equivalent to having bins of equal length in $\log(r)$ with equal weighting. This fitting was chosen because we fit over more than an order of magnitude in r and the density within this range also changes by more than an order of magnitude.

The fitting is performed over the range from $r = 0.004\,{\rm kpc}/h$ to $r = r_{\rm vir}$, independently for each halo. The lower bound is forced upon us by the resolution of the profiles (see

section 4.A.4) and the upper bound is where we assume the 'edge' of the halo to be.

For the NFW fits we can also plot rescaled density ρ/ρ_0, against rescaled radius r/r_s. In these units all halos with an NFW profile "collapse" onto a single curve.

One selection criterion we apply is that we only consider halos that are not in the process of merging. To determine this, we compare two measures of the halo mass. The first is the combined mass of the particles that *ROCKSTAR* associates to that halo given their six-dimensional phase-space information. The second one includes all particles, even the ones whose momenta suggest that they are not part of the halo. We only keep halos where these two mass parameters agree within 10%.

4.2.4 Extreme fluctuations

To date, the literature on UCMHs has focussed on treating these halos as isolated objects, forming in an otherwise homogeneous and uniform background. This allows analytical calculations to be made but the validity of this approximation has not been verified.

To answer how extreme the most dense region of a certain size in some larger volume is, and assuming the density perturbation δ at horizon entry to be distributed according to the Gaussian distribution with $\bar{\delta} = 0$, we can express the fraction of volume where $\delta > x$ as:

$$\begin{aligned} \frac{V_{\delta>x}}{V} &= \frac{1}{\sigma\sqrt{2\pi}} \int_x^\infty e^{\left(-\frac{\delta^2}{2\sigma^2}\right)} d\delta \\ &= \frac{1}{2}\mathrm{Erfc}\left(\frac{x}{\sqrt{2}\sigma}\right). \end{aligned} \tag{4.12}$$

If we further consider a region of the size of $(1\mathrm{kpc}/h)^3$ in a $(32\,\mathrm{kpc}/h)^3$ volume, we find that the most extreme overdensity is a 4.0-σ fluctuation. We show the distribution of the most extreme values in Fig. 4.1, which shows that a 4-σ fluctuation is the most likely value, but that values as extreme as 5.5-σ are possible if one draws from 1000 samples.

We can also reverse the question and estimate the fraction of volume where the density is greater than some threshold value. For 2 and 3 times the typical density contrast, we get this fraction to be 0.023 and 0.001, respectively. In a $(32\,\mathrm{kpc}/h)^3$ volume this corresponds to 745 and 44 regions of $(1\mathrm{kpc}/h)^3$ size. Assuming that all peaks are randomly placed independently of each other, an estimate of the distance between the most overdense region and the one with overdensity greater or equal to twice the typical is given by $32/(745)^{1/3}\mathrm{kpc}/h \simeq 3.5\,\mathrm{kpc}/h$, i.e. rather close compared to the scale of the halo itself.

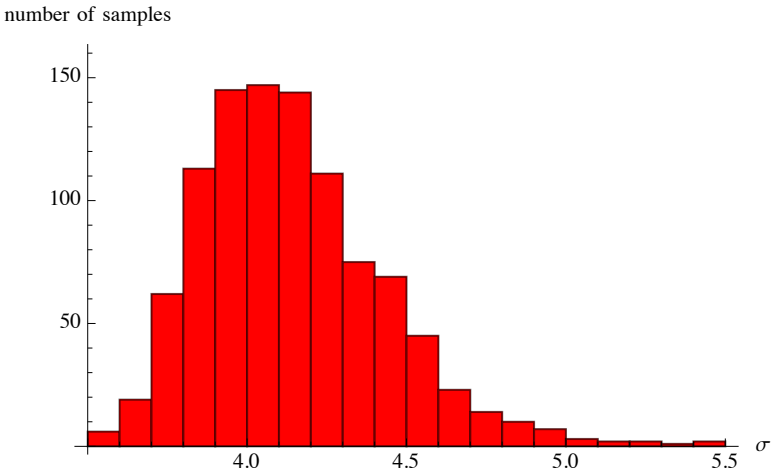

Figure 4.1: A histogram showing how many standard deviations the maximum $\delta_{1\mathrm{kpc}/h}$ is away from the average in a $32\,\mathrm{kpc}/h$ sized volume (taken from 1000 samples). To derive this histogram we have made the approximation that each $1\mathrm{kpc}/h$ region in each $32\,\mathrm{kpc}/h$ volume is independent of all the other $1\mathrm{kpc}/h$ regions in that volume.

Due to the clustering of density peaks which arises from superimposing multiple scales, the distances between large overdensities will in fact be even smaller than the estimate made above (Lumsden et al., 1989).

The spherical infall model, which leads to a steep power law profile also assumes spherical symmetry. Whilst it is true that the most extreme peaks are expected to be close to spherical initially (Bardeen et al., 1986), the unsmoothed density field will still have substructure. This substructure will grow with time and pull any matter on a purely radial trajectory off this trajectory. Moreover, gravitational tidal forces from the nearby surrounding halos will further break the spherical symmetry.

In the presence of large primordial non-Gaussianities (which are observationally unconstrained on the small scales we are interested in), one might expect the existence of isolated large-amplitude density peaks to become much more probable. For some probability density functions, extremely large-amplitude peaks do become exponentially more likely, but so do other comparably large amplitude peaks, implying that the extremely large peak will still not be isolated. For example, if the density perturbation is drawn from a chi-squared probability density function with one degree of freedom, $\delta = \delta_G^2 - \langle \delta_G^2 \rangle$, where δ_G has a Gaussian distribution (which follows in the asymptotic limit of very large local f_{NL} (Lyth, 2012)), then the typical $(32\,\mathrm{kpc}/h)^3$ volume will have a 10-σ fluctuation and the most extreme fluctuation in 1000 realisations of the initial conditions will have a 20-σ fluctuation, twice the amplitude of the second largest perturbation expected in the same volume. Furthermore, the mode coupling between different scales would in practice mean that the largest overdensity is likely to be situated close to the second largest per-

turbation, and so it still appears to be very hard to come up with a situation in which a large amplitude perturbation is likely to form in isolation from its nearest neighbours. We will show in Sec. 4.3.2 that a UCMH-like halo can form if we place a smooth, spherical overdensity surrounded by perturbations with a typical amplitude 15 times smaller. It would be interesting to find a model of the early Universe capable of generating comparable initial conditions.

4.3 Gaussian-profile spherical overdensity.

4.3.1 A completely isolated halo

We first simulate an isolated, spherically symmetric overdensity to test the theoretical prediction of a power-law profile (4.1). For the initial profile of the overdensity we chose a three-dimensional function with a Gaussian profile

$$\delta_{\rm in}(r) = A \exp\left(\frac{-r^2}{2\sigma_w^2}\right), \tag{4.13}$$

where A represents the initial amplitude of the seed overdensity in the center, and σ_w regulates the size of the overdensity. We place the overdensity at the center of the box and r denotes the distance from this center. We have set $\sigma_w = 0.5\,{\rm kpc}/h$ so that the overdensity is well-contained inside the simulation volume. We set $A = 0.3$ at initial redshift $z_{\rm in} = 10\,000$ such that the perturbation starts off marginally within the linear regime but quickly triggers the spherical collapse process shortly after matter-radiation equality. After some time the collapse dynamics give rise to a self-similar steady-state and we determined the slope of the density profile by fitting

$$\rho(r) = Cr^{-\alpha}, \tag{4.14}$$

which in log-log space is just a straight line with the slope $-\alpha$. In Fig. 4.2 we show that we indeed obtain a $\rho(r) \sim r^{-\alpha}$ profile. It is not precisely $\alpha = -9/4$, but this is not entirely unexpected because of numerical instabilities (Vogelsberger et al., 2009; Lithwick and Dalal, 2011) and the fact that $\alpha = -9/4$ is only the coarse-grained form of this type of structure growth.

Collisionless particles that can freely move through the center of the overdensity form caustics, which can be seen as additional structure at the edges of profiles. This effect is

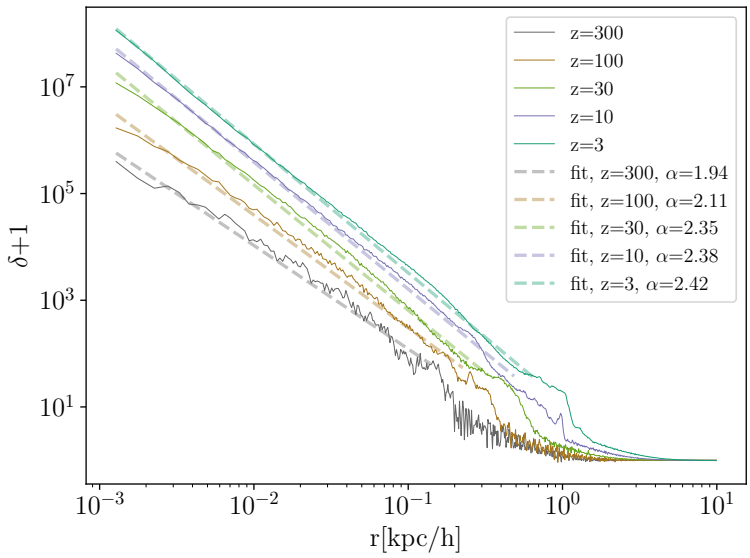

Figure 4.2: The profile of the Gaussian-seed halo in the absence of all other perturbations. We fit the power-law and thus obtain the parameter α. The number of particles used for this simulation was 512^3. By $z = 3$ the halo mass has grown to $1.8 \times 10^4 M_\odot/h$, which is still a negligible fraction of the total mass inside the box (meaning that the finite box size is not slowing down the halo accretion).

physical and we have tested that by changing the resolution of the simulation, as shown in Fig. 4.20.

4.3.2 Peak-to-background ratio 15

Having seen that we can form a UCMH starting with a spherically symmetric overdensity surrounded by a homogeneous background, we will now investigate how the evolution of the central halo changes when we drop the assumption of a homogeneous background. Following the discussion in Sec. 4.2.4, we would not expect the amplitude of the central halo to be more than about five times larger than the typical amplitude of the other perturbations. We study that case in Sec. 4.3.3. Here we study as an intermediate case the situation where the amplitude of the typical fluctuations in the box smoothed on the same kpc/h scale were 15 times smaller.

Given our choice of $A = 0.3$, we can make the typical amplitude of the perturbations 15 times smaller by boosting the standard ΛCDM power spectrum by a factor of 16 on all scales relevant to our simulation, meaning that the linearised root-mean-square perturbation (excluding the large amplitude central halo) is 4.0 times larger than it would be in ΛCDM on all scales. Starting from such initial conditions we simulate and study the formation and evolution of halos. A snapshot at redshift $z = 30$ is illustrated in Fig. 4.3.

To determine α, the slope of the profile in log-log space, we fit the linear function

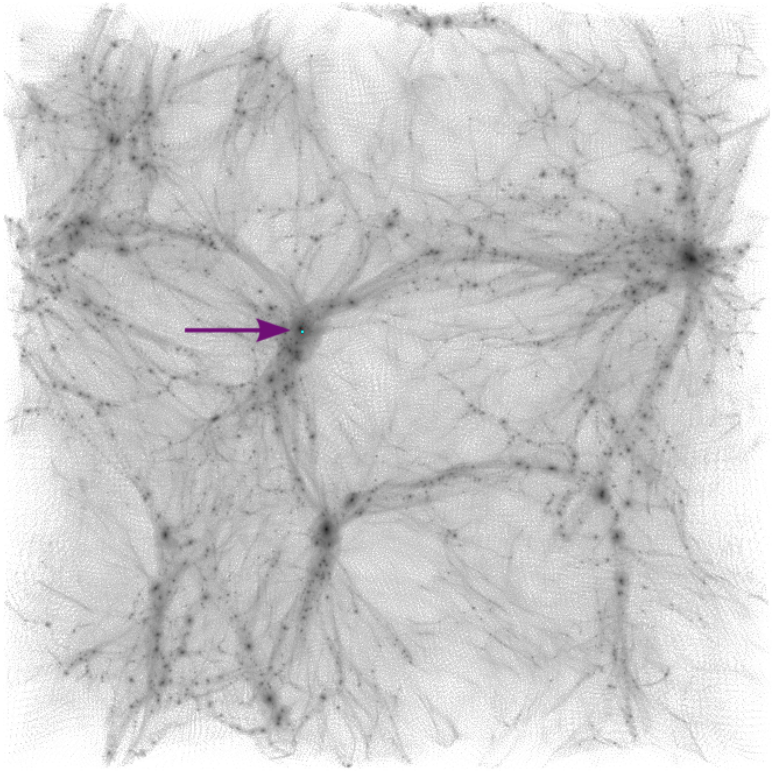

Figure 4.3: Slice through the simulation box at redshift $z = 30$ for the peak-to-background ratio 15 simulation. The halo, marked by the arrow, that was seeded by the Gaussian overdensity peak is slightly to the left and to the top of the center, highlighted in light blue.

(4.14) to the central halo.[2]

In Fig. 4.4 we show a scatter plot of the slope parameter α against the virial mass for every halo in this simulation (at $z = 100$ and $z = 30$). The red circle in each panel represents the seed halo that started with amplitude 15 times the background. The seed halo clearly has an exceptional slope compared to its background, even down to $z = 30$.

In Fig. 4.5 we show the density profiles of halos at multiple redshifts. For $z = 100$ we show a random sub-sample of halos with a mass $M_{\rm vir} > 10^2 M_\odot/h$ and for the other three redshifts the mass cut is $M_{\rm vir} > 10^3 M_\odot/h$. We also include a histogram of α values for all of the halos that pass this mass cut. It is again clear that amongst the most massive halos the seed halo's slope remains exceptional, even down to $z = 10$ (although less and less so as the background structure develops).

Finally, in Fig. 4.6, we collapse the halo profiles on to the NFW function in the manner described at the end of section 4.2.3 (we apply the same mass cuts as for Fig. 4.5). We also show a histogram of the difference in the value of our fitting statistic S, eq. (4.11) for the best fitting power-law and NFW profiles (i.e. $S_{\rm PL} - S_{\rm NFW}$). It is clear from the

[2]Since halos move around the simulation volume, it is not always obvious which halo formed from the Gaussian overdensity. We identified that halo by tracking one of the particles that was initially closest to the center of the simulation volume. At each redshift, we looked for the halo that contained the tracked particle at its core.

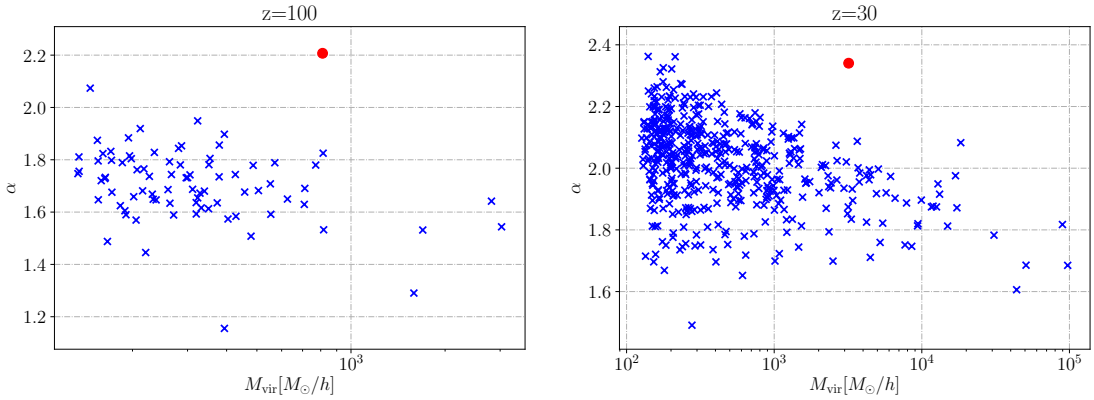

Figure 4.4: The best-fit power-law exponent α for all halos in the peak-to-background 15 simulation at $z = 100$ and 30. The special halo has an exceptionally steep slope compared to all other halos with a comparable mass.

profiles that the NFW profile is not an excellent fit for the special seed halo. There is a noticeable upturn at small r/r_s. Also note how far to the right the special halo's profile extends in each panel. This is a consequence of the NFW fit requiring a small r_s value, exceptionally smaller than any other halo that satisfies the mass cuts.

We cannot resolve the profile of any halo on scales below the resolution limit of our simulation. However, because the special halo remains exceptional compared to its background, even down to $z = 10$, it seems reasonable to expect that the profile would remain close to a power-law even beyond the limits of our resolution.

4.3.3 Peak-to-background ratio 5

We now increase the amplitude of the surrounding perturbations even more and repeat the analysis. In the results of this subsection the central overdensity is only 5-times larger than a typical one. A snapshot at redshift $z = 30$ is shown in Fig. 4.7.

Figs. 4.8, 4.9 and 4.10 are analogous to Figs. 4.4, 4.5 and 4.6, however for the simulations with even larger background perturbations and showing only $z = 100$ and $z = 30$.

The most striking observation to make is that the special halo is no longer at all exceptional compared to its surroundings. Its slope compared to its mass is large compared to other halos in the simulation, but not exceptionally so. Moreover, its value of $S_{\rm PL} - S_{\rm NFW}$, although still favouring a power-law, is not at all special compared to other halos, some of which also favour the power-law.

We cannot say what happens below the limits of our resolution; however it is clear that when an initial, spherically-symmetric perturbation is embedded in a background 5 times smaller it is no longer exceptional at least by $z = 100$. Therefore it does not behave

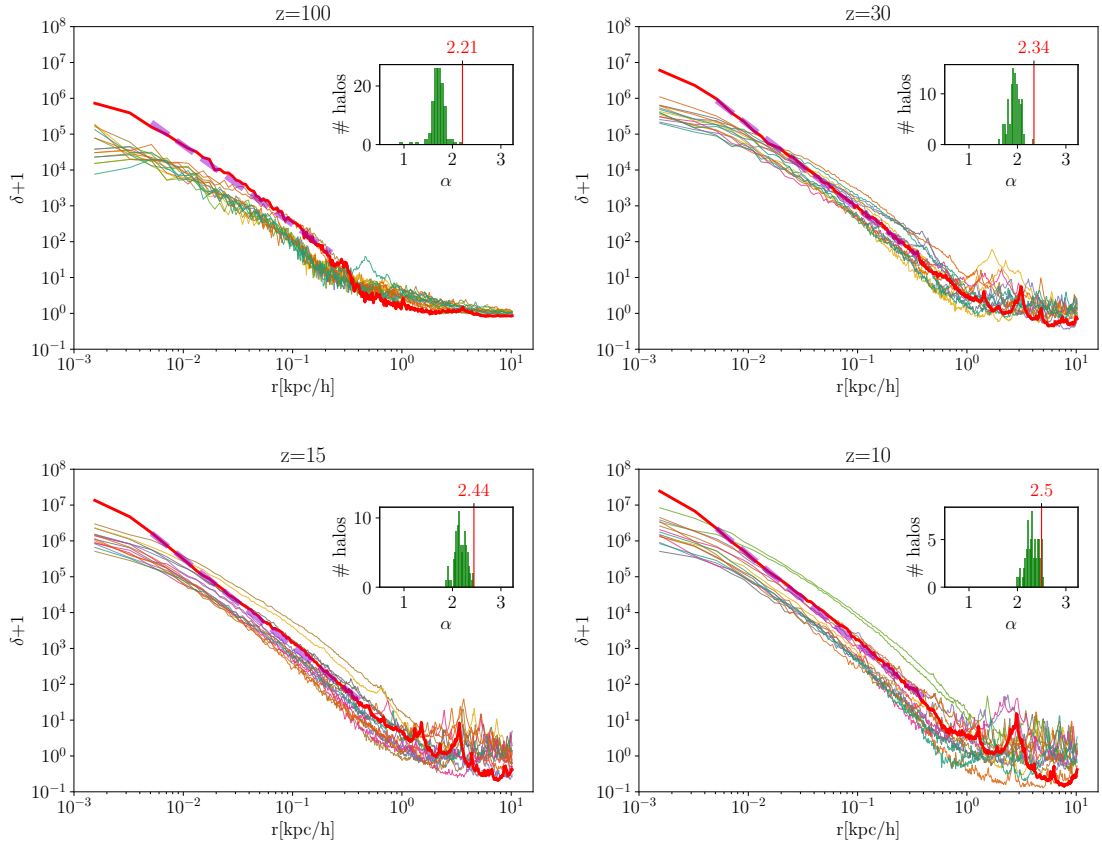

Figure 4.5: The profiles of the halos in the peak-to-background ratio 15 simulation at $z = 100, 30, 15$, and 10. The profile of the halo descending from the seed halo is highlighted in red so it can be distinguished from the other halos. For each snapshot, we fit the profiles to eq. (4.14) and present the resulting α in a histogram. The range we fit over is r between $0.004\,\mathrm{kpc}/h$ and r_{vir} for each halo individually. To plot the profiles, for $z = 100$ we only kept halos with $M_{\mathrm{vir}} > 10^2 M_\odot/h$ and for $z = 30, 15, 10$ we kept the halos with $M_{\mathrm{vir}} > 10^3 M_\odot/h$. The power-law fit to the seed halo's profile is plotted as a violet dashed line.

as if it was in a homogeneous background and it is reasonable to assume that it has not formed a UCMH-like profile on smaller scales. Although we do not show it here, this holds even at $z = 300$.

4.3.4 Summary of special halo simulations

In this section we have shown that as the background of an initial spherically-symmetric perturbation is increased, the halo descending from this seed perturbation becomes less and less exceptional. This might not appear too surprising, however it isn't trivial that an initial 5-σ fluctuation at $z = 10\,000$ will be entirely unexceptional by $z = 100$.

The conclusion we take from this section is that unless a fluctuation has an initial amplitude at least between 5 and 15 times larger than the typical background fluctuations its halo will soon become comparable in slope, mass and density to many other nearby halos. Unless the perturbation is more extreme initially than one would expect to find

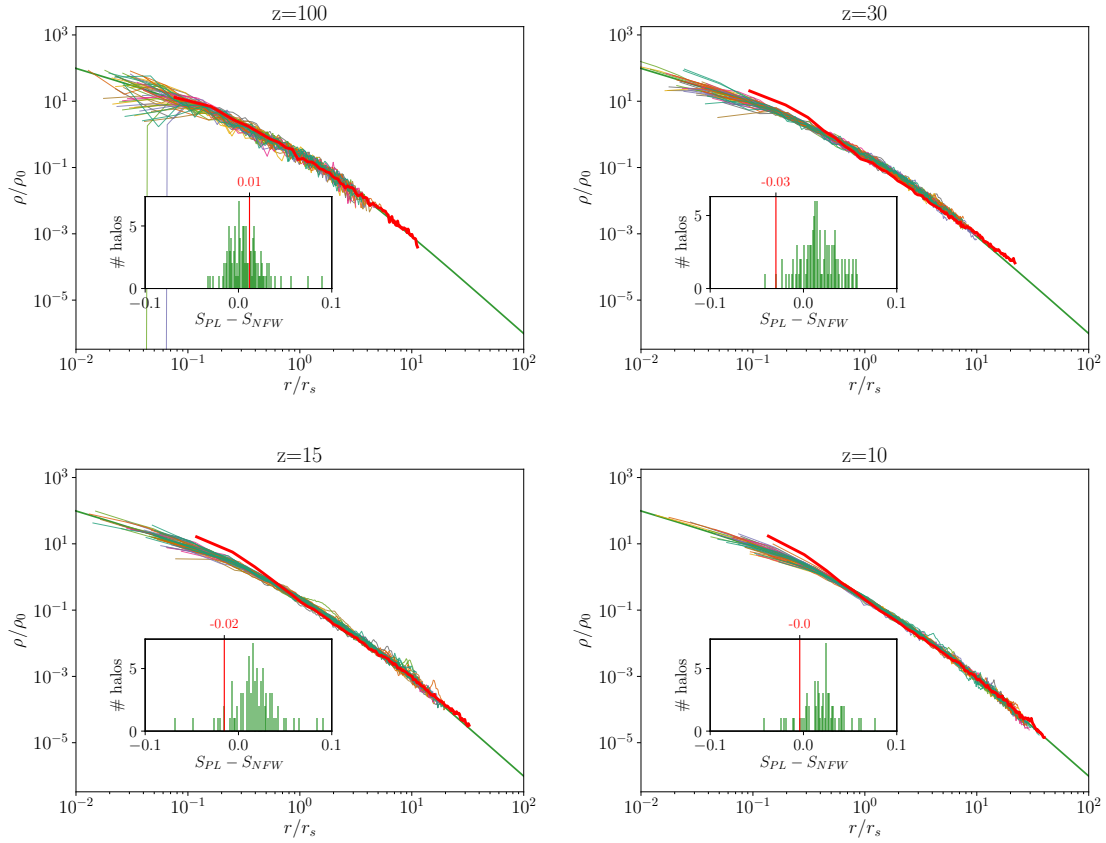

Figure 4.6: The rescaled profiles of halos in the peak-to-background ratio 15 simulation. The NFW analytical prediction is shown in green and the descendant of the seed halo is highlighted in red. Histograms show the difference of a measure for goodness of fit between the power-law and NFW profile. A negative value of this quantity points towards the power-law being a better fit than NFW. With the exception of $z = 100$, the special halo seems to favour power-law profile over NFW. The exceptionality is particularly noticeable near the center of the halo. Fitting the special halo with an NFW profile gives a very small r_s. Here this is manifested by the special halo's profile being shifted towards larger radii than any other halo.

given Gaussian initial conditions, see Sec. 4.2.4, it will not grow into a UCMH-like halo.

We stress that this is not the result of lowering the density of the initial seed fluctuation. The initial profile was identical in all three subsections; the only thing that was changed was the amplitude of background fluctuations. Therefore, when examining the evolution of objects on the very small scales in the early Universe, a single density contrast δ_c is not enough to describe the subsequent evolution. The evolution depends sensitively on the environment and therefore any constraints must too.

4.4 Boosting the power spectrum around the $1\,\mathrm{kpc}/h$ scale

In this section we no longer consider the evolution of a specific overdensity peak that was planted *by hand*. Instead, we increase the probability of extreme *random* fluctuations on a similar scale by boosting the variance of the primordial perturbation modes over some

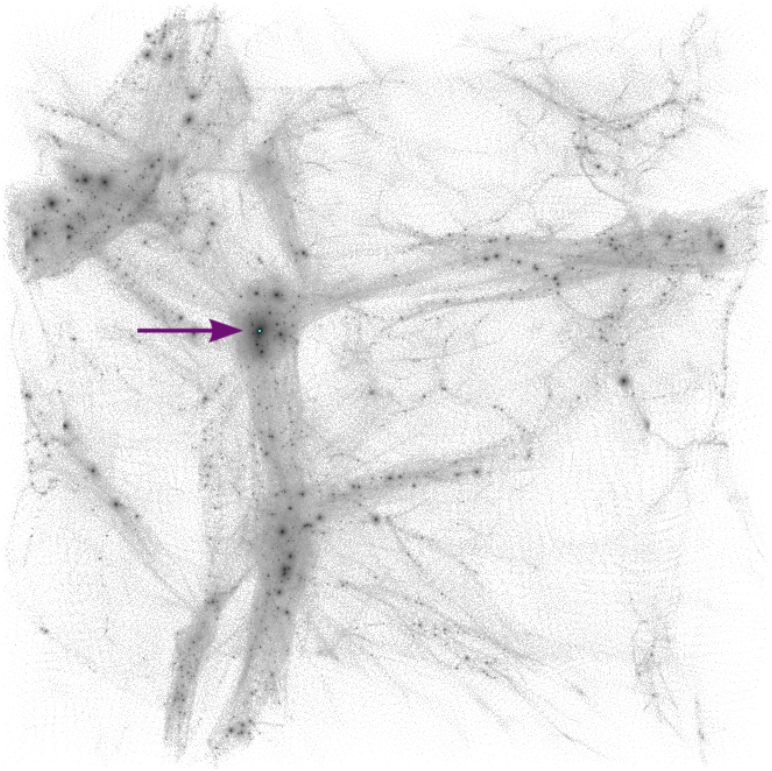

Figure 4.7: Slice through the simulation box at redshift $z = 30$ for the peak-to-background ratio 5 simulation. The halo, marked by the arrow, that was seeded by the Gaussian overdensity peak is slightly to the left and to the top of the center, highlighted in light blue.

range of scales. In principle this boost can take many forms (e.g. a step, or a bump in Fourier space) and the precise nature of structure formation will depend on the form of the boost. However, UCMHs are claimed to form with a sufficiently large abundance to be observed under *any* boost of the power spectrum with sufficiently large amplitude.

We see no halo with convincing UCMH properties; however we are somewhat limited by the resolution. We do however see many compact structures. With hindsight, this is not surprising either. If we boost the primordial spectrum then structures on the boosted scales form earlier. This means these structures form when the Universe is denser. Therefore they also reach a larger virial density than they would have had they formed from a non-boosted initial power spectrum.

Note however this is not only true for the most extreme, and therefore rare, structures forming under a boosted power spectrum. In fact *every* structure that forms on the boosted scales forms earlier and is therefore more compact. As a consequence, even though we do not find structures as compact as a hypothetical UCMH, the structures we find may, due to their increased abundance, have their own unique cosmological signals. It would be useful and interesting future work to examine how the new type of compact halos we describe depend on the specific nature of the boost to the power spectrum.

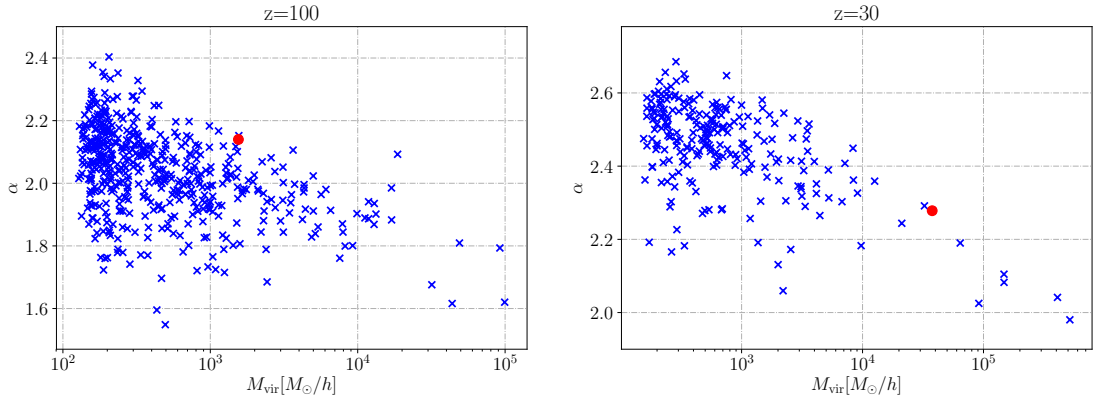

Figure 4.8: Figures analogous to Fig. 4.4, but for the peak-to-background-ratio 5. The power-law parameter α of the halo, formed from the special seed, is no longer very different from the other halos.

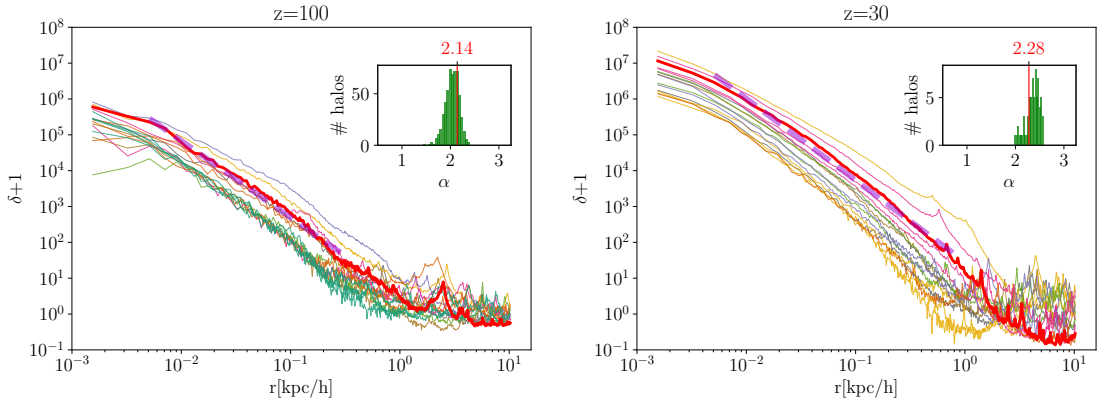

Figure 4.9: The profiles of the halos in the peak-to-background ratio 5 simulation at $z = 100$ and 30. We have again only included halos with $M_{\rm vir} > 10^2 M_\odot/h$ for the $z = 100$ profiles and $M_{\rm vir} > 10^3 M_\odot/h$ for $z = 30$. The profile of the descendant of the seed halo is again highlighted in red. Unlike the situation in the peak-to-background 15 simulation, the slope of the special halo is no longer more extreme than the other halos in the box.

The form of our boost in the power spectrum is as follows. Firstly we take the following unboosted power-law power spectrum of the primordial curvature perturbation ζ, $\mathcal{P}_0^\zeta(k) = A_s\,(k/k_{\rm pivot})^{n_s-1}$ with $A_s = 2.26\times10^{-9}$, $k_{\rm pivot} = 0.05$ Mpc^{-1} and $n_s = 0.96$.

We then boost this power spectrum to form the primordial power spectrum used for our simulations, $\mathcal{P}^\zeta(k)$. Specifically,

$$\mathcal{P}^\zeta(k) = \mathcal{P}_0^\zeta(k)\,(1 + B(k)) \tag{4.15}$$

where

$$B(k) = A_b \exp\left(-2.77\,(\ln k - \ln k_\star)^2\right). \tag{4.16}$$

The scale at which we boost the simulation's power spectrum is $k_\star = 1\ h$kpc^{-1}.

The value of 2.77 in the definition of $B(k)$ is chosen such that the full width at half maximum of the boost is 1 (in units of $\ln k$). This means that our power spectrum is

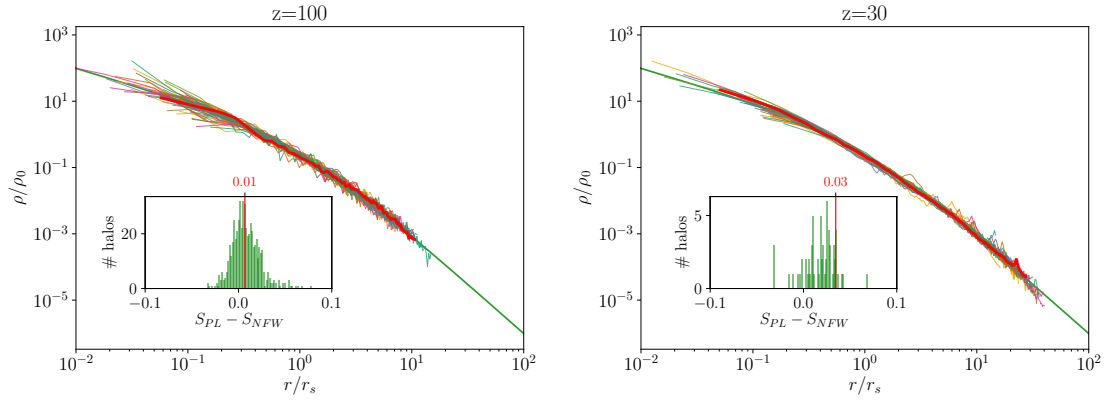

Figure 4.10: The rescaled profiles of halos in the peak-to-background ratio 5 simulation. The analytical prediction is shown in green and the special halo is highlighted in red. In contrast to the peak-to-background ratio 15, the special halo does not appear distinguishable from the rest. The $S_{\rm PL} - S_{\rm NFW}$ measure also demonstrates the profile of the special halo to be a better fit to NFW than to power-law (note a smaller value of S indicates a better fit, see equation (4.11) and the discussion around it).

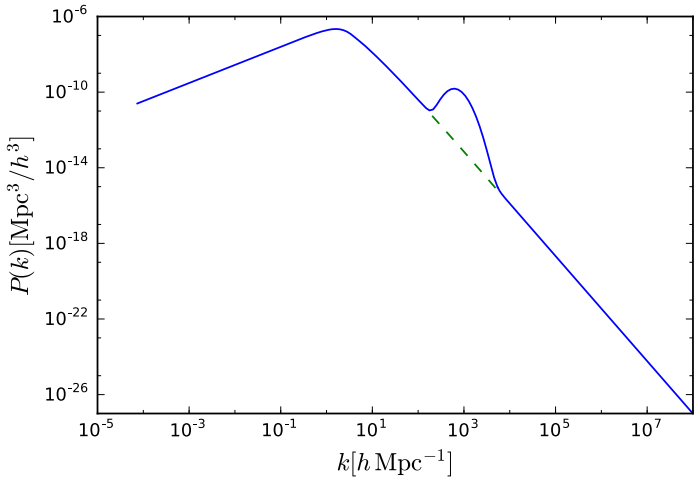

Figure 4.11: Boosted matter power spectrum used in our simulations. Plot shown has boost parameters $A_b = 10^3$ and $k_\star = 1\ h\mathrm{kpc}^{-1}$ from eq. (4.16). The matter power spectrum has been calculated using CAMB and is outputted at $z = 100\,000$. Note that this is only the dark matter power spectrum.

boosted over a width corresponding to approximately one efolding, which is a natural length scale during inflation.

Before starting each simulation we use *CAMB* (Lewis et al., 2000) to calculate the linear transfer functions and hence the matter power spectrum at the simulation's starting redshift. The shape of such a boosted power spectrum is plotted in Fig. 4.11 for $A_b = 10^3$, $k_\star = 1\ h\mathrm{kpc}^{-1}$ and at redshift $z = 100\,000$. Note that this is the power spectrum of dark matter only. The power spectrum of baryons is significantly different due to baryons still being tightly coupled to photons at this high redshift.

We also show σ_R (i.e. the rms of the density contrast smoothed by a spherical tophat on a scale R) in Fig. 4.12 for the same input power spectrum with four different boost amplitudes at the same redshift.

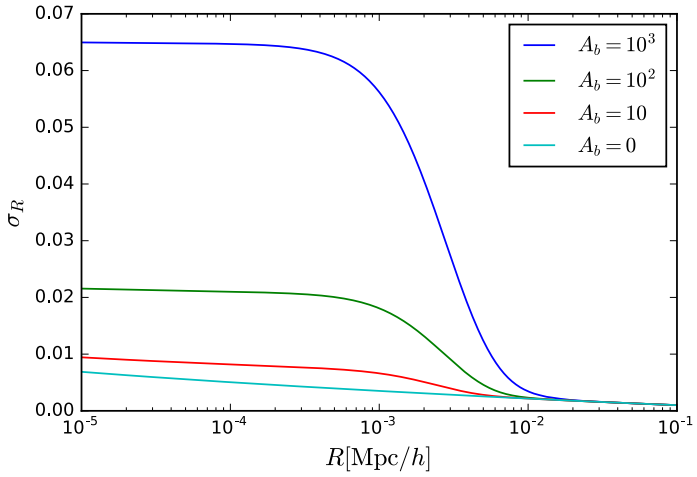

Figure 4.12: The root-mean-square fluctuations of the density perturbation when smoothed with a tophat filter of radius R (i.e σ_R). This is for the same input power spectrum as that shown in Fig. 4.11 with four different boosts and at the same redshift.

We ran simulations with boosts of $A_b = 0, 10, 100$ and 1000. Each simulation was given the same seed. At $z = 100\,000$ the largest fluctuation in the $A_b = 1000$ simulation, when the density was smoothed with a spherical tophat filter of radius $1\,\mathrm{kpc}/h$ was $\delta_R = 0.23$. With this boost, σ_R at this radius and redshift is 0.054 therefore this corresponds to a 4.3-σ fluctuation.

We start each simulation at $z = 5 \times 10^6$ and run them to $z = 15$. We do not go to lower redshifts than this because at $z = 10$ the scale of our box, $32\,\mathrm{kpc}/h$, becomes non-linear. Snapshots at redshift $z = 30$ are illustrated in Fig. 4.13.

4.4.1 Results of boosted simulations

As might be expected, given our results from section 4.3, we find that most of the halos fit NFW profiles better than power-law (see Figs. 4.14 and 4.15). Moreover, there are no obvious exceptional halos, even when we set $A_b = 10^3$. There are a few halos that fit the power-law better than NFW; however none stand out as much as the special halo in the peak-to-background 15 simulation in section 4.3.2 (see, for example, the red line in Fig. 4.6 for $z = 30$, 15 and 10). We expect this better fit arises here simply because our resolution is not good enough to resolve the r_s of the NFW profile for these *lower mass* halos. A similar effect was seen for the non-special halos in the previous section.

Histograms of the concentration parameter c are shown in Fig. 4.16. At redshift $z = 30$, concentration parameters of $c \gtrsim 100$ can occur for the $A_b = 10^3$ simulation. Given that we expect this to grow with time, the concentration today would be much larger. This shows

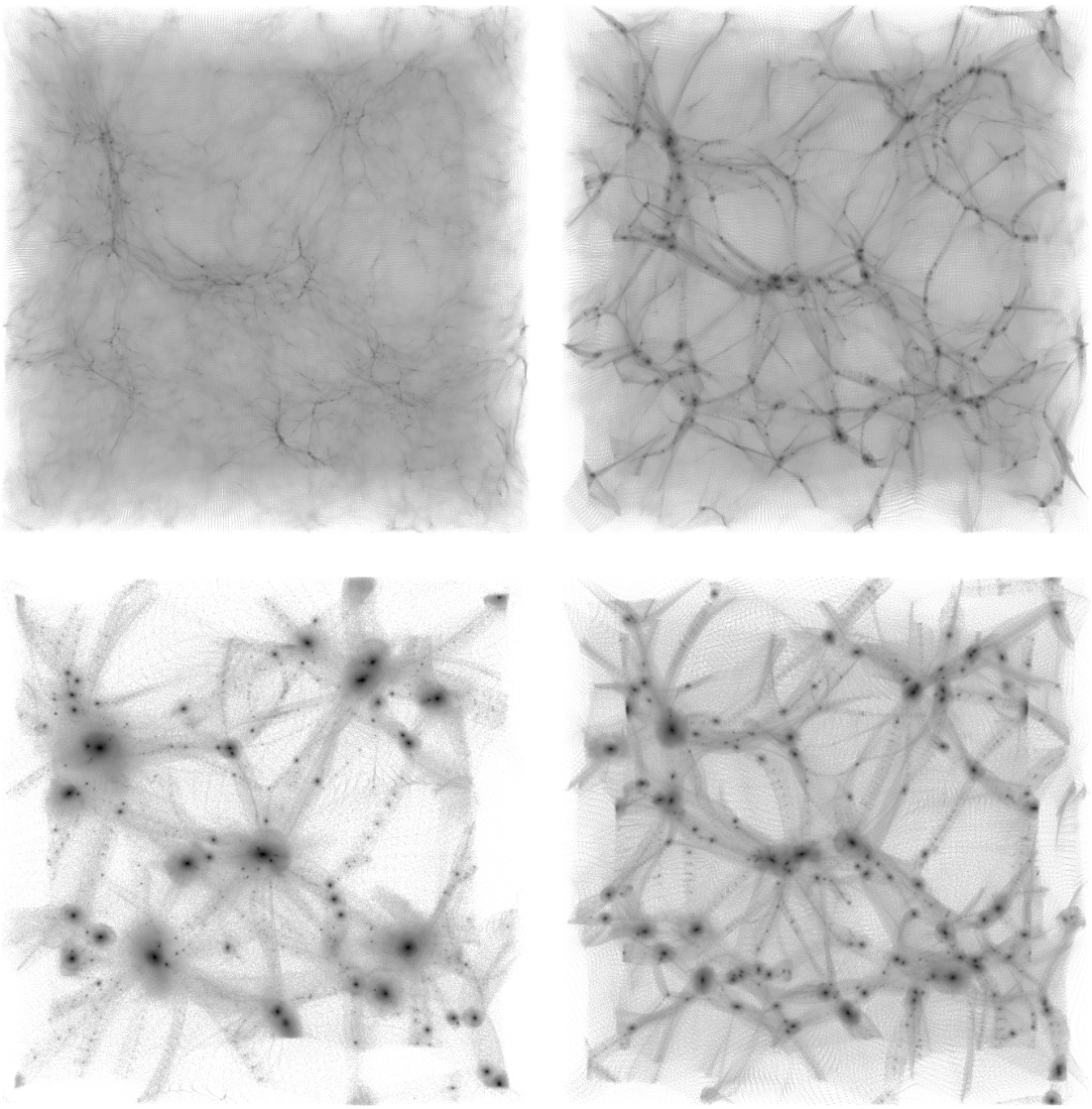

Figure 4.13: Slices through the simulation volume at redshift z = 30 for the simulations with boosted power spectrum. The amplitudes of the boosts are $A_b = 0, 10, 100, 1000$, clockwise, starting from the top left.

that although there may be no UCMH candidates in our simulations the structures that do form are still much more compact than those in a simulation without a boosted power spectrum. It is worth stressing again that when the input power spectrum is boosted *all* the structures that form are much more compact. It is not just the rare, extreme fluctuations that experience this effect. This is because the boosted initial conditions form structures earlier, when the whole universe was more dense. Therefore these structures also virialise at much larger densities and remain much denser at later times.

A similar, but less pronounced effect is also seen for the smaller boosts.

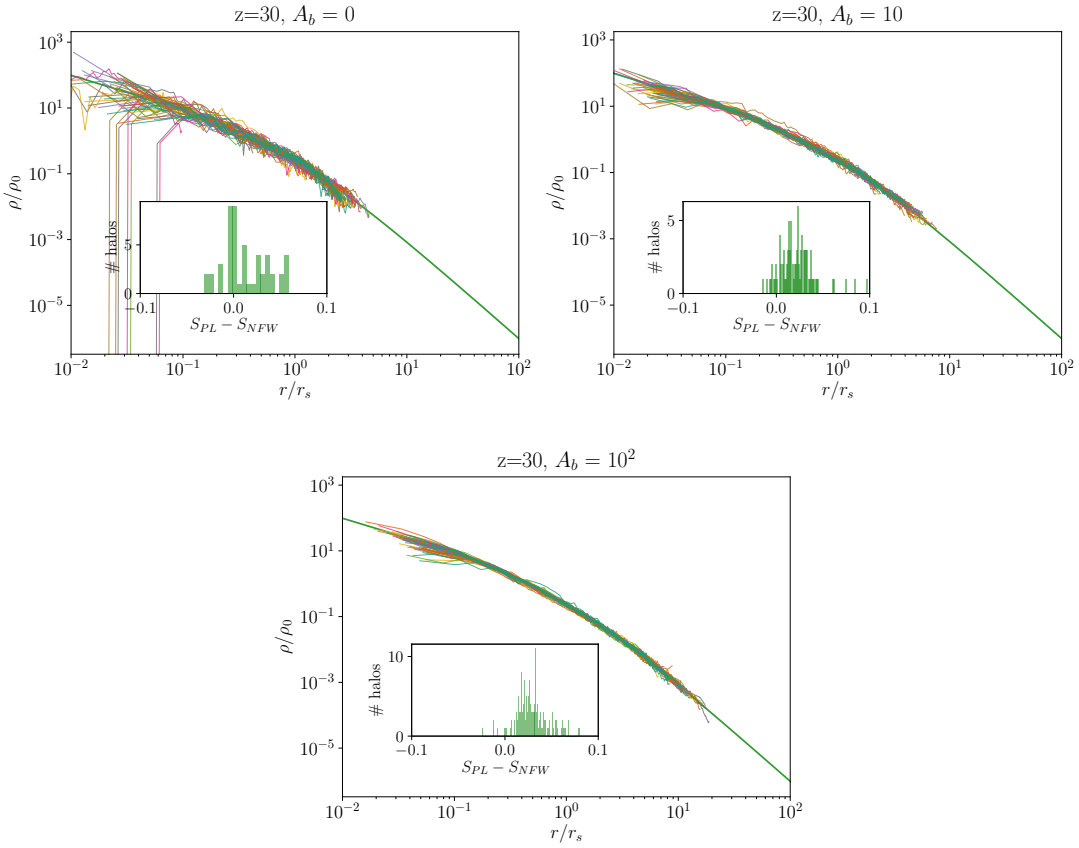

Figure 4.14: The evolution of halos' profiles with the increasing amount of boost. The NFW analytical prediction is shown in green. Histograms show the difference of a measure for goodness of fit (equation (4.11)) between the power-law and NFW. Almost all halos seem to be a better fit to NFW than to power-law.

4.5 UCMH OBSERVABILITY AND WIMP ANNIHILATION

Numerous observational tests have been either proposed or enacted to constrain the number density of UCMHs, and these observational limits translate into upper bounds on the primordial power spectrum. These constraints assumed a dense $r^{-9/4}$ inner profile of the halos, which we have shown to be unlikely to form. In this section we briefly calculate how the observability of these halos changes when using an NFW halo with a large concentration parameter, of the form observed in our simulations. Whilst calculating the constraint on the power spectrum goes beyond the scope of this work, we use our simulation results in this section to show how the expected signature of WIMP annihilation in the dense center of the halos reduces when using a realistic halo density profile.

The expected gamma-ray flux from WIMP annihilation within a halo at distance d from the Earth is given by (Josan and Green, 2010b):

$$\Phi_\gamma = \frac{\Phi_{\text{astro}}\Phi_{\text{particle}}}{2d^2} \tag{4.17}$$

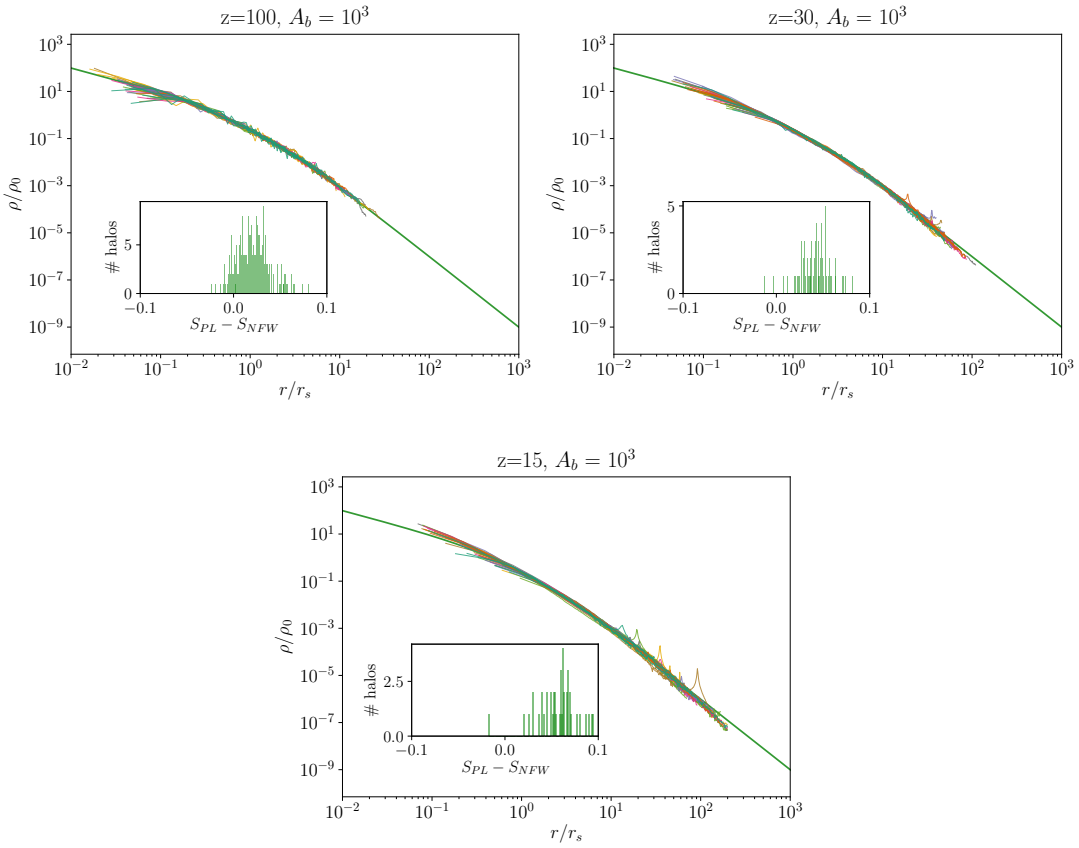

Figure 4.15: The rescaled profiles for $A_b = 10^3$ at $z = 100$, 30 and 15. From the positions of the lines on top of the NFW reference line it is clear that r_s is getting smaller as time increases. As with Fig. 4.14 the NFW profile is a better fit than a power-law for almost all of the profiles.

where Φ_{particle} depends on the WIMP particle mass and annihilation cross section, which is assumed to be independent of the halo properties, e.g. the velocity distribution of the particles (see Bringmann and Weniger (2012) for a justification).

The astrophysical part is given by an integral of the density squared

$$\Phi_{\text{astro}} = \int_0^{r_h} \rho(r)^2 r^2 \mathrm{d}r \tag{4.18}$$

where r_h is the radius of the halo, which we always take to be r_{vir}. In practice, although the majority of the NFW halo mass is within the outer part of the profile where $\rho \propto 1/r^3$, the annihilation signal is dominated by the innermost part with the greatest density, which satisfies $r < r_s$ so it does not matter much where we cut-off the integral. Note that the physical radius and density must be used.

For halos with an $r^{-9/4}$ profile, the signal is dominated by the central density, which must be cut off at some maximum value. Bringmann et al. estimate a maximum possible

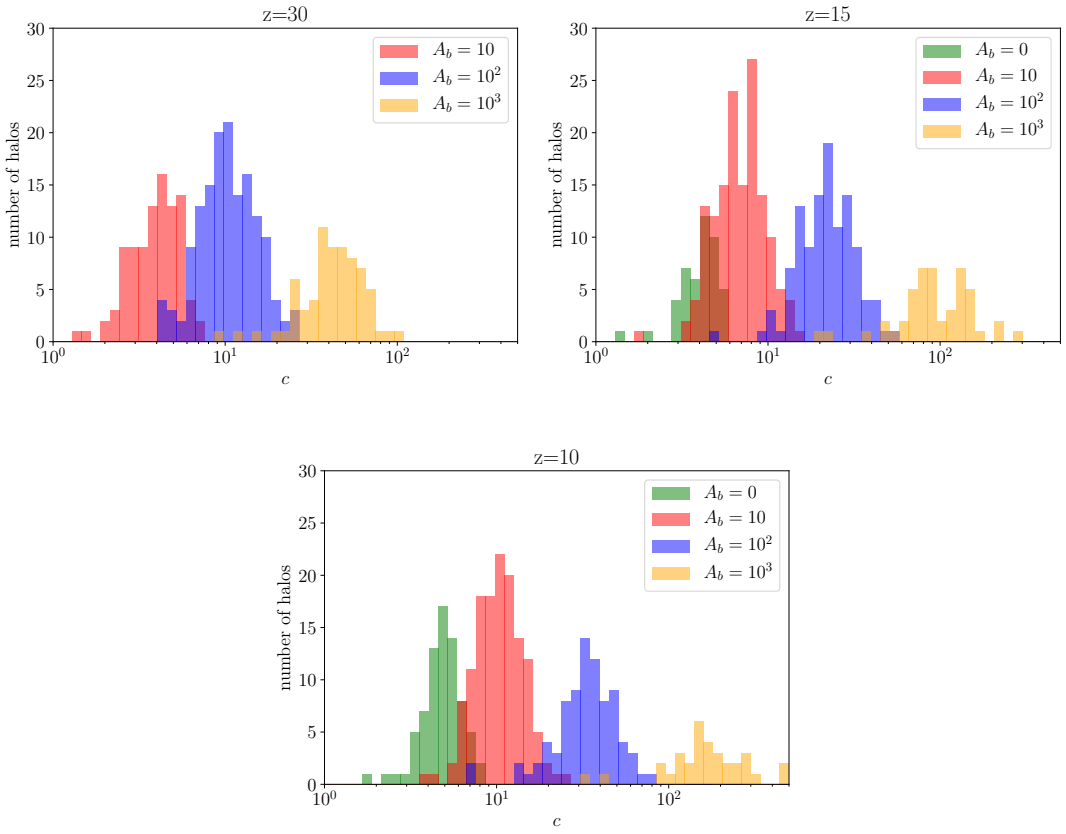

Figure 4.16: Concentration parameter c for the halos in simulations where we boosted the power spectrum. The halos in higher-boost simulations are much more compact. Concentration also grows with time. We only retain halos with $M_{\rm vir} > 10^2 M_\odot/h$. Note that at $z = 15$ there already exist halos in the $A_b = 10^3$ simulation with $c > 200$.

density of the UCMHs today of

$$\rho_{\rm max} \simeq \frac{m_\chi}{\langle\sigma v\rangle(t_0 - t_i)} = K\rho_{c,m}, \tag{4.19}$$

where

$$K \simeq 5 \times 10^{16}, \tag{4.20}$$

calculated assuming fiducial values of the WIMP mass $m_\chi = 1\,\text{TeV}$, thermally averaged cross section $\langle\sigma v\rangle = 3 \times 10^{-26}\text{cm}^3\text{s}^{-1}$, and the age of the Universe $t_0 = 13.7\,\text{Gyr}$. The UCMH formation time t_i is irrelevant provided that $t_i \ll t_0$ (Bringmann and Weniger, 2012). The critical density of the Universe today is $\rho_c = 415 M_\odot h^2/\text{kpc}^3$, and $\rho_{c,m} \equiv \Omega_m \rho_c$. The UCMH profile is given by

$$\rho_{\rm UCMH} = \begin{cases} \rho_{\rm max} & \text{if } r < r_{\rm cut}, \\ \rho_{\rm max}\left(\frac{r}{r_{\rm cut}}\right)^{-\frac{9}{4}} & \text{if } r > r_{\rm cut}. \end{cases} \tag{4.21}$$

Using the definition of the virial mass in terms of the virial radius (which is independent

of the density profile)

$$M_{\rm virial} = \frac{4\pi}{3} 178 \rho_{c,m} r_{\rm vir}^3, \tag{4.22}$$

where $\rho_{c,m}$ is the critical density of matter (of both CDM and baryons, because our simulations treat them equally). Calculating the density contrast centered on a UCMH to a radius $r_{\rm vir}$

$$\begin{aligned} 1 + \delta_{\rm UCMH}(r_h) &= \frac{1}{\rho_{c,m}} \frac{3}{r_{\rm vir}^3} \int_0^{r_{\rm vir}} \rho_{\rm UCMH}(r) r^2 dr \\ &\simeq 4K \left(\frac{r_{\rm cut}}{r_{\rm vir}} \right)^{9/4}, \end{aligned} \tag{4.23}$$

leads to

$$\frac{r_{\rm cut}}{r_{\rm vir}} \simeq \left(\frac{179}{4K} \right)^{4/9} \ll 1. \tag{4.24}$$

Using the above results, we find the WIMP-annihilation signal is

$$\Phi_{\rm astro,UCMH} \simeq {r_{\rm cut}}^3 \rho_{\rm max}^2 = K^{2/3} \left(\frac{179}{4} \right)^{4/3} r_{\rm vir}^3 \rho_{c,m}^2. \tag{4.25}$$

For an NFW profile, we can similarly evaluate (4.18) to calculate the WIMP-annihilation signal from such a halo, and then compare it to the UCMH result for a halo with the same mass (and hence the same $r_{\rm vir}$),[3]

$$\begin{aligned} \Phi_{\rm astro,NFW} &= r_s^3 \rho_0^2 \frac{c(3 + c(3 + c))}{3(1 + c)^3} \\ &= 1.2 \times 10^3 r_{\rm vir}^3 \rho_{c,m}^2 \frac{c^4 (3 + c(3 + c))}{(1 + c)^3} \\ &\times \frac{1}{(\log(1 + c) - c/(1 + c))^2}, \end{aligned} \tag{4.26}$$

where we note that the result strongly depends on the concentration parameter, $c = r_{\rm vir}/r_s$, with an approximate c^3 dependence in the limit of $c \gg 1$. For this reason the large values of c generated by boosting the power spectrum do give rise to much larger WIMP annihilation signals than would be the case with an unboosted power spectrum for halos of the same mass and also with an NFW profile. We show the mild redshift evolution of the WIMP-annihilation signal in Fig. 4.17 for all four levels of boost. Increasing A_b by an order of magnitude has a much larger effect on $\Phi_{\rm astro,tot}$, the total value of $\Phi_{\rm astro}$ added up for all halos, than the redshift evolution of any given boost with redshift. Although the WIMP-annihilation signal does initially increase with redshift for the unboosted simulation, we

[3] Although the density of the NFW profile also diverges at the center, the impact of including the maximum density restriction given by (4.19) is negligible.

expect this is a numerical artefact of many protohalos having not yet reached sufficient size to be detected by *ROCKSTAR*. Similarly, we caution that the slight decrease in $\Phi_{\mathrm{astro,tot}}$ with redshift may be due to the decreasing minimum physical length we can resolve in an expanding background, meaning that we resolves the cores of the halos less well at late times.

We calculated the WIMP-annihlation signal by integrating (4.18) which assumes spherical symmetry, and compared the result to (4.26) using the best fit values of c from Sec. 4.4.1 and r_{vir} outputs from *ROCKSTAR*, finding the results agree within a factor of 2. We note that Kohri et al. (Kohri et al., 2014) have previously shown that the WIMP-annihilation signal is extremely sensitive to the exponent α when they assumed a truncated power law profile of the form $\rho \propto (1 + r/r_{\mathrm{cut}})^{\alpha}$.

However, even for the largest values of c observed (using a boost factor $A_b = 1000$), the WIMP-annihilation signal as far as we are able to resolve it remains about a factor of 10^4 smaller than it would be for a UCMH with the same mass, which means they would have to be 100 times closer in order to be equally observable. Hence we can only observationally rule out their existence in a volume one millionth as large as could be probed for halos with $r^{-9/4}$ profiles. The NFW halos are however much more common than the assumed abundance of UCMHs given the same initial conditions, meaning that the observational constraints on the power spectrum may not weaken as strongly as may be expected, but a detailed study of this issue goes beyond the scope of this paper.

In Fig. 4.18 we explore whether there is any connection between the combinations of three different parameters: the virial mass of a halo M_{vir}, its concentration parameter c, and a measure for the WIMP annihilation signal. The WIMP-signal measure is higher for heavier halos and more compact ones. It is also significantly higher in simulations with a higher boost.

In Fig. 4.19 we show the WIMP-annihilation signal as a function of virial mass of all halos. The most interesting feature is that the WIMP-annihilation signal of the special seed in the peak-to-background 15 simulation is an order-of-magnitude larger than any of the other halos in the same simulation with comparable mass. If we had better resolution, we expect that the WIMP-annihilation signal from this halo would become even larger than what is plotted. The integral of the density squared is dominated by the very center of the halo where the density is largest, and this halo has a steeper profile towards the center than all of the others, see Fig. 4.5.

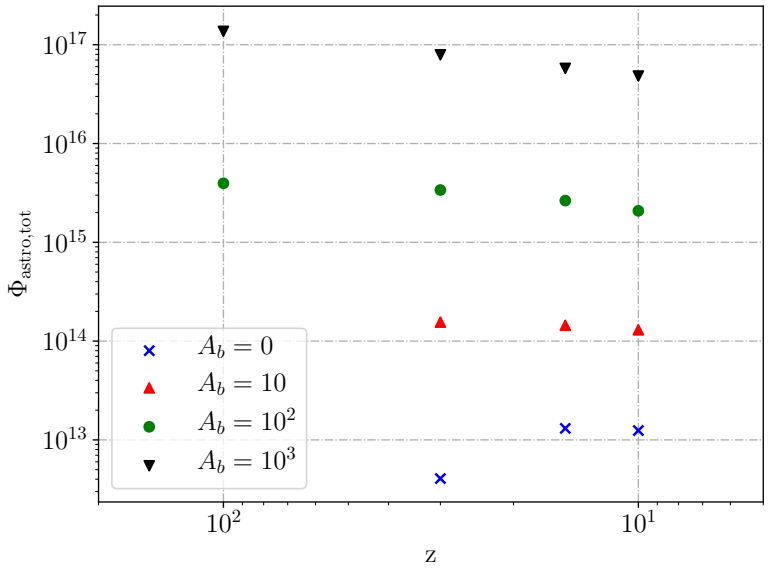

Figure 4.17: The total $\Phi_{\rm astro}$ part of the WIMP-annihilation signal from the most massive halos plotted against z for the power spectrum boosted by 4 different amounts. Notice how the strength of the signal typically decreases slowly with redshift, which we caution may be a numerical artifact, see the text after Eq. (4.26). To calculate this signal, we take into account all the halos with $M_{\rm vir} \gtrsim 3\,M_\odot$. For the two smallest boosts at $z = 100$, no such halos are identified in the simulation.

4.6 Conclusions

We have performed the first 3D N-body simulations of UCMH formation. Starting with an isolated spherical overdensity we have shown that this would form a steep power-law profile with the density scaling close to $\rho \propto r^{-9/4}$ (Bertschinger, 1985), and we are able to resolve this profile by up to 3 orders of magnitude of length scales at low redshift. When we include random density fluctuations with an amplitude typically 15 times smaller than the special halo, we observe that the halo descended from the special seed becomes somewhat disrupted, with the density profile becoming shallower towards the center (compare Figs. 4.2 and 4.5). This flattening occurs on such small scales that it does not make a significant difference to the numerical values of the halo properties we extract, such as the power-law steepness α or the WIMP-annihilation signal. Since the WIMP-annihilation signal is dominated by the square of the density in the core of the halo, our estimates for the WIMP-annihilation signal present only the lower bound on this quantity, due to the limitations of our resolution.

However, even though the special halo flattens a little it still remains exceptional relative to the other halos that form in the simulation box. Its steepness and WIMP-annihilation signal are both much larger than any other comparable mass halo in the simulation (see Figs. 4.4 and 4.17). It is therefore likely that the inner part of this halo, unresolvable by our simulations, remains close to a power-law.

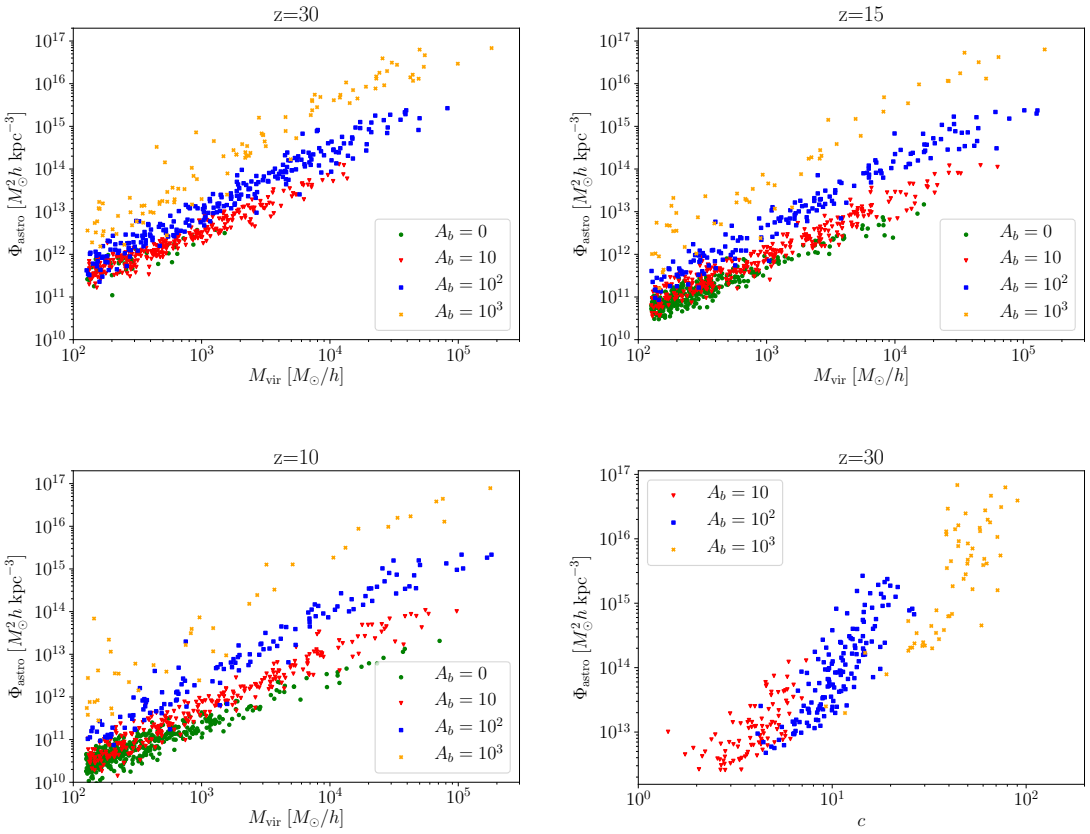

Figure 4.18: Scatter plots for the WIMP-annihilation signal plotted against $M_{\rm vir}$ for three different redshifts (top and left panels) and against c for $z = 30$ (bottom right). Different amplitudes of the boost are represented with different color. It is curious that the WIMP-annihilation signal appears to depend on concentration in a way that doesn't depend on the size of the boost. However, there is a lot of scatter in this relationship.

When we further increase the size of background fluctuations to be five times smaller than the special halo we see the special halo become further disrupted. In fact, in this simulation, even for the special halo, we find an NFW profile is a better fit than a power-law (see Fig. 4.10). Moreover, although it starts as equivalent to a 5-σ fluctuation of the background it has ceased to be exceptional even by $z = 300$. These two facts strongly suggest that even below the scales we can resolve the special halo will not have a steep UCMH-like profile.

Note that in all of these situations the initial special seed remains the same size, it is only the background fluctuations that change. Therefore, we can conclude that in order to form this UCMH-like power-law profile an initial fluctuation must be substantially larger than five times its background. Ricotti and Gould estimated that the critical density threshold for collapse into a UCMH was $\delta_c = 10^{-3}$ (Ricotti and Gould, 2009) and this estimate was refined to include a scale dependence by Bringmann et al. (Bringmann et al., 2012). We have here shown that in realistic cases δ_c is strongly dependent on the envir-

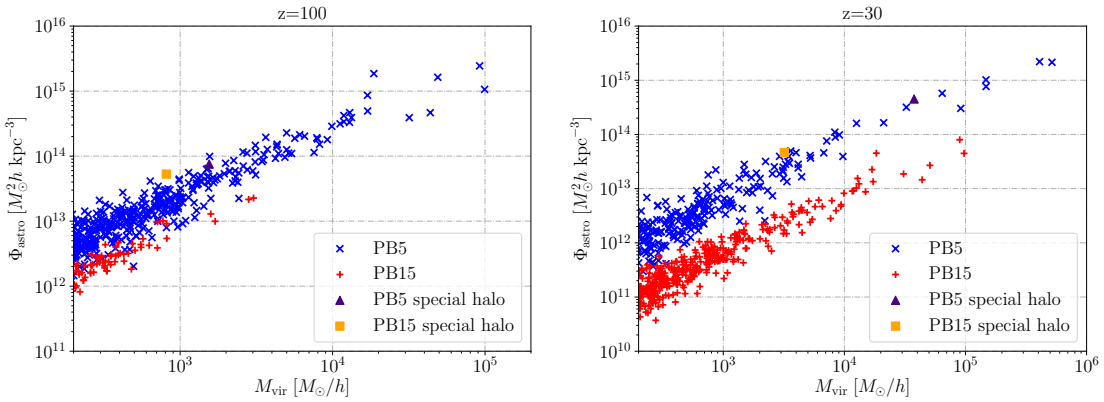

Figure 4.19: The $\Phi_{\rm astro}$ part of the WIMP-annihilation signal from all halos with $M_{\rm vir} > 2 \times 10^2 M_\odot/h$. For the peak-to-background ratio 15 simulations, the value of $\Phi_{\rm astro}$ is significantly boosted compared to all other halos with the same mass from the same simulation, due to the steeper profile density, as shown by Fig. 4.4 for the same two redshifts. However for the peak-to-background 5 simulation, we see that the special seed no longer has a larger value than average, but that its mass is considerably larger than in the peak-to-background 15 simulation, especially at $z = 30$, meaning that the special seed has has undergone more merging.

onment. The subsequent growth, profile steepness and WIMP-annihilation signal are all affected by the neighbouring perturbations.

We note that although almost all constraints from UCMHs have been made assuming a steep $r^{-9/4}$ profile to hold down to extremely small radii, the expectation from N-body simulations is that the emergence of NFW profiles is generic due to radial instabilities which will always exist and grow within realistic simulations (Angulo et al., 2016; Ogiya and Hahn, 2017; Dalal et al., 2010). However, we perform the first 3D simulations with boosted initial power spectra, probing small scales and starting deep in the radiation dominated era. We confirm that the NFW profile remains generic. In section 4.2.4 we have estimated an upper bound on the typical distance between an extremely large overdensity and the nearest overdensity with a comparable size, and shown that even a rare 5-σ fluctuation will not be isolated from the evolution of neighbouring halos over a long period of time.

Despite providing evidence that UCMHs of the form typically considered in the literature are not very likely to be realised in nature, we stress that our simulations with the initial power spectrum boosted on the kpc scale do form a significant number of dense NFW-like halos with masses around $10^4 - 10^5 M_\odot/h$. Furthermore, these halos have extremely large values of the concentration parameter $c = r_{\rm vir}/r_s$, which can grow to over 100 by redshift ten. Assuming the central density remains constant and the concentration grows roughly as $c \propto 1/(1+z)$ (Bullock et al., 2001) this would imply concentrations as large as 1000 by redshift zero. Subsequently, it would be very interesting to extend our simulations to redshift zero to study the stability of the halos we simulate with large con-

centration parameters. However, this would also require the inclusion of baryonic effects on these extremely small scales.

Given that the presence of halos with profiles close to $r^{-9/4}$ is unrealistic in the Universe the observational upper bounds on the primordial power spectrum on small scales, derived from the non-observation of UCMHs will have to be re-evaluated. However, given that we have also shown that when the primordial power spectrum is boosted even *typical* halos form at much higher densities and are thus much more compact than usual there are likely to be other means to constrain these small scales, which remains to be explored.

4.7 Acknowledgments

We gratefully acknowledge Camilla Penzo for providing her version of *RAMSES* that includes the contribution of radiation density in the Hubble function. The authors thank Jens Chluba, Peter Coles, Neal Dalal, Oliver Hahn, Massimo Ricotti, Patrick Scott, David Seery and Teruaki Suyama for interesting discussions. JA, CB and MG would like to thank the Department of Physics at the University of Auckland for kind hospitality. SH thanks Sussex University for hosting him on a return visit. CB is supported by a Royal Society University Research Fellowship. This work was supported by a grant from the Swiss National Supercomputing Centre (CSCS) under project ID s710.

4.A Appendix A: Notes about the simulations and halo analysis

4.A.1 Initial conditions and quasilinear evolution

In order to set up our initial conditions we use a customized version of the initial condition generator that is implemented in *gevolution* (Adamek et al., 2016a). In the public version of *gevolution*, the initial conditions are set up in terms of a linear displacement field and velocity potential that are obtained by multiplying a Gaussian realization of the primordial curvature perturbation by the respective linear transfer functions. The latter can be computed using a Boltzmann code such as *CAMB* (Lewis et al., 2000) or *CLASS* (Blas et al., 2011). As usual, the particle initial conditions are obtained by displacing particles from a regular lattice according to the gradient of the displacement field, and assigning velocities according to the gradient of the velocity potential. In our modification of this algorithm we introduce the possibility to create an initial configuration corresponding to a

spherical Gaussian overdensity that can act as a seed for a UCMH. Using the superposition principle that applies in the linear regime we allow in general for any linear combination of the random realization and this spherical overdensity.

The initial conditions are set deep inside the radiation dominated era, at redshift $z = 10\,000$ for the simulations with the special central halo or $z = 5\,000\,000$ for the simulations with the boosted power spectrum. We ignore the fact that the baryonic component of matter is strongly coupled at that time, assuming that at the small scales relevant for our study the perturbations in the baryon-photon plasma are irrelevant and we only have to consider CDM. Using *gevolution* we follow the initial logarithmic growth of the matter perturbations up to the point where the density contrast approaches unity for the most extreme initial conditions. This happens around $z \simeq 3000$.

4.A.2 Nonlinear evolution

The particle-mesh scheme of *gevolution*, which works at fixed spatial resolution, eventually becomes inadequate for tracking the detailed evolution of the very compact structures we are interested in. One common approach to deal with this issue is to use adaptive mesh refinement (AMR), that is to successively fine-grain the mesh in regions of high particle density. A cell-based AMR algorithm is implemented in the public code *RAMSES* (Teyssier, 2002). We use a slightly modified version where the Hubble function takes into account radiation density and hence is more accurate at high redshift. In order to pass from one code to the other we have *gevolution* write a snapshot that we then use as initial data for *RAMSES*. By running the two codes just a bit further and comparing snapshots at a later time (still before AMR is triggered in *RAMSES*) we convince ourselves that the change between codes did not introduce any unexpected issues.

For simplicity, we do not use the hydrodynamics modules of *RAMSES* which means that baryons are effectively treated as dark matter. Baryonic effects are expected to play an important role at low redshift $z \lesssim 10$, but we are not interested in these aspects here and stop our simulations before they become a serious concern.

4.A.3 Spherical shells and smoothing

Once halos have formed we identify them using the friends-of-friends halo finder algorithm *ROCKSTAR* (Behroozi et al., 2013). For each halo the profile of $1 + \delta$ is obtained by

counting the number of particles n inside the spherically symmetric shells around the center of the halo and dividing by the volume of each shell:

$$1 + \delta = \frac{\rho}{\bar{\rho}} = \frac{nV_{\rm shell}}{N^3 V}, \tag{4.27}$$

where N^3 is the number of all particles in the simulation and $V_{\rm shell}$ and V are the volumes of a chosen shell and the entire box, respectively. To reduce the noise at higher r, we have gradually increased the size of the bins such that every bin was larger than the previous by a constant factor: $r_{n+1} = qr_n$, which was set to $q = 1.01$. Therefore, in the i-th bin the density contrast was

$$1 + \delta = \frac{3nL^3}{4\pi N^3 r_0^3} \frac{(1-q)^3}{(1-q^{i+1})^3 - (1-q^i)^3}, \tag{4.28}$$

where L^3 represents the entire volume of the simulation. For the size of the starting bin r_0 we chose four-times the size of a cell for the finest AMR level. In our simulations the maximum refinement level was 16, and therefore the starting bin was $r_0 = 32/2^{14}\,{\rm kpc}/h = 1.95\ {\rm pc}/h$. This approach works as long as the halos are approximately spherical. To avoid empty bins in the shells where there happen to be no particles, we apply Gaussian smoothing with a width small enough to retain the shape of a halo profile. We checked that this does not degrade our resolution.

4.A.4 Convergence tests

In order to understand up to what minimal radius we can trust our results we ran some convergence tests. In Fig. 4.20 we show two simulations performed with *RAMSES* with the same initial conditions, but different number of particles: 256^3 and 512^3. This corresponds to a mass resolution of $0.169 M_\odot/h$ and $0.021 M_\odot/h$, respectively. In both cases the maximum AMR level was 16. From the plot we conclude that we can trust the lower-resolution simulation down to approximately $r \sim 2 \times 10^{-3}{\rm kpc}/h$. Unless indicated otherwise, our numerical results presented in Sections III–V were obtained with simulations that had 256^3 particles.

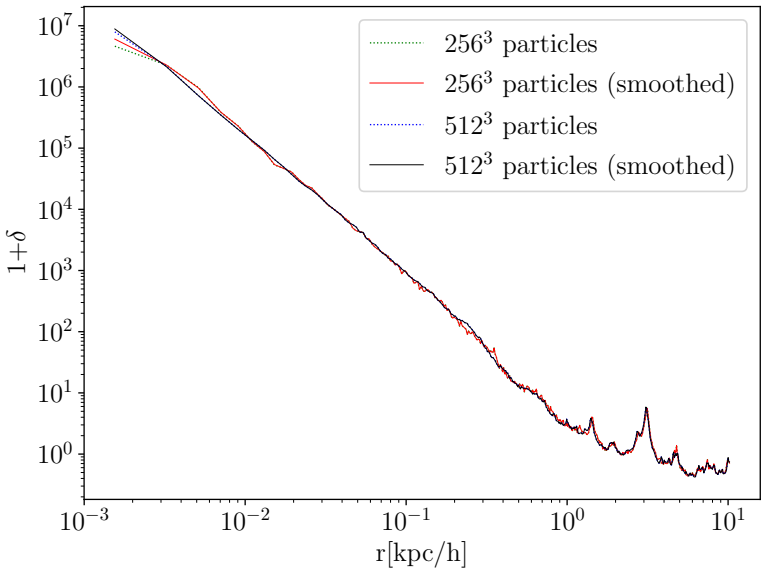

Figure 4.20: The profile of the Gaussian-seed halo in the peak-to-background ratio 15 simulation at $z = 30$ for two different numbers of particles. We also show the effect of smoothing – the profiles before applying smoothing are shown in dashed and the ones after are continuous. The smoothing we applied affects the shape of the profile even less than changing the resolution. The only noticeable difference is in the first bin.

Conclusion

In Chapter 2 we studied a quintessence model with an exponential potential and canonical kinetic term. We assumed a FLRW metric and explored how spatial curvature affects the evolution of the dynamical system. This was done by generalising the two-parameter flat case to three parameters. In contrast to the flat model, we demonstrated the existence of two new fixed points and elucidated the behaviour of the system in their vicinity. The first fixed point corresponds to a universe where the energy density is dominated by the curvature and is not attractive. The other one corresponds to a universe where energy density is a combination of curvature and the scalar field. This fixed point is interesting, because it attracts all trajectories with a negative curvature for a large class of exponential potentials. The system is therefore naturally drawn towards a configuration that corresponds to a fixed value of w.

Although it is well established that the universe today has almost critical density with little or no curvature, this fixed point might still be of interest for the cases where the energy density is dominated by the scalar field. The problem with using this solution to explain the accelerated expansion is that the equation-of-state parameter at this point is $-1/3$, but the present value has been measured to be very close to -1 (Abbott et al., 2017). In any case, there exists an attractor solution for flat, negatively curved and some positively curved cases where the equation-of-state parameter is close to the value $w = -1$ in the limit $\lambda \to 0$, which might be applicable to dark energy.

In Chapter 2 we focused on one specific and rather simple model, but this sort of curvature-inclusive analysis is applicable to other more complicated models that might exhibit significantly richer dynamical behaviour. Theories worth studying would be scalar fields with a more general potential (Copeland et al., 2009), non-canonical kinetic terms, multiple scalar fields, globally anisotropic metrics (i.e. the Bianchi models) (Fadragas et al., 2014), e.g. the Kantowski-Sachs model (Coley and Goliath, 2000), and models based on exact inhomogeneous cosmologies. These models would typically introduce several

extra parameters which would make their dynamics a lot more complex.

In Chapter 3 we developed a spherically symmetric general-relativistic N-body framework and simulated some particles' motions for a few initial conditions. The weak-field regime of general relativity was assumed. This framework was developed in a cosmological context, expanding around an FLRW metric. We reduced the complexity of the problem by introducing spherical symmetry. This not only shortened the set of equations but also meant that simulations became very fast. To test our code, we studied two cases with known exact solutions – the Schwarzschild and Lemaître-Tolman-Bondi metrics – and found good agreement between analytical solutions and our numerical results. In contrast with these special cases, our framework also applies in situations where no exact solution is known, for example when the fluid description of matter is not valid, such as when shell-crossings appear.

By comparing our numerical solution and the Schwarzschild solution around a point mass we demonstrated that the relativistic potentials we compute as accurate as the first-order post-Newtonian correction. This is of particular interest for the exploration of models with exotic sources of stress-energy perturbations, such as dynamical dark energy or modified gravity. The only assumption that goes into our scheme is the requirement that the gravitational fields remain weak. For example, this assumption breaks down when a black hole forms. In a purely spherical setup where particles only have radial velocities this will eventually be the case for any initial overdensity.

In order to avoid this and create stable bound structures, we introduced angular momentum, which in spherical case, effectively acts as pressure and opposes collapse. The objective was to create more realistic representations of cosmic structures such as galaxy clusters, which can then act as tests of gravity on these scales. This could also be applied to study the compact bound objects that can form in the early universe, such as ultracompact minihalos (which are the main theme in chapter 4), or for the early stages of the formation of primordial black holes.

In Chapter 4 we simulated the formation of ultracompact minihalos (UCMHs). First, we confirmed Bertschinger's (Bertschinger, 1985) analytical prediction that halos which form in isolation have a steep power-law profile.

As we increase the amplitude of perturbations surrounding the Gaussian-seed halo, its profile becomes closer to an NFW profile. We simulated two cases, in the first one the scale-invariant fluctuations had an amplitude boosted to be 15 times smaller than the one of the special halo, and in the second, this ratio was 5. In the first case, the special halo

can still be distinguished from the others: its profile resembles that of the power-law, but already starts to display some flattening in the centre, which is typical for NFW. In the second case, the special halo merges with some other, NFW-like halos in its surroundings and by $z = 30$ its profile is indistinguishable from the rest.

We also computed the dark-matter annihilation signal that such a halo would produce and compared it to the ones from the surrounding halos. This quantity is important because the tightest constraints on the abundance of UCMHs come from the non-detection of dark-matter annihilation signal. It is sensitive to the square of the density and therefore most of the signal comes from the centre of the halo. It is therefore important to establish whether in the centre density scales as $\rho \propto r^{-9/4}$ or $\rho \propto r^{-1}$ which is the case for NFW.

In the last part, we considered a slightly different setting, where we instead boosted the power spectrum at a selected scale. In this case halos form earlier, they have higher central densities, and are more compact compared to the situation without a boost. They however almost all exhibit a good fit to the NFW profile. Despite providing evidence that UCMHs of the form typically considered in the literature are not very likely to be realised in nature, we would like to stress that the dark-matter annihilation signal in a universe with a power-spectrum higher than expected would be enhanced.

It would be interesting to extend our simulations to redshift zero and study the stability the highly concentrated halos we found. This would most likely have to be performed with a "zoom-in" simulation. Another interesting question is how to include the effects of baryons.

This work also has observational consequences. Given that the presence of halos with profiles close to $r^{-9/4}$ is unrealistic, the observational upper bounds on the primordial power spectrum on small scales derived from the non-observation of UCMHs will have to be re-evaluated.

Bibliography

Aarseth, S. J. (1963). Dynamical evolution of clusters of galaxies, I. *Mon. Not. Roy. Astron. Soc.*, 126:223. 14

Abazajian, K., Fuller, G. M., and Patel, M. (2001). Sterile neutrino hot, warm, and cold dark matter. *Phys. Rev.*, D64:023501. 45

Abazajian, K. N. et al. (2009). The Seventh Data Release of the Sloan Digital Sky Survey. *Astrophys.J.Suppl.*, 182:543–558. 26

Abbott, B. P. e. a. (2017a). Gw170814: A three-detector observation of gravitational waves from a binary black hole coalescence. *Phys. Rev. Lett.*, 119:141101. 3

Abbott, B. P. e. a. (2017b). Gw170817: Observation of gravitational waves from a binary neutron star inspiral. *Phys. Rev. Lett.*, 119:161101. 3

Abbott, T. et al. (2005). The dark energy survey. 45

Abbott, T. M. C. et al. (2017). Dark Energy Survey Year 1 Results: Cosmological Constraints from Galaxy Clustering and Weak Lensing. 102

Abell, P. A. et al. (2009). LSST Science Book, Version 2.0. 25, 45

Adamek, J., Clarkson, C., Daverio, D., Durrer, R., and Kunz, M. (2017a). Safely smoothing spacetime: backreaction in relativistic cosmological simulations. 5

Adamek, J., Daverio, D., Durrer, R., and Kunz, M. (2013). General Relativistic N-body simulations in the weak field limit. *Phys.Rev.*, D88(10):103527. 45, 47

Adamek, J., Daverio, D., Durrer, R., and Kunz, M. (2016a). General relativity and cosmic structure formation. *Nature Phys.*, 12:346–349. 98

Adamek, J., Daverio, D., Durrer, R., and Kunz, M. (2016b). gevolution: a cosmological N-body code based on General Relativity. *JCAP*, 1607(07):053. 16

Adamek, J., Di Dio, E., Durrer, R., and Kunz, M. (2014a). Distance-redshift relation in plane symmetric universes. *Phys.Rev.*, D89(6):063543. 66

Adamek, J., Durrer, R., and Kunz, M. (2014b). N-body methods for relativistic cosmology. *Class.Quant.Grav.*, 31(23):234006. 45, 48

Adamek, J., Durrer, R., and Kunz, M. (2017b). Relativistic N-body simulations with massive neutrinos. 17

Ade, P. et al. (2014a). Planck 2013 results. XVI. Cosmological parameters. *Astron.Astrophys.*, 571:A16. 26

Ade, P. A. R. et al. (2014b). Planck 2013 results. XVI. Cosmological parameters. *Astron. Astrophys.*, 571:A16. 3

Ade, P. A. R. et al. (2015). Planck 2015 results. XIII. Cosmological parameters. 3, 17, 20, 44, 70

Alimi, J.-M., Bouillot, V., Rasera, Y., Reverdy, V., Corasaniti, P.-S., Balmes, I., Requena, S., Delaruelle, X., and Richet, J.-N. (2012). DEUS Full Observable ΛCDM Universe Simulation: the numerical challenge. 14

Alishahiha, M., Silverstein, E., and Tong, D. (2004). DBI in the sky. *Phys.Rev.*, D70:123505. 29

Alnes, H., Amarzguioui, M., and Gron, O. (2006). An inhomogeneous alternative to dark energy? *Phys.Rev.*, D73:083519. 29

Alpher, R. A., Bethe, H., and Gamow, G. (1948). The origin of chemical elements. *Phys. Rev.*, 73:803–804. 2

Anderson, L. et al. (2014). The clustering of galaxies in the SDSS-III Baryon Oscillation Spectroscopic Survey: baryon acoustic oscillations in the Data Releases 10 and 11 Galaxy samples. *Mon. Not. Roy. Astron. Soc.*, 441(1):24–62. 44

Angulo, R. E., Hahn, O., Ludlow, A., and Bonoli, S. (2016). Earth-mass haloes and the emergence of NFW density profiles. 73, 97

Angulo, R. E., Springel, V., White, S. D. M., Jenkins, A., Baugh, C. M., and Frenk, C. S. (2012). Scaling relations for galaxy clusters in the Millennium-XXL simulation. *Mon. Not. Roy. Astron. Soc.*, 426:2046. 14

Anthonisen, M., Brandenberger, R., and Scott, P. (2015). Constraints on cosmic strings from ultracompact minihalos. *Phys. Rev.*, D92(2):023521. 72

Arkani-Hamed, N., Cheng, H.-C., Luty, M. A., and Mukohyama, S. (2004). Ghost condensation and a consistent infrared modification of gravity. *JHEP*, 0405:074. 29

Armendariz-Picon, C., Damour, T., and Mukhanov, V. F. (1999). k - inflation. *Phys.Lett.*, B458:209–218. 28

Armendariz-Picon, C., Mukhanov, V. F., and Steinhardt, P. J. (2001). Essentials of k essence. *Phys.Rev.*, D63:103510. 28

Aslanyan, G., Price, L. C., Adams, J., Bringmann, T., Clark, H. A., Easther, R., Lewis, G. F., and Scott, P. (2016). Ultracompact minihalos as probes of inflationary cosmology. *Phys. Rev. Lett.*, 117(14):141102. 72

Bardeen, J. M., Bond, J. R., Kaiser, N., and Szalay, A. S. (1986). The Statistics of Peaks of Gaussian Random Fields. *Astrophys. J.*, 304:15–61. 78

Barnes, J. and Hut, P. (1986). A Hierarchical 0 Nlogn Force Calculation Algorithm. *Nature*, 324:446–449. 15

Baumgarte, T. W. and Shapiro, S. L. (1999). On the numerical integration of Einstein's field equations. *Phys. Rev.*, D59:024007. 46

Beck, G. and Colafrancesco, S. (2016). Hunting Dark Matter in ultra-compact structures: from large scales to the solar system. 72

Behroozi, P. S., Wechsler, R. H., and Wu, H.-Y. (2013). The Rockstar Phase-Space Temporal Halo Finder and the Velocity Offsets of Cluster Cores. *Astrophys. J.*, 762:109. 16, 75, 99

Ben-Dayan, I. and Kalaydzhyan, T. (2014). Constraining the primordial power spectrum from SNIa lensing dispersion. *Phys. Rev.*, D90(8):083509. 72

Bento, M. d. C., Bertolami, O., and Sen, A. (2003). Generalized Chaplygin gas and CMBR constraints. *Phys.Rev.*, D67:063003. 29

Berezinsky, V., Dokuchaev, V., and Eroshenko, Y. (2003). Small - scale clumps in the galactic halo and dark matter annihilation. *Phys. Rev.*, D68:103003. 46

Berezinsky, V. S., Dokuchaev, V. I., and Eroshenko, Y. N. (2014). Small-scale clumps of dark matter. *Phys. Usp.*, 57:1–36. [Usp. Fiz. Nauk184,3(2014)]. 72

Berezinsky, V. S., Dokuchaev, V. I., and Eroshenko, Yu. N. (2013). Formation and internal structure of superdense dark matter clumps and ultracompact minihaloes. *JCAP*, 1311:059. 72

Bernardeau, F., Colombi, S., Gaztanaga, E., and Scoccimarro, R. (2002). Large scale structure of the universe and cosmological perturbation theory. *Phys. Rept.*, 367:1–248. 11

Bertschinger, E. (1985). Self-similar secondary infall and accretion in an Einstein-de Sitter universe. *ApJS*, 58:39–65. 22, 72, 74, 95, 103

Betoule, M. et al. (2014). Improved cosmological constraints from a joint analysis of the SDSS-II and SNLS supernova samples. *Astron. Astrophys.*, 568:A22. 44

Blake, C. et al. (2012). The WiggleZ Dark Energy Survey: Joint measurements of the expansion and growth history at z $<$ 1. *Mon. Not. Roy. Astron. Soc.*, 425:405–414. 44

Blake, C. A., Abdalla, F. B., Bridle, S. L., and Rawlings, S. (2004). Cosmology with the Square Kilometre Array. *New Astron. Rev.*, 48:1063–1077. 25

Blas, D., Lesgourgues, J., and Tram, T. (2011). The Cosmic Linear Anisotropy Solving System (CLASS) II: Approximation schemes. *JCAP*, 1107:034. 98

Boehmer, C. G., Tamanini, N., and Wright, M. (2015). Interacting quintessence from a variational approach Part I: algebraic couplings. 29

Bouchet, F. R. and Hernquist, L. (1988). COSMOLOGICAL SIMULATIONS USING THE HIERARCHICAL TREE METHOD. *Submitted to: Astrophys. J.* 15

Boylan-Kolchin, M., Springel, V., White, S. D. M., Jenkins, A., and Lemson, G. (2009). Resolving Cosmic Structure Formation with the Millennium-II Simulation. *Mon. Not. Roy. Astron. Soc.*, 398:1150. 14

Brans, C. and Dicke, R. H. (1961). Mach's principle and a relativistic theory of gravitation. *Phys.Rev.*, 124:925–935. 28

Bringmann, T., Scott, P., and Akrami, Y. (2012). Improved constraints on the primordial power spectrum at small scales from ultracompact minihalos. *Phys. Rev.*, D85:125027. viii, 22, 23, 71, 72, 96

Bringmann, T. and Weniger, C. (2012). Gamma Ray Signals from Dark Matter: Concepts, Status and Prospects. *Phys. Dark Univ.*, 1:194–217. 91, 92

Bryan, G. L. and Norman, M. L. (1998). Statistical properties of x-ray clusters: Analytic and numerical comparisons. *Astrophys. J.*, 495:80. 75

Buchert, T. (1995). Lagrangian perturbation approach to the formation of large scale structure. In *Dark matter in the universe. Proceedings, 132nd course of the International School of Physics *Enrico Fermi*, Varenna, Italy, July 25-August 4, 1995*, pages 543–564. 13

Buchert, T. (2008). Dark Energy from Structure: A Status Report. *Gen.Rel.Grav.*, 40:467–527. 29

Buchert, T., Lavena, J., and Alimi, J.-M. (2006). Correspondence between Kinematical Backreaction and Scalar Field Cosmologies - the Morphon Field. *Class. Quant. Grav.*, 23:6379. 29

Bull, P., Clifton, T., and Ferreira, P. G. (2012). The kSZ effect as a test of general radial inhomogeneity in LTB cosmology. *Phys. Rev.*, D85:024002. 29

Bullock, J. S., Kolatt, T. S., Sigad, Y., Somerville, R. S., Kravtsov, A. V., Klypin, A. A., Primack, J. R., and Dekel, A. (2001). Profiles of dark haloes. Evolution, scatter, and environment. *Mon. Not. Roy. Astron. Soc.*, 321:559–575. 22, 76, 97

Bunn, E. F. and White, M. J. (1997). The Four year COBE normalization and large scale structure. *Astrophys. J.*, 480:6–21. 46

Burd, A. B. and Barrow, J. D. (1988). Inflationary Models with Exponential Potentials. *Nuc. Phys.*, B308:929. 30, 40

Busca, N. G. et al. (2013). Baryon Acoustic Oscillations in the Ly-α forest of BOSS quasars. *Astron. Astrophys.*, 552:A96. 44

Caldwell, R., Dave, R., and Steinhardt, P. J. (1998). Cosmological imprint of an energy component with general equation of state. *Phys.Rev.Lett.*, 80:1582–1585. 28

Caldwell, R. and Linder, E. V. (2005). The Limits of quintessence. *Phys.Rev.Lett.*, 95:141301. 28

Capozziello, S. (2002). Curvature quintessence. *Int.J.Mod.Phys.*, D11:483–492. 27

Carilli, C. L. and Rawlings, S. (2004). Science with the Square Kilometer Array: Motivation, key science projects, standards and assumptions. *New Astron. Rev.*, 48:979. 45

Carr, B., Tenkanen, T., and Vaskonen, V. (2017). Primordial black holes from inflaton and spectator field perturbations in a matter-dominated era. *Phys. Rev.*, D96(6):063507. 71

Carr, B. J. and Hawking, S. W. (1974). Black holes in the early Universe. *Mon. Not. Roy. Astron. Soc.*, 168:399–415. 46

Carr, B. J., Kohri, K., Sendouda, Y., and Yokoyama, J. (2010). New cosmological constraints on primordial black holes. *Phys. Rev.*, D81:104019. 71

Carroll, S. M. (2004). *Spacetime and geometry: An introduction to general relativity*. 6

Chiba, T., Okabe, T., and Yamaguchi, M. (2000). Kinetically driven quintessence. *Phys.Rev.*, D62:023511. 28

Chluba, J., Erickcek, A. L., and Ben-Dayan, I. (2012). Probing the inflaton: Small-scale power spectrum constraints from measurements of the CMB energy spectrum. *Astrophys. J.*, 758:76. 72

Choi, K.-Y. and Takahashi, T. (2017). New bound on low reheating temperature for dark matter in models with early matter domination. *Phys. Rev.*, D96(4):041301. 72

Clark, H. A., Iwanus, N., Elahi, P. J., Lewis, G. F., and Scott, P. (2017). Heating of galactic gas by dark matter annihilation in ultracompact minihalos. *JCAP*, 1705(05):048. 72

Clark, H. A., Lewis, G. F., and Scott, P. (2016a). Investigating dark matter substructure with pulsar timing ? I. Constraints on ultracompact minihaloes. *Mon. Not. Roy. Astron. Soc.*, 456(2):1394–1401. [Erratum: Mon. Not. Roy. Astron. Soc.464,no.2,2468(2017)]. 72

Clark, H. A., Lewis, G. F., and Scott, P. (2016b). Investigating dark matter substructure with pulsar timing ? II. Improved limits on small-scale cosmology. *Mon. Not. Roy. Astron. Soc.*, 456(2):1402–1409. [Erratum: Mon. Not. Roy. Astron. Soc.464,no.1,955(2017)]. 72

Cole, P. S. and Byrnes, C. T. (2017). Extreme scenarios: the tightest possible constraints on the power spectrum due to primordial black holes. 71

Cole, S. and Lacey, C. G. (1996). The Structure of dark matter halos in hierarchical clustering models. *Mon. Not. Roy. Astron. Soc.*, 281:716. 22

Coley, A. and Goliath, M. (2000). Closed cosmologies with a perfect fluid and a scalar field. *Phys.Rev.*, D62:043526. 41, 102

Copeland, E. J., Liddle, A. R., and Wands, D. (1998). Exponential potentials and cosmological scaling solutions. *Phys.Rev.*, D57:4686–4690. 28, 30

Copeland, E. J., Mizuno, S., and Shaeri, M. (2009). Dynamics of a scalar field in Robertson-Walker spacetimes. *Phys.Rev.*, D79:103515. 41, 102

Copeland, E. J., Sami, M., and Tsujikawa, S. (2006). Dynamics of dark energy. *Int. J. Mod. Phys.*, D15:1753–1936. 28, 45

Dalal, N., Lithwick, Y., and Kuhlen, M. (2010). The Origin of Dark Matter Halo Profiles. *ArXiv e-prints*. 73, 97

Davis, M., Summers, F. J., and Schlegel, D. (1992). Large scale structure in a universe with mixed hot and cold dark matter. *Nature*, 359:393–396. 45

Dvali, G., Gabadadze, G., and Porrati, M. (2000). 4-D gravity on a brane in 5-D Minkowski space. *Phys.Lett.*, B485:208–214. 28

Eddington, A. S. (1924). *The Mathematical Theory of Relativity*, page 93. Cambridge University Press, 2nd edition. 51

Einstein, A. (1939). On a stationary system with spherical symmetry consisting of many gravitating masses. *Annals Math.*, 40:922–936. 58

Emami, R. and Smoot, G. (2017). Observational Constraints on the Primordial Curvature Power Spectrum. 72

Fadragas, C. R., Leon, G., and Saridakis, E. N. (2014). Dynamical Analysis of anisotropic scalar-field cosmologies for a wide range of potentials. *Class. Quant. Grav.*, 31:075018. 41, 102

Fosalba, P., Crocce, M., Gaztañaga, E., and Castander, F. J. (2015). The MICE grand challenge lightcone simulation - I. Dark matter clustering. *Mon. Not. Roy. Astron. Soc.*, 448:2987–3000. 14

Garousi, M. R. (2000). Tachyon couplings on nonBPS D-branes and Dirac-Born-Infeld action. *Nucl.Phys.*, B584:284–299. 29

Gasperini, M. and Veneziano, G. (1993). Pre - big bang in string cosmology. *Astropart.Phys.*, 1:317–339. 28

Gleiser, Reinaldo J. and Ramirez, Marcos A. (2009). On the dynamics of thin shells of counter rotating particles. *Class. Quant. Grav.*, 26:045006. 62, 63

Gleiser, Reinaldo J. and Ramirez, Marcos A. (2010). Static spherically symmetric Einstein-Vlasov shells made up of particles with a discrete set of values of their angular momentum. *Class. Quant. Grav.*, 27:065008. 62, 63

Green, S. R. and Wald, R. M. (2011). A new framework for analyzing the effects of small scale inhomogeneities in cosmology. *Phys.Rev.*, D83:084020. 45

Green, S. R. and Wald, R. M. (2012). Newtonian and Relativistic Cosmologies. *Phys.Rev.*, D85:063512. 45

Griffen, B. F., Ji, A. P., Dooley, G. A., Gómez, F. A., Vogelsberger, M., O'Shea, B. W., and Frebel, A. (2016). The Caterpillar Project: a Large Suite of Milky way Sized Halos. *Astrophys. J.*, 818(1):10. 14

Guo, Z.-K., Ohta, N., and Tsujikawa, S. (2007). Probing the Coupling between Dark Components of the Universe. *Phys.Rev.*, D76:023508. 29

Guth, A. H. (1981). The Inflationary Universe: A Possible Solution to the Horizon and Flatness Problems. *Phys. Rev.*, D23:347–356. 17

Haggerty, M. J. and Janin, G. (1974). Numerical experiments on cosmological clustering. *AAP*, 36:415–427. 14

Halliwell, J. J. (1987). Scalar Fields in Cosmology with an Exponential Potential. *Phys. Lett.*, B185:341. 30

Hawking, S. (1971). Gravitationally collapsed objects of very low mass. *Mon. Not. Roy. Astron. Soc.*, 152:75. 46

Heitmann, K., Frontiere, N., Sewell, C., Habib, S., Pope, A., Finkel, H., Rizzi, S., Insley, J., and Bhattacharya, S. (2015). The Q Continuum Simulation: Harnessing the Power of GPU Accelerated Supercomputers. *Astrophys. J. Suppl.*, 219(2):34. 14

Hinshaw, G. et al. (2013). Nine-Year Wilkinson Microwave Anisotropy Probe (WMAP) Observations: Cosmological Parameter Results. *Astrophys.J.Suppl.*, 208:19. 26

Hirata, K. et al. (1987). Observation of a Neutrino Burst from the Supernova SN 1987a. *Phys. Rev. Lett.*, 58:1490–1493. [,727(1987)]. 3

Hockney, R. W. and Eastwood, J. W. (1999). *Computer Simulation Using Particles*. Institute of Physics Publ. 67

Holmberg, E. (1941). On the Clustering Tendencies among the Nebulae. II. a Study of Encounters Between Laboratory Models of Stellar Systems by a New Integration Procedure. *Astrophys. J.,*, 94:385. 14

Hu, W. and Sawicki, I. (2007). A Parameterized Post-Friedmann Framework for Modified Gravity. *Phys.Rev.*, D76:104043. 27

Hubble, E. (1929). A relation between distance and radial velocity among extra-galactic nebulae. *Proc. Nat. Acad. Sci.*, 15:168–173. 2

Josan, A. S. and Green, A. M. (2010a). Constraints from primordial black hole formation at the end of inflation. *Phys. Rev.*, D82:047303. 71

Josan, A. S. and Green, A. M. (2010b). Gamma-rays from ultracompact minihalos: potential constraints on the primordial curvature perturbation. *Phys. Rev.*, D82:083527. 72, 90

Kamenshchik, A. Y., Moschella, U., and Pasquier, V. (2001). An Alternative to quintessence. *Phys.Lett.*, B511:265–268. 29

Kawasaki, M., Kusenko, A., Tada, Y., and Yanagida, T. T. (2016). Primordial black holes as dark matter in supergravity inflation models. *Phys. Rev.*, D94(8):083523. 71

Khoury, J., Ovrut, B. A., Steinhardt, P. J., and Turok, N. (2001). The Ekpyrotic universe: Colliding branes and the origin of the hot big bang. *Phys. Rev.*, D64:123522. 17

Khoury, J. and Weltman, A. (2004). Chameleon cosmology. *Phys.Rev.*, D69:044026. 29

Kilbinger, M. et al. (2013). CFHTLenS: Combined probe cosmological model comparison using 2D weak gravitational lensing. *Mon. Not. Roy. Astron. Soc.*, 430:2200–2220. 44

Kim, J., Park, C., Rossi, G., Lee, S. M., and Gott, III, J. R. (2011). The New Horizon Run Cosmological N-Body Simulations. *J. Korean Astron. Soc.*, 44:217–234. 14

Klypin, A., Trujillo-Gomez, S., and Primack, J. (2011). Halos and galaxies in the standard cosmological model: results from the Bolshoi simulation. *Astrophys. J.*, 740:102. 14

Knebe, A. et al. (2011). Haloes gone MAD: The Halo-Finder Comparison Project. *Mon. Not. Roy. Astron. Soc.*, 415:2293–2318. 16

Kohri, K., Nakama, T., and Suyama, T. (2014). Testing scenarios of primordial black holes being the seeds of supermassive black holes by ultracompact minihalos and CMB μ-distortions. *Phys. Rev.*, D90(8):083514. 71, 94

Kolb, E. W., Matarrese, S., Notari, A., and Riotto, A. (2005). The Effect of inhomogeneities on the expansion rate of the universe. *Phys.Rev.*, D71:023524. 29

Kravtsov, A. V., Klypin, A. A., and Khokhlov, A. M. (1997). Adaptive refinement tree: A New high resolution N body code for cosmological simulations. *Astrophys. J. Suppl.*, 111:73. 15

Kwan, J., Heitmann, K., Habib, S., Padmanabhan, N., Finkel, H., Lawrence, E., Frontiere, N., and Pope, A. (2015). Cosmic Emulation: Fast Predictions for the Galaxy Power Spectrum. *Astrophys. J.*, 810(1):35. 17

Lacki, B. C. and Beacom, J. F. (2010). Primordial Black Holes as Dark Matter: Almost All or Almost Nothing. *Astrophys. J.*, 720:L67–L71. 71

Laureijs, R. et al. (2011). Euclid Definition Study Report. 16, 24, 45

Levi, M. et al. (2013). The DESI Experiment, a whitepaper for Snowmass 2013. 25

Lewis, A., Challinor, A., and Lasenby, A. (2000). Efficient computation of CMB anisotropies in closed FRW models. *Astrophys. J.*, 538:473–476. 87, 98

Li, F., Erickcek, A. L., and Law, N. M. (2012). A new probe of the small-scale primordial power spectrum: astrometric microlensing by ultracompact minihalos. *Phys. Rev.*, D86:043519. 72

Liddle, A. R. and Lyth, D. H. (1992). COBE, gravitational waves, inflation and extended inflation. *Phys. Lett.*, B291:391–398. 19

Liddle, A. R. and Urena-Lopez, L. A. (2006). Inflation, dark matter and dark energy in the string landscape. *Phys.Rev.Lett.*, 97:161301. 29

Linde, A. D. (1982). A New Inflationary Universe Scenario: A Possible Solution of the Horizon, Flatness, Homogeneity, Isotropy and Primordial Monopole Problems. *Phys. Lett.*, 108B:389–393. 17

Lithwick, Y. and Dalal, N. (2011). Self-similar Solutions of Triaxial Dark Matter Halos. *Astrophys. J.,*, 734:100. 73, 74, 79

Lumsden, S. L., Heavens, A. F., and Peacock, J. A. (1989). The clustering of peaks in a random Gaussian field. *MNRAS*, 238:293–318. 78

Lyth, D. H. (2012). The hybrid inflation waterfall and the primordial curvature perturbation. *JCAP*, 1205:022. 78

Lyth, D. H. and Liddle, A. R. (2009). *The primordial density perturbation: Cosmology, inflation and the origin of structure*. 6

Lyth, D. H. and Wands, D. (2002). Generating the curvature perturbation without an inflaton. *Phys. Lett.*, B524:5–14. 17

Mack, K. J., Ostriker, J. P., and Ricotti, M. (2007). Growth of structure seeded by primordial black holes. *Astrophys. J.*, 665:1277–1287. 71

Malik, K. A. and Matravers, D. R. (2013). Comments on gauge-invariance in cosmology. *Gen. Rel. Grav.*, 45:1989–2001. 53

Natarajan, A., Zhu, N., and Yoshida, N. (2015). Probing the Small Scale Matter Power Spectrum through Dark Matter Annihilation in the Early Universe. 72

Navarro, J. F., Frenk, C. S., and White, S. D. M. (1996). The Structure of cold dark matter halos. *Astrophys. J.*, 462:563–575. 22, 75

Navarro, J. F., Frenk, C. S., and White, S. D. M. (1997). A Universal density profile from hierarchical clustering. *Astrophys. J.*, 490:493–508. 22, 75

Nunez, A. and Solganik, S. (2005). Ghost constraints on modified gravity. *Phys.Lett.*, B608:189–193. 28

Ogiya, G. and Hahn, O. (2017). What sets the central structure of dark matter haloes? 73, 97

Okouma, P. M., Fantaye, Y., and Bassett, B. A. (2013). How Flat is Our Universe Really? *Phys. Lett.*, B719:1–4. 29

Pattison, C., Vennin, V., Assadullahi, H., and Wands, D. (2017). Quantum diffusion during inflation and primordial black holes. 71

Pavlov, A., Westmoreland, S., Saaidi, K., and Ratra, B. (2013). Nonflat Time-variable Dark Energy Cosmology. *Phys. Rev.*, D88:123513. 30

Peebles, P. and Vilenkin, A. (1999). Quintessential inflation. *Phys.Rev.*, D59:063505. 29

Penzias, A. A. and Wilson, R. W. (1965). A Measurement of excess antenna temperature at 4080-Mc/s. *Astrophys. J.*, 142:419–421. 3

Percival, W. J. et al. (2010). Baryon Acoustic Oscillations in the Sloan Digital Sky Survey Data Release 7 Galaxy Sample. *Mon.Not.Roy.Astron.Soc.*, 401:2148–2168. 26

Perlmutter, S. et al. (1999). Measurements of Omega and Lambda from 42 high redshift supernovae. *Astrophys.J.*, 517:565–586. 3, 26

Peskin, M. E. and Schroeder, D. V. (1995). *An Introduction to quantum field theory*. Addison-Wesley, Reading, USA. 5

Plebanski, J. and Krasinski, A. (2006). *An introduction to general relativity and cosmology*. Cambridge University Press. 53

Potter, D., Stadel, J., and Teyssier, R. (2016). PKDGRAV3: Beyond Trillion Particle Cosmological Simulations for the Next Era of Galaxy Surveys. 14

Prada, F., Klypin, A. A., Cuesta, A. J., Betancort-Rijo, J. E., and Primack, J. (2012). Halo concentrations in the standard LCDM cosmology. *Mon. Not. Roy. Astron. Soc.*, 423:3018–3030. 14

Press, W. H. and Schechter, P. (1974). Formation of galaxies and clusters of galaxies by selfsimilar gravitational condensation. *Astrophys. J.*, 187:425–438. 14

Rasanen, S. (2004). Dark energy from backreaction. *JCAP*, 0402:003. 29

Ratra, B. and Peebles, P. J. E. (1988). Cosmological consequences of a rolling homogeneous scalar field. *Phys. Rev. D*, 37(12):3406–3427. 28

Rekier, J., Cordero-Carrión, I., and Füzfa, A. (2015). Fully relativistic non-linear cosmological evolution in spherical symmetry using the BSSN formalism. *Phys. Rev.*, D91(2):024025. 46

Ricotti, M. and Gould, A. (2009). A New Probe of Dark Matter and High-Energy Universe Using Microlensing. *Astrophys. J.*, 707:979–987. 46, 72, 74, 96

Riess, A. G. et al. (1998). Observational evidence from supernovae for an accelerating universe and a cosmological constant. *Astron.J.*, 116:1009–1038. 3, 14, 26

Roy, X., Buchert, T., Cartoni, S., and Obadiah, N. (2011). Global gravitational instability of FLRW backgrounds - interpreting the dark sectors. *Class. Quant. Grav.*, 28:165004. 29

Rubin, V. C., Thonnard, N., and Ford, Jr., W. K. (1980). Rotational properties of 21 SC galaxies with a large range of luminosities and radii, from NGC 4605 /R = 4kpc/ to UGC 2885 /R = 122 kpc/. *Astrophys. J.*, 238:471. 4

Saito, R. and Shirai, S. (2011). Primordial Black Hole as a Source of the Boost Factor. *Phys. Lett.*, B697:95–100. 71

Samushia, L. et al. (2013). The Clustering of Galaxies in the SDSS-III DR9 Baryon Oscillation Spectroscopic Survey: Testing Deviations from Λ and General Relativity using anisotropic clustering of galaxies. *Mon. Not. Roy. Astron. Soc.*, 429:1514–1528. 44

Schneider, A. and Teyssier, R. (2015). A new method to quantify the effects of baryons on the matter power spectrum. *JCAP*, 1512(12):049. 17

Scoccimarro, R. (1998). Transients from initial conditions: a perturbative analysis. *MNRAS*, 299:1097–1118. 13

Shandera, S., Erickcek, A. L., Scott, P., and Galarza, J. Y. (2013). Number Counts and Non-Gaussianity. *Phys. Rev.*, D88(10):103506. 72

Shibata, M. and Nakamura, T. (1995). Evolution of three-dimensional gravitational waves: Harmonic slicing case. *Phys. Rev.*, D52:5428–5444. 46

Silverstein, E. and Tong, D. (2004). Scalar speed limits and cosmology: Acceleration from D-cceleration. *Phys.Rev.*, D70:103505. 29

Sivanandam, N. (2013). Is the Cosmological Coincidence a Problem? *Phys. Rev.*, D87(8):083514. 27

Skillman, S. W., Warren, M. S., Turk, M. J., Wechsler, R. H., Holz, D. E., and Sutter, P. M. (2014). Dark Sky Simulations: Early Data Release. 14

Slipher, V. M. (1917). Nebulae. *Proc. Am. Phil. Soc.*, 56:403–409. 2

Smoot, G. F. et al. (1992). Structure in the COBE differential microwave radiometer first year maps. *Astrophys. J.*, 396:L1–L5. 3

Spergel, D. N. et al. (2007). Wilkinson Microwave Anisotropy Probe (WMAP) three year results: implications for cosmology. *Astrophys. J. Suppl.*, 170:377. 3

Springel, V. (2005). The Cosmological simulation code GADGET-2. *Mon. Not. Roy. Astron. Soc.*, 364:1105–1134. 15

Springel, V. et al. (2005). Simulating the joint evolution of quasars, galaxies and their large-scale distribution. *Nature*, 435:629–636. 14

Starobinsky, A. A. (1980). A New Type of Isotropic Cosmological Models Without Singularity. *Phys. Lett.*, 91B:99–102. 17

Starobinsky, A. A. (2007). Disappearing cosmological constant in f(R) gravity. *JETP Lett.*, 86:157–163. 27

Steinhardt, P. J., Wang, L.-M., and Zlatev, I. (1999). Cosmological tracking solutions. *Phys.Rev.*, D59:123504. 28

Sussman, R. A., Hidalgo, J. C., Dunsby, P. K. S., and German, G. (2015). Spherical dust fluctuations: The exact versus the perturbative approach. *Phys. Rev.*, D91(6):063512. 53

Tamanini, N. (2014). Dynamics of cosmological scalar fields. *Phys.Rev.*, D89(8):083521. 28

Teyssier, R. (2002). Cosmological hydrodynamics with adaptive mesh refinement: a new high resolution code called ramses. *Astron. Astrophys.*, 385:337–364. 15, 99

Tomita, K. (2001). A local void and the accelerating universe. *Mon.Not.Roy.Astron.Soc.*, 326:287. 29

Tormen, G., Bouchet, F. R., and White, S. D. M. (1997). The Structure and dynamical evolution of dark matter halos. *Mon. Not. Roy. Astron. Soc.*, 286:865–884. 22

Tsujikawa, S. (2008). Observational signatures of f(R) dark energy models that satisfy cosmological and local gravity constraints. *Phys.Rev.*, D77:023507. 27

Tsujikawa, S. (2010a). Dark energy: investigation and modeling. 28

Tsujikawa, S. (2010b). Modified gravity models of dark energy. *Lect.Notes Phys.*, 800:99–145. 27

Tsujikawa, S. (2013). Quintessence: A Review. *Class.Quant.Grav.*, 30:214003. 28

Van Acoleyen, K. (2008). LTB solutions in Newtonian gauge: From Strong to weak fields. *JCAP*, 0810:028. 53

van den Aarssen, L. G., Bringmann, T., and Goedecke, Y. C. (2012). Thermal decoupling and the smallest subhalo mass in dark matter models with Sommerfeld-enhanced annihilation rates. *Phys. Rev.*, D85:123512. 72

van den Hoogen, R., Coley, A. A., and Wands, D. (1999). Scaling solutions in Robertson-Walker space-times. *Class.Quant.Grav.*, 16:1843–1851. 29

Vogelsberger, M., White, S. D. M., Mohayaee, R., and Springel, V. (2009). Caustics in growing Cold Dark Matter Haloes. *Mon. Not. Roy. Astron. Soc.*, 400:2174. 79

Weinberg, S. (1989). The cosmological constant problem. *Rev. Mod. Phys.*, 61:1–23. 23, 27

Wetterich, C. (1988). Cosmology and the fate of dilatation symmetry. *Nuclear Physics B*, 302(4):668–696. 28

Wetterich, C. (1995). The Cosmon model for an asymptotically vanishing time dependent cosmological 'constant'. *Astron.Astrophys.*, 301:321–328. 29

Yang, Y. (2014). Constraints on the primordial power spectrum of small scales using the neutrino signals from the dark matter decay. *Int. J. Mod. Phys.*, A29(32):1450194. 72

Yang, Y., Yang, G., Huang, X., Chen, X., Lu, T., and Zong, H. (2013a). Contribution of ultracompact dark matter minihalos to the isotropic radio background. *Phys. Rev.*, D87(8):083519. 72

Yang, Y., Yang, G., and Zong, H. (2013b). Dark Matter Decay and the Abundance of Ultracompact Minihalos. *EPL*, 101(6):69001. 72

Yang, Y., Yang, G., and Zong, H. (2013c). Neutrino signals from ultracompact minihalos and constraints on the primordial curvature perturbation. *Phys. Rev.*, D87(10):103525. 72

Yoo, J. and Watanabe, Y. (2012a). Theoretical Models of Dark Energy. *Int. J. Mod. Phys.*, D21:1230002. 23

Yoo, J. and Watanabe, Y. (2012b). Theoretical Models of Dark Energy. *Int.J.Mod.Phys.*, D21:1230002. 27, 28

Zackrisson, E. et al. (2013). Hunting for dark halo substructure using submilliarcsecond-scale observations of macrolensed radio jets. *Mon. Not. Roy. Astron. Soc.*, 431:2172–2183. 72

Zel'dovich, Y. B. (1970). Gravitational instability: An approximate theory for large density perturbations. *AAP*, 5:84–89. 13

Zhang, D. (2011). Impact of Primordial Ultracompact Minihaloes on the Intergalactic Medium and First Structure Formation. *Mon. Not. Roy. Astron. Soc.*, 418:1850. 72

Zlatev, I., Wang, L.-M., and Steinhardt, P. J. (1999). Quintessence, cosmic coincidence, and the cosmological constant. *Phys.Rev.Lett.*, 82:896–899. 28